FLETCHER M

TEMPERATURE DEPENDENCE OF DAMAGE RANGES

IN ION IMPLANTED METALS

MSc(Physics)   UP   1990

Temperature dependence of damage ranges in ion implanted metals

MARIANNE FLETCHER

submitted as partial fulfillment of the requirements
for the degree of

MAGISTER SCIENTIAE

(Physics)

in the faculty of Science

UNIVERSITY OF PRETORIA

MAY 1990

TEMPERATURE DEPENDENCE OF DAMAGE RANGES IN ION IMPLANTED METALS

Marianne Fletcher

Supervisor   :   Prof E K H Friedland

Co–supervisor: Prof H W Alberts

Department   :   Physics

Degree   :   MSc

SUMMARY

Damage ranges in ion–implanted crystalline metals have been found to lie significantly deeper than the ranges predicted by the stopping theory for ions in amorphous materials. This phenomenon is especially significant in fcc crystals and occurs to a lesser extent in bcc metals. Three mechanisms have been proposed to explain these unexpectedly deep damage ranges: the channeling of implanted ions, thermal migration of radiation–induced interstitials, as well as a stress field propagation of defects which initially lie within the range predicted by the LSS theory.

In order to obtain some insight into the relevance of these three possible mechanisms it is necessary to study as many possible variables which might influence both the range distribution as well as the level of radiation–induced damage. This study investigates the temperature dependence of the damage.

Single crystals of fcc copper, nickel and platinum, as well as the bcc metal alpha–iron, were implanted off–axially at various temperatures (ranging from 77K to 573K) with 150 keV argon ions using similar dose rates and fluences. Rutherford backscattering of 1–2 MeV alpha particles was used to obtain dechanneling spectra which provided information as to the extent and level of the radiation damage.

(ii)

In previous studies the deep damage ranges have generally been found to increase gradually with implantation temperature. While this investigation discerned a similar trend for iron, no definite temperature dependence of the radiation damage ranges in nickel and copper could be established due to large standard deviations in experimental data. The damage range in platinum was unexpectedly found to decrease with implantation temperature. Especially in the case of platinum, but also possibly in the other three metals, the level of radiation damage in all the samples was found to decrease with implantation temperature.

Due to the very large differences observed in the relative damage ranges of the various metals, thermal migration of interstitials is not expected to be the main cause of the unexpectedly deep damage ranges because the migration energies in these solids are quite similar. The large differences in relative damage range may however be incorporated within a stress field defect propagation model. Such a model would also explain the fact that the experimentally obtained damage range in iron does not significantly differ from the LSS range of Ar^+ ions in this metal: Because the slip planes in bcc metals are less densely packed than in fcc metals, the Peierls force opposing glide along these slip planes is greater in bcc metals. Within a thermal spike–induced stress field model a gradual increase in radiation damage range with temperature is considered reasonable due to the decrease in Peierls force with increase in ambient crystal temperature. An increase in damage range with temperature can also be expected due to decreased crowdion trajectories resulting in a greater amount of displacement collisions occurring within the collision cascade region. This would lead to an intensification of the thermal spike and subsequently greater thermal expansion, causing defects to be propagated deeper into the crystal the greater the implantation temperature. The decrease in damage levels with temperature that was observed in all the samples investigated can also be explained within the stress field defect propagation model.

Due to the fact that insufficient Ar^+ ions are expected to penetrate via channeling to depths corresponding to the observed radiation damage ranges (especially for off–axial implantation) channeling is not expected to play a major role in the production of deep damage. This was confirmed by the fact that iron, which has a relative damage range of about 1, was calculated to possess Ar^+ channeling half angles of comparable size and orientation to

those calculated for nickel and copper, which displayed significantly larger relative damage ranges. However, the low temperature channeling half angles for platinum were calculated to be considerably greater than those of any of the other metals. It is suggested that channeling of Ar^+ ions could well be the major cause of the deep damage found in low temperature implanted platinum. Reduced channeling half angles with increase in implantation temperature might then also provide an explanation for the observed decrease in platinum damage range.

TEMPERATUURAFHANKLIKHEID VAN SKADEREIKWYDTE IN IOONGEïNPLANTEERDE METALE

Marianne Fletcher

Leier   :   Prof E K H Friedland

Medeleier   :   Prof H W Alberts

Departement: Fisika

Graad   :   MSc

OPSOMMING

Dit is reeds bekend dat diepteprofiele van ioongeïnplanteerde skade in kristallyne metale veel dieper lê as wat die ioon–afremmingsteorie voorspel vir die reikafstand van ione in amorfe materiale. Hierdie verskynsel vind veral plaas in vsk kristalle en word tot 'n mindere mate ook in bsk metale waargeneem. Drie meganismes is reeds voorgestel ter verklaring van hierdie onverwagte diep skade: die kanalisering van geïnplanteerde ione, termiese migrasie van stralingsgeïnduseerde tussenruimtelike atome, asook die inforsering (deur middel van 'n drukspanningsveld) van ontwrigtings wat aanvanklik lê in die gebied voorspel deur die LSS teorie.

Die juistheid van hierdie drie voorgestelde meganismes kan ondersoek word deur so veel moontlike veranderlikes, wat beide die skadediepte sowel as die hoeveelheid skade beïnvloed, te bestudeer. In hierdie werkstuk word die temperatuurafhanklikheid van die stralingskade ondersoek.

Enkelkristalle van vsk koper, nikkel en platinum, sowel as die bsk metaal alfa–yster, is by verskillende temperature (77–573K) met 150 keV Ar^+–ione geïnplanteer (in 'n nie–aksiale rigting). Die dosis en tempo van inplantering is deurentyd konstant gehou. Rutherford terugverstrooiing van 1–2 MeV alfa-deeltjies is gebruik om dekanaliseringspektra van die beskadigde oppervlaktes te bekom. Vanuit hierdie spektra kon inligting verkry word

omtrent beide die diepte van die skade asook die hoeveelheid skade wat berokken is deur die energieke argon-ione.

Verskillende outeure het reeds waargeneem dat die diepte van die stralingskade geleidelik toeneem met toename in inplanteringstemperatuur. Alhoewel 'n soortgelyke tendens in hierdie studie vasgestel is vir yster, kon geen besliste temperatuurafhanklikheid van die skadediepte vasgestel word vir nikkel en koper nie, weens die feit dat baie groot standaardafwykings in eksperimentele resultate verkry is. Dit was wel onverwags om te vind dat die skadediepte in platinum afneem met inplanteringstemperatuur. Veral in die geval van platinum, maar vermoedelik ook vir die ander drie metale, is gevind dat die hoeveelheid skade afneem met toename in substraattemperatuur tydens inplantering.

Weens die baie groot verskille wat waargeneem is in die relatiewe skadereikafstand in die verskillende metale, word veronderstel dat termiese migrasie van tussenruimtelike atome nie die hoof oorsaak van diep skadeproduksie is nie. Hierdie groot verskille kan wel verklaar word deur middel van die drukspanningsveldmodel. Die feit dat die eksperimentele skadereikafstand in yster nie grootliks verskil van die afremmingsafstand van ione (soos deur die LSS teorie voorspel word) nie, kan ook deur bogenoemde model verklaar word: Omdat die glipvlakke in bsk metale minder diggepak is as in die geval van vsk metale, is die Peierlskrag (wat ontwrigtingsglip teenwerk) groter in bsk metale. Binne hierdie "termiese priem"-geïnduseerde drukspanningsveldmodel sou 'n geleidelike toename in skadediepte met inplanteringstemperatuur bowendien verwag word weens die afname in die Peierlskrag met temperatuur. Verder neem die lengte van gefokusseerde botsingsreekse af met temperatuur. Die gevolg hiervan is dat die digtheid van uitruilingsbotsings binne die botsingskaskadegebied toeneem, sodat die "termiese priem" geassosieer met kaskadeontwikkeling meer intens is. Gevolglik vind groter termiese uitsetting plaas en derhalwe word ontwrigtings dieper die kristal ingeforseer hoe hoër die inplanteringstemperatuur. Die waargenome afname in skadedigtheid met toename in temperatuur (vir al die metale wat ondersoek is) kan ook binne die drukspanningsveldmodel verklaar word.

Weens die feit dat te min argon-ione deur middel van kanalisering gewoonlik die waargenome diepskadegebied bereik (veral in die geval van in-

plantering weg van 'n hoof–asrigting) word daar nie verwag dat kanalisering die hoof oorsaak van diepskadeproduksie is nie. In hierdie ondersoek is hierdie verwagting vervul deur die waarneming dat yster (met 'n relatiewe skadereikafstand van ongeveer 1) teoreties–berekende kanaliseringshalfhoeke besit wat beide in grootte en oriëntering goed ooreenstem met die berekende halfhoeke van nikkel en koper (waarin veel groter relatiewe skadereikafstande bereik word). In teenstelling is bereken dat die lae–temperatuur kanaliseringshalfhoeke van platinum heelwat groter is as in die geval van enige van die ander metale. Daarom word voorgestel dat kanalisering van argon-ione wel die hoofoorsaak van diepskadeproduksie mag wees in die geval van lae–temperatuur–geïnplanteerde platinum. Die afname in die grootte van die halfhoeke met toename in substraattemperatuur mag dan ook as verklaring dien vir die waargenome afname in die diepte van die stralingskade in platinum met toename in temperatuur.

FOREWORD

In the last two decades ion implantation has increasingly been used to modify near–surface properties of metals. Changes in chemical composition as well as changes in the crystal structure of the surface region may be caused by energetic ion bombardment. In this study chemically inert argon was implanted into various fcc and bcc metal single crystals and therefore the main change in the surfaces of these metals is expected to be of a physical nature, i.e. the introduction of defect structures such as dislocation loops and vacancy or interstitial clusters. The foreign argon ions situated within the target material also cause disruption of the initially "perfect" crystal structure.

The altered surface properties of metals after ion implantation include modification of corrosion and wear resistance[1,2], changes in the mechanical hardness of the surfaces[3] as well as changes in their friction and lubrication properties[4]. Radiation damage has also been found to influence the fatigue lifetime of a metal[2,5]. Reasons for changes in the surface properties of metals after ion implantation may be attributed to occurrences such as thickening of surface–oxide films due to the presence of defects within the surface layer. (This has been found to occur for Ar implanted into iron[1].) Implantation of metal ions may cause the formation of surface alloys which are effective in modifying corrosion behaviour[6].

Ion implantation has also been employed for the simulation of radiation damage caused by fast neutrons. The bcc metal α–iron is of particular interest for such radiation damage studies since it is a major constituent in many structural alloys, including the ferritic steels widely used in the construction of nuclear reactors.

Damage ranges in crystalline metals have been found to significantly exceed the projected ranges of ions in the amorphous counterparts of these materials[49,50,60,62,63,64,67]. Various mechanisms have been suggested to explain the occurrence of these unexpectedly deep damage ranges. Both

channeling of ions as well as thermal migration of interstitials created by the incident beam have been considered as possible causes. The directionally dependent propagation of defects to depths exceeding the projected ion ranges by way of a compressive stress field, set up due to the thermal spike phenomenon, has also been proposed.

In order to obtain some insight into the relevance of these three possible mechanisms it is necessary to study as many as possible variables which may have an effect on the level and range distribution of implantation–induced radiation damage. The influence of factors such as ion energy, ion dosage, tempo of implantation as well as the effect of different ions in various metals, have been studied.[63,64,65,67] In the current work the temperature dependence of radiation damage is investigated.

Rutherford backscattering spectra of alpha particles dechanneled at radiation–induced defect structures were obtained to investigate both the range and level of the radiation damage. In order to analyse these spectra effectively it is necessary to have an understanding of concepts such as backscattering, energy loss and channeling. These phenomena are discussed in the first three chapters of this book. Chapter 4 investigates the various crystal structures of relevance to this study as well as the type of defects which are likely to be produced as a result of ion bombardment. The dechanneling of alpha particles at various defect structures is investigated in Chapter 5, while Chapter 6 contains a review of various experimental investigations and computer simulations which have led to a greater understanding of ion–induced radiation damage. Chapter 7 describes the experimental set–up used in the current investigation and Chapter 8 contains the various experimental results and a discussion thereof.

ACKNOWLEDGEMENTS

I wish to thank the following persons for their help, advice and encouragement:

Prof E K H Friedland, Prof H W Alberts, Mrs C J Vos (for the typing), Mr P C Nawrotzki, Mr R van Weele, Mr A M F M van der Kallen, Kim Weimer, Mrs A Schickerling, my family and my husband Andrew.

CONTENTS

page

CHAPTER 1

BACKSCATTERING

1. INTRODUCTION

The components of a typical experimental system used for backscattering analysis are illustrated in fig. 1.1. An ion source generates a beam of charged particles which, after acceleration (in e.g. a Van der Graaff accelerator), energy selection and collimation, impinges upon a target mounted in an evacuated chamber.
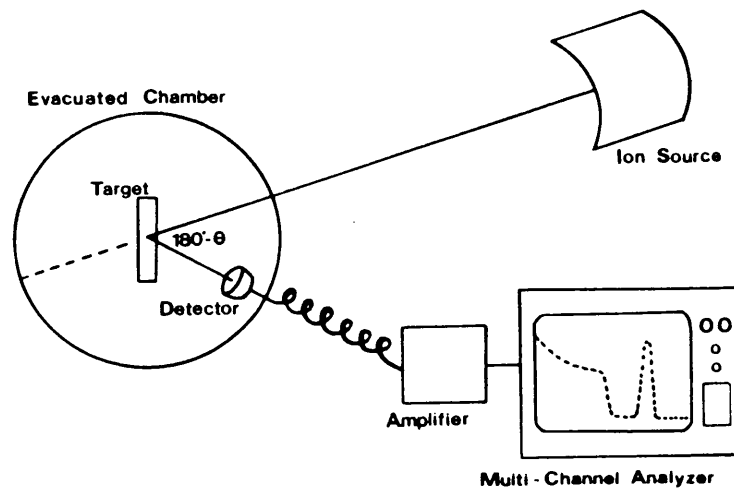
Figure 1.1   A Rutherford backscattering experiment.

Almost all incident particles penetrate the target material and eventually come to rest due to electronic and nuclear stopping processes. (If the target is thin they may be transmitted through to the other side.) Only a very small fraction (much less than 10^{-4}) of the incident particles will undergo large angle ($>90°$) scattering collisions with target atoms. This large angle scattering is known as Rutherford backscattering (RBS) and can occur at the surface or at a depth t below the target surface.

Of these backscattered particles only a fraction will be in an alignment favourable for impingement on a detector system (e.g. a surface barrier detector) placed at an angle θ with the incident beam direction. The amount of backscattered particles detected will be dependent on the solid angle underspanned by the detector.

The output of the detector is an analogue signal, the magnitude of which is proportional to the energy of the detected particle. After amplification, a multichannel analyzer (MCA) (which can contain thousands of "channels") measures the signal and registers its magnitude as a count in an appropriate channel corresponding to the energy of the detected particle.

During the collection of an increasing amount of counts, the graphic display of the MCA gradually "builds" a spectrum of counts vs. channel number. The relation between channel number and energy of the corresponding detected particle is a characteristic of the system and can be determined experimentally. The MCA spectrum can then be interpreted as a plot of "backscattering yield" vs. energy of backscattered particles.

An MCA spectrum contains information leading to elemental identification, depth determination and quantitative analysis of the target material.

2. KINEMATIC FACTOR

The energy of a backscattered particle, before and after interaction with the target material, differs. This is due to the fact that, even if elastic

collisions are assumed, the incident particle transfers energy to target atoms and is consequently slowed down. The ratio of projectile energy E_1 detected after a backscattering incident to that of its incident energy E_0 is described by the kinematic factor, K:

$$K = \frac{E_1}{E_0} \qquad 1.1$$

An expression for the kinematic factor as a function of projectile and target masses and backscattering angle may be derived. This definition assumes an elastic collision between projectile and target, which is valid if the projectile energy, E_0, is much larger than the binding energy of target atoms (1–10 eV). Nuclear reactions must also be negligible. Incident beams must therefore not have energies higher than 2–3 MeV.
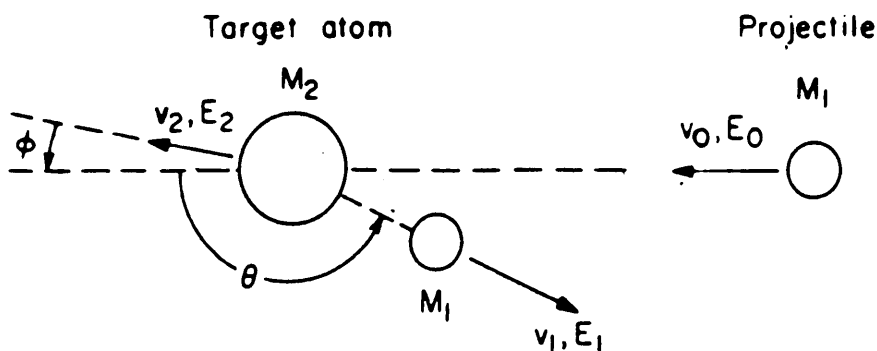
Figure 1.2 (Ref. 7f) An elastic collision

As illustrated in figure 1.2, particle 1 with mass M_1 travelling at a constant velocity v_0, collides elastically with a stationary target particle 2 with mass M_2. Some of the kinetic energy of the incident particle is transferred to the target atom so that after collision each particle moves

away at a different velocity and at different angles: Particle 1 is scattered by an angle θ with the incident direction and possesses a velocity v_1 after interaction. Particle 2 (the recoil atom) moves away with velocity v_2 at an angle ϕ.

Assuming the collision to be elastic, conservation of energy and momentum lead to equations 1.2, 1.3 and 1.4.

Energy:
$$\frac{1}{2} M_1 v_0^2 = \frac{1}{2} M_1 v_1^2 + \frac{1}{2} M_2 v_2^2 \qquad 1.2$$

Momentum parallel with incident beam:
$$M_1 v_0 = M_1 v_1 \cos \theta + M_2 v_2 \cos \phi \qquad 1.3$$

Momentum normal to incident beam:
$$0 = M_1 v_1 \sin \theta - M_2 v_2 \sin \phi \qquad 1.4$$

Eliminating ϕ and v_2 one obtains:

$$\frac{v_1}{v_0} = \frac{(M_2^2 - M_1^2 \sin^2 \theta)^{\frac{1}{2}} + M_1 \cos \theta}{M_1 + M_2}$$

This leads to the following expression for the kinematic factor:

$$K = \frac{E_1}{E_0} = \frac{\frac{1}{2}M_1 v_1^2}{\frac{1}{2}M_1 v_0^2} = \left[\frac{(M_2^2 - M_1^2 \sin^2 \theta)^{\frac{1}{2}} + M_1 \cos \theta}{M_1 + M_2}\right]^2$$

Therefore
$$K = \left\{\frac{[1-(\frac{M_1}{M_2}) \sin^2 \theta]^{\frac{1}{2}} + (\frac{M_1}{M_2}) \cos \theta}{1 + (\frac{M_1}{M_2})}\right\}^2 \qquad 1.5$$

The kinematic factor for a certain target/projectile combination is therefore independent of the energy of the projectile and varies only with changes in M_1, M_2 and scattering angle of the incident ion.

Tables containing kinematic factors for various θ (90–180°) are found in the literature[7a]. These tables exist for both H and He ions incident on targets with atomic masses ranging from 6 to 216.

3. SCATTERING CROSS SECTION (σ)

Only a small percentage of particles constituting an energetic beam incident on a target will undergo large angle (Rutherford) backscattering. Of these, only a fraction will eventually appear at the detector.

The probability that a collision will result in a detected particle is given by the differential scattering cross section, $\frac{d\sigma}{d\Omega}$. This concept may be explained along with fig. 1.3:
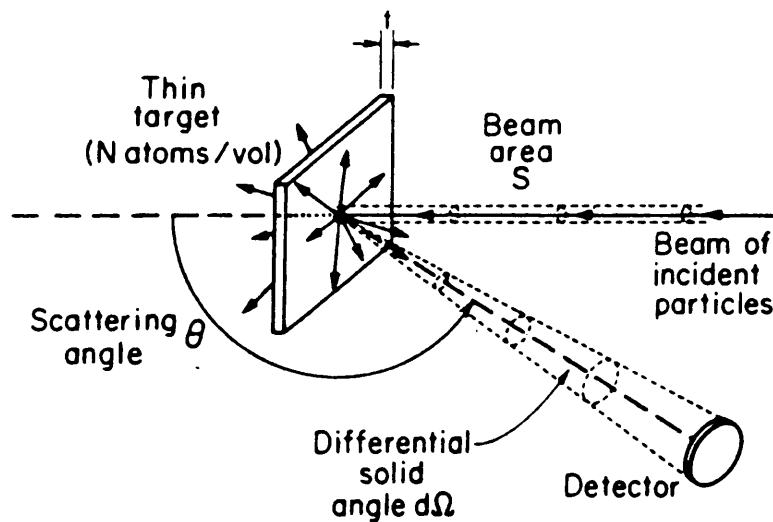
Figure 1.3 (Ref. 7g) Backscattered particles reaching the detector constitute a solid angle d Ω.

As can be seen from this illustration, only particles backscattered within the solid angle spanned by the detector will be counted. The differential scattering cross section is then given by:

$$\frac{d\sigma}{d\Omega} = \frac{1}{Nt} \left[\frac{dQ}{d\Omega} / Q\right] \qquad 1.6$$

where:

Q = number of particles that hit the target

dQ = number of particles recorded by the detector

N = volume density of target atoms

t = thickness of the target

Nt = number of target atoms per unit area

dΩ = the differential solid angle of the detector

This definition implies that the solid angle $d\Omega$ is so small that the scattering angle θ is well–defined. It also assumes minimal target thickness (so that energy loss phenomena need not be taken into account).

The dimension of the differential scattering cross section is that of an area. One can imagine that each nucleus of an atom presents on area $\frac{d\sigma}{d\Omega}$ to the beam of incident particles. A summation of $\frac{d\sigma}{d\Omega}$ for all the atoms in the exposed area will result in the total value for the probability of detection.

The concept of integral scattering cross section (Σ) is defined for when one wishes to describe the probability of a scattering event being detected within a finite solid angle, Ω:

$$\Sigma = \int_{\Omega} \left(\frac{d\sigma}{d\Omega}\right) d\Omega \qquad 1.7$$

In backscattering spectrometry the solid angle Ω of a typical detector system using a surface barrier detector is in the order of 10^{-3} to 10^{-2} sr. The relative smallness of this solid angle causes the scattering angle θ to be well–defined.

It can be shown[7c] that near $\theta = 180^\circ$ the scattering cross section is furthermore not strongly influenced by changes in the scattering angle. For a detector angle near 180° an average scattering angle value (taken as the angle between the incident beam direction and the central axis of the detector) is sufficiently accurate for small detector solid angles (10^{-2} to 10^{-3} sr).

The average scattering cross section is defined as:

$$\sigma \; = \; \frac{1}{\Omega} \int_\Omega (\frac{d\sigma}{d\Omega})d\Omega \qquad\qquad 1.8$$

and it follows that σ tends to $\frac{d\sigma}{d\Omega}$ in the limit of very small detector angles.

The following formula by Rutherford[7b] enables one to calculate the differential scattering cross section with respect to centre–of–mass co–ordinates:

$$(\frac{d\sigma}{d\Omega})_{CM} \; = \; \left[\frac{z_1 z_2 e^2}{4E_{CM} \sin^2(\frac{\theta_{CM}}{2})} \right]^2 \qquad\qquad 1.9$$

where CM indicates that values are given with respect to centre–of–mass co–ordinates, E is the energy of the projectile immediately before scattering and $e^2 \; = \; 1{,}4398 \; \times \; 10^{-13}$ MeVcm.

This formula can be transformed to the laboratory frame of reference to yield:

$$\frac{d\sigma}{d\Omega} = \left(\frac{z_1 z_2 e^2}{4E}\right)^2 \cdot \frac{4}{\sin^4\theta} \cdot \frac{\left\{\left[1 - \frac{M_1}{M_2}\sin\theta\right]^{\frac{1}{2}} + \cos\theta\right\}^2}{\left[1 - \left(\frac{M_1}{M_2}\sin\theta\right)^2\right]^{\frac{1}{2}}} \qquad 1.10$$

This equation is only accurate for $M_1 << M_2$ which is sufficient for the purposes of this study.

An example of the use of the differential scattering cross section for a typical experimental set-up follows:

A surface barrier detector spans 2×10^{-3} sr and makes an angle $\theta = 165°$ with respect to the incident beam. The integrated current of a beam of 1,5 MeV alpha particles ($z_1 = 2$; $M_1 = 4$ g/mol) incident on a copper sample ($z_2 = 29$; $M_2 = 63,5$ g/mol) is $12000 \times 3 \times 10^{-10} = 3,6 \times 10^{-6}$C. (The Cu sample is assumed to be amorphous.)

The total amount of α^+-particles incident on the copper sample is:

$$\frac{3,6 \times 10^{-6}\text{C}}{1,6 \times 10^{-19}\text{C}} = 4,5 \times 10^{13}$$

The $\frac{d\sigma}{d\Omega}$ for laboratory co-ordinates can be calculated from equation 1.10 to yield a value of $1,2 \times 10^{-24}$ cm^2/sr.

Each nucleus of the Cu target therefore presents an area of $1,2 \times 10^{-24}$ cm^2 per sr of the detector solid angle; therefore effectively an area of $1,2 \times 10^{-24} \cdot 2 \times 10^{-3} = 2,4 \times 10^{-27}$cm^2. Thus the total number of detected alpha particles backscattered from just the surface monolayer of the copper

(which has an areal density of roughly 2×10^{15} atoms cm^{-2}) is:

$$2,4 \times 10^{-27} \text{cm}^2 \cdot 2 \times 10^{15} \text{ atoms cm}^{-2} \cdot 4,5 \times 10^{13}$$

$$= \quad 216 \text{ atoms.}$$

If one takes into account the fact that most alpha particles will penetrate the target, and that for each successive monolayer traversed there exists a certain probability for RBS and subsequent detection, one would expect the detected RBS yield to be very much more than predicted by this simple calculation for a surface monolayer.

It can be seen from equation 1.10 that the probability for detection of a backscattered particle increases with decrease in the energy of the particle immediately before being backscattered. Due to energy loss, increasing projectile penetration will therefore result in an increase in RBS yield from each successive monolayer traversed.

Another aspect that arises from the energy dependence of the RBS yield, is how this influences the choice of total integrated beam current for a specific incident energy. In this study alpha particle beams with incident energies of 1,5 and 1,8 MeV were used. Integrated currents for the 1,8 MeV beams had to be 1,5 times larger than those for the 1,5 MeV beams in order to collect comparable backscattering yields.

4. ENERGY TO DEPTH CONVERSION

The amount of slowing down experienced by an energetic particle as it traverses a target is dependent on its instantaneous energy at each point in the material.

Energy loss or "stopping power" is defined by

$$\lim_{\Delta x \to o} \frac{\Delta E}{\Delta x} \equiv \frac{dE}{dx}(E) \qquad 1.11$$

As the incident particle is constantly losing energy to the material it is traversing, the stopping power is constantly changing. There is not a simple linear dependence of particle energy to depth of penetration. Various approximations can however be made when relating the measured energy of a backscattered particle to the depth at which the RBS incident took place.

A more commonly used concept used in describing energy loss in the "stopping cross section", ε:

$$\varepsilon = \frac{1}{N}\frac{dE}{dx} \qquad 1.12$$

where N is the atomic density of the target material. The use of ϵ is preferred because, as opposed to $\frac{dE}{dx}$, ε stays constant for materials of the same z but different atomic packing (and therefore different densities).
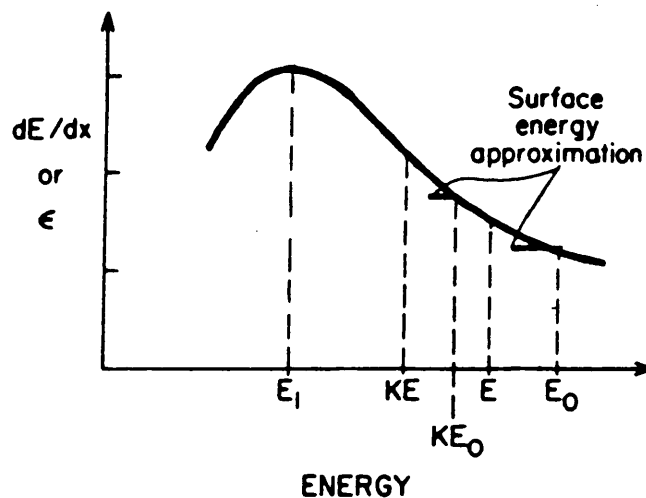
Figure 1.4 (Ref. 7h) The energy dependence of the stopping power.

Energy loss will be described in more detail in the next chapter. For the purposes of the ensuing discussion it is assumed that data of stopping power (or stopping cross section) as a function of projectile energy is available. A typical dependence of $\frac{dE}{dx}$ on E is illustrated in figure 1.4.

Figure 1.5 shows a particle beam of energy E_0 incident on a mono–elemental target surface at an angle θ to the normal. Particles undergoing RBS at the surface are scattered with energy KE_0 as indicated. A particle penetrating the target progressively loses energy, so that at a depth x it possesses energy $E < E_0$. Immediately after undergoing a large angle back–scattering event at x (resulting in its changing direction and travelling back to the surface at an angle θ_2 with the normal direction), the particle possesses an energy KE. It then progressively loses more energy before finally emerging with energy E_1; it is this energy that is finally recorded by the detector system.
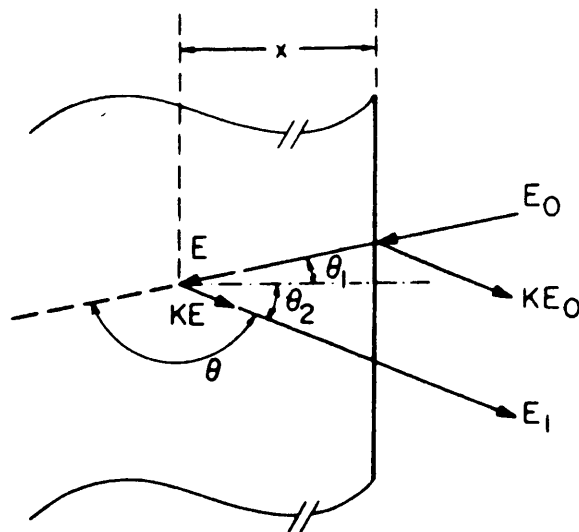
Figure 1.5   (Ref. 7i)   Backscattering at a point x within the target material.

The scattering angle, θ (see figure 1.5) is given by:

$$\theta = 180^\circ - \theta_1 - \theta_2 \qquad\qquad 1.13$$

The energy lost by the incident particle as it travels up to a depth x inside the material is given by:

$$E_0 - E = \int_0^x \left(\frac{dE}{dx}\right)dx \qquad\qquad 1.14$$

For evaluation of this integral, $\frac{dE}{dx}$ needs to be known as a function of x. Energy loss data is however usually given as a function of energy (see figure 1.4). If x is regarded as a function of E, then

$$dx = \frac{dx}{dE}(E)\cdot dE$$

from which follows:

$$x = \int_{E_0}^{E} \left(\frac{dx}{dE}\right)dE = \int_{E_0}^{E} \left(\frac{dE}{dx}\right)^{-1} dE \qquad\qquad 1.15$$

Referring to figure 1.5, one obtains for energy loss of the particle along its inward path:

$$\frac{x}{\cos\theta_1} = -\int_{E_0}^{E} \left(\frac{dE}{dx}\right)^{-1} dE \qquad\qquad 1.16a$$

13

and for energy loss along the outward path of the particle:

$$\frac{x}{\cos\ \theta_2}\ =\ -\int_{KE}^{E_1}(\frac{dE}{dx})^{-1}dE \qquad\qquad 1.16b$$

The energies involved in these two equations are indicated in figure 1.5.

As $\frac{dE}{dx}$ is constantly changing with energy, the term under the integral in equations 1.16 is not a constant. Substitution of a certain value of $\frac{dE}{dx}$ however greatly simplifies the solution of these equations. The problem arises as to which value of $\frac{dE}{dx}$ will give the best approximation.
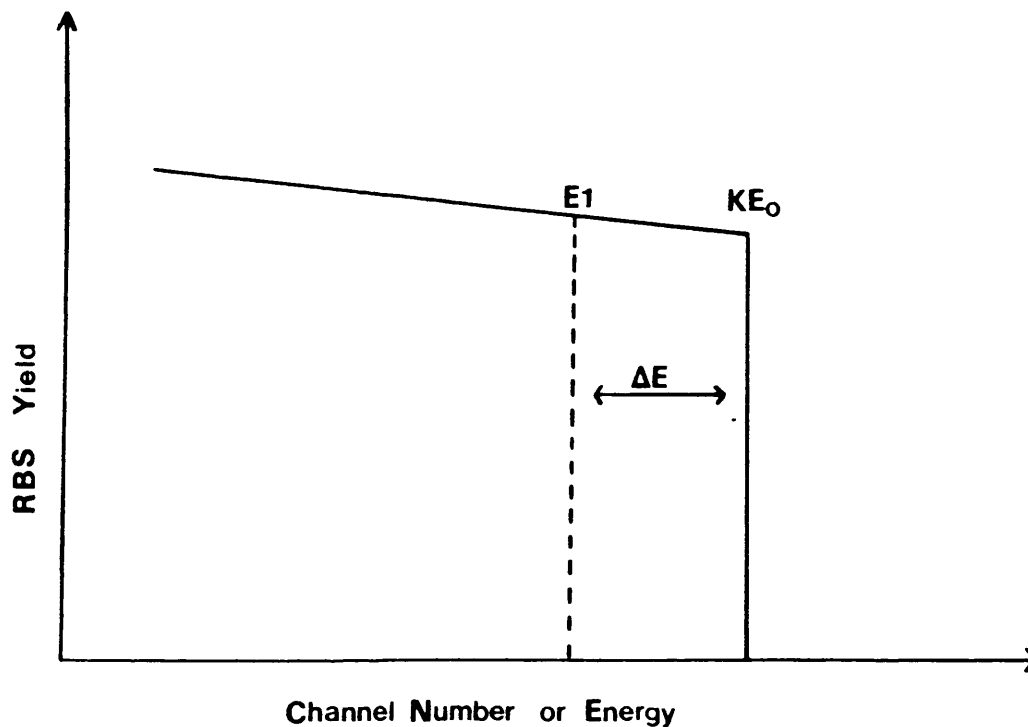
Figure 1.6 An idealistic backscattering spectrum.

The "Surface Approximation" (used in the analysis of data obtained in this study) is adequate for RBS taking place in the uppermost or surface region of the target. This approximation involves the substitution of the $\frac{dE}{dx}$ value corresponding to E_0 in equation 1.16a, and the $\frac{dE}{dx}$ value corresponding to KE_0 in equation 1.16b.

After rearrangement one then obtains for the inward path:

$$E = E_0 - \frac{1}{\cos \theta_1} \left.\frac{dE}{dx}\right|_{E_0} \qquad \text{1.17a}$$

and for the outward path:

$$E = KE - \frac{x}{\cos \theta_2} \left.\frac{dE}{dx}\right|_{KE_0} \qquad \text{1.17b}$$

Elimination of E from both these equations yields:

$$\Delta E = x \left\{ \frac{1}{\cos \theta_2} \left.\frac{dE}{dx}\right|_{KE_0} + \frac{K}{\cos \theta_1} \left.\frac{dE}{dx}\right|_{E_0} \right\} \qquad \text{1.18}$$

where
$$\Delta E = KE_0 - E_1$$

An example of an idealistic MCA spectrum resulting from the backscattering just described, is illustrated in figure 1.6. The steep edge of the spectrum corresponds to the energy, KE_0, of particles backscattered from the target surface. The energy E_1, which corresponds to backscattering at depth x in the material, is indicated at a lower channel number.

After experimental determination of the relationship between channel number and energy, $KE_0 - E_1 = \Delta E$ can be read off from the spectrum.

Equation 1.18 then enables one to determine the depth corresponding to any channel number or energy:

$$x = \frac{\Delta E}{[S]} \qquad\qquad 1.19$$

where

$$[S] = \frac{1}{\cos \theta_2} \left.\frac{dE}{dx}\right|_{KE_0} + \frac{K}{\cos \theta_1} \left.\frac{dE}{dx}\right|_{E_0} \qquad\qquad 1.20$$

[S] is called the "energy loss factor".

An equivalent set of equations can be given in terms of the stopping cross section:

$$x = \frac{\Delta E}{[\varepsilon] N} \qquad\qquad 1.21$$

where $[\varepsilon] = \dfrac{1}{\cos \theta_2} \varepsilon(KE_0) + \dfrac{K}{\cos \theta_1} \varepsilon(KE_0)$ $\qquad\qquad 1.22$

5. ENERGY STRAGGLING AND SYSTEM RESOLUTION

In figure 1.7 a beam of identical particles, all with energy E_0, are incident on a target of thickness Δx. Ideally all transmitted particles should possess exactly the same energy, say E_1, when emerging from the back surface of the target. Due to statistical fluctuations, however, the energy loss of each particle is not the same. (Fluctuations are caused by the varying amount of interactions with different impact parameters.) Instead, transmitted particles possess a range of energies, spread around the mean value E_1.

This uncertainty in energy is called "energy straggling" and places a finite limit on the precision of depth resolution in both transmission and backscattering spectrometry.
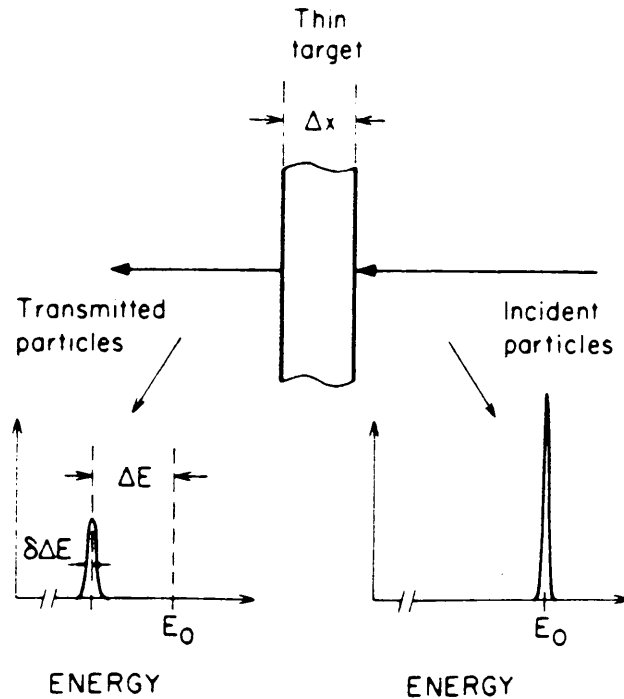
Figure 1.7 (Ref. 7j) Transmitted or backscattered particles possess a range of energies due to statistical fluctuations.

For ion velocities large compared with the orbital electron velocities of the target atoms, Bohr[8] derived the following expression for energy straggling with the help of a simple classical model:

$$\Omega_{\sim B}^2 = 4\pi \left(z_1 e^2\right)^2 N z_2 \Delta x \qquad \textbf{1.23}$$

where $\Omega_{\sim B}^2$ is the Bohr value of the energy straggling and represents the mean square value of the energy variation. Values of $\Omega_{\sim B}^2/N\Delta x$ for He straggling in

the metals of interest to this study, are for iron 27,05 ; for nickel 29,13 ; for copper 30,17 and for Pt 81,16 $\left(\text{in units of } 10^{-12} \text{ (eVcm)}^2\right)$.

Bohr's expression is independent of projectile energy. An increasing energy dependence of $\Omega_{\sim\text{B}}$ is however predicted for decreasing ion velocities due to the increasing importance of atomic charge distributions at lower energies. Both Chu[9,10] and Lindhard and Scharff[11] predicted an appreciable reduction of the straggling width for alpha particles below 4 MeV, especially for high atomic number target materials. Friedland and Lombard[12] found the correction factors not to be necessary for 1–2 MeV alpha particle straggling in Al, Ni and Au.

Bohr's theory further predicts a Gaussian distribution for energy straggling. This has proved to be an adequate description for alpha particle energy straggling in the 1–2 MeV range[7d]. The Gaussian energy straggling distribution is described by:

$$\left(2\pi\Omega_{\sim\text{B}}^2\right)^{-\frac{1}{2}} \exp \left[-\frac{x^2}{2\Omega_{\sim\text{B}}^2}\right] \qquad\qquad 1.24$$

In a channeling direction, energy straggling may be increased due to the variation in the stopping of channeled particles depending on their angle of incidence with respect to the channeling axis. (This is discussed in Chapter 3 section 9.)

All the possible factors which may cause an uncertainty or spread in the energy involved in a backscattering process (and which can influence the

eventual shape of the spectrum) are summarized as follows:

- The incident beam may not be monoenergetic, and can then be described by an energy profile with a standard deviation $\underset{\sim}{\Omega}_{Beam(1)}$. After a backscattering incident in the material this factor reduces to $K\underset{\sim}{\Omega}_{Beam(1)}$.

- The beam energy diverges slightly between the source and the point of interaction, contributing a standard deviation $K\underset{\sim}{\Omega}_{Beam(2)}$.

- Limitations of the energy resolution of the detection system and electronics contributes a standard deviation of $\underset{\sim}{\Omega}_{Det}$.

- Due to the finite value of the surface area of the detector (and therefore also the angle it underspans), an uncertainty can occur in the precise value of the kinematic factor employed, causing a "kinematic" contribution to the standard deviation in energy, $\underset{\sim}{\Omega}_{Kin}$.

- Along the incident path energy straggling causes the analyzing beam to have a standard deviation in energy of $\underset{\sim}{\Omega}_{In}$.

- Along the outward path energy straggling causes a standard deviation, $\underset{\sim}{\Omega}_{Out}$, in the energy of the beam.

The total uncertainty in energy, $\underset{\sim}{\Omega}_{Tot}$, of particles represented in an RBS spectrum may then be expressed as follows:

$$\underset{\sim}{\Omega}_{Tot} = \sqrt{\underset{\sim}{\Omega}_s^2 + \underset{\sim}{\Omega}_r^2} \qquad \text{1.25a}$$

where

$$\underset{\sim}{\Omega}_s^2 = K^2\underset{\sim}{\Omega}_{In}^2 + \underset{\sim}{\Omega}_{Out}^2 \qquad \text{1.25b}$$

and represents the variance due to energy straggling

$$\text{and} \qquad \underset{\sim}{\Omega}_r^2 \;=\; K^2\!\left(\underset{\sim}{\Omega}_{\text{Beam}(1)}^2 + \underset{\sim}{\Omega}_{\text{Beam}(2)}^2\right) + \underset{\sim}{\Omega}_{\text{Det}}^2 + \underset{\sim}{\Omega}_{\text{Kin}}^2 \qquad 1.25c$$

where $\underset{\sim}{\Omega}_r^2$ represents the variance due to system resolution.

Even in the absence of energy straggling the system resolution causes a finite spread in the energies of detected particles as represented on an RBS spectrum. This may be understood by observing the high energy edge of such a spectrum (which represents the energy of particles backscattered from the surface of the target and which therefore did not penetrate and undergo energy straggling). Figure 1.8 shows the less steep gradient of the high energy edge that is obtained in practice as opposed to the idealistic sharp edge illustrated in figure 1.6. One might expect KE_0 to be represented by a single channel (due to the absence of energy straggling), but instead there exists an uncertainty in the precise value of KE_0 which is spread over a number of channels. This is due to the limits of the system resolution. In practice the value of KE_0 is taken to be the energy corresponding to the channel number where the RBS yield is halfway between the minimum and maximum values of the sharp edge.
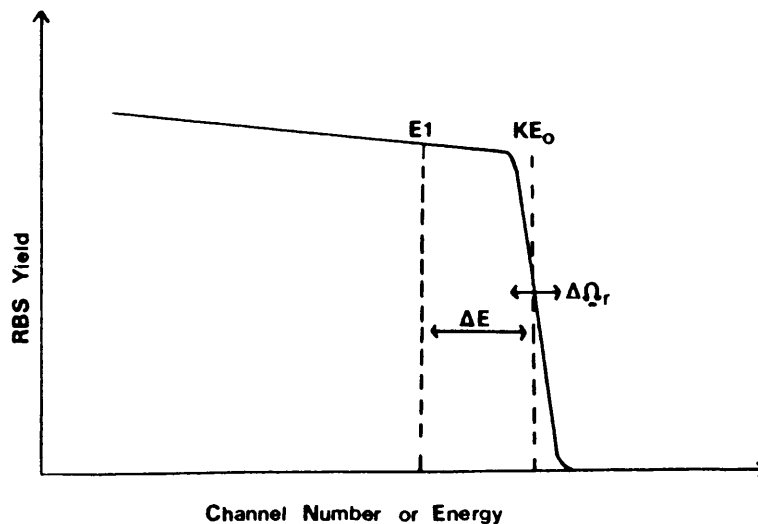
Figure 1.8   The leading edge of the spectrum is less sharp due to limitations of the system energy resolution.

It is possible to use the high energy edge to determine the magnitude of the system resolution $\underset{\sim}{\Omega}_r$. If, say, each channel represents 3 keV and the RBS yield rises from a minimum to half its maximum value over four channels, then $\underset{\sim}{\Omega}_r = 3 \times 4 = 12$ keV.

Since the standard deviations associated with energy straggling $(\underset{\sim}{\Omega}_s)$ and system resolution $(\underset{\sim}{\Omega}_r)$ add up quadratically, the resulting total standard deviation in energy $(\underset{\sim}{\Omega}_{Tot})$ is usually determined predominantly by one of these two processes. For backscattering close to the surface, system resolution plays the greater role. The deeper the occurrence of the back-scattering event however, the more energy straggling takes place and the larger the contribution of $\underset{\sim}{\Omega}_s$ to $\underset{\sim}{\Omega}_{Tot}$ ($\underset{\sim}{\Omega}_r$ stays constant). From this discussion it is also clear that energies become increasingly ill–defined whilst progressing to lower channel numbers on the RBS spectrum.

The error in depth determinations from RBS spectra can be calculated when the total standard deviation in energy is known by placing this value into equation 1.19:

$$\delta x = \frac{\underset{\sim}{\Omega}_{Tot}}{[S]} \qquad\qquad 1.26$$

CHAPTER 2

ENERGY LOSS AND RANGES OF IONS IN AMORPHOUS MATERIALS

1. INTRODUCTION

Most energetic ions incident on a target will penetrate the material and progressively slow down as their kinetic energy decreases due to various types of interaction with the surrounding material. Each ion will eventually come to rest at a certain depth if the material is thick enough so as not to allow transmission through the back surface of the target.

Due to statistically distributed scattering centres and various quantum mechanical properties for electronic excitation and ionization, identical incident ions are not all stopped at the same depth in a material. A beam of identical ions injected into a target will therefore cause a certain final distribution of particles after all projectiles have come to rest. The "range distribution" is defined as the probability density for finding a particle at rest in a given position inside the target. Range profiles for amorphous materials are approximately Gaussian in shape. Departures from such distributions are observed in materials possessing crystalline ordering. (See the next chapter.)

It is evident that the range distribution will depend on the stopping power (or energy loss) of a specific ion/target/energy combination.

Energy loss is a complex function of various factors such as:

- the atomic numbers of both projectile and target

- the density of the target material

- the energy of the incident ion

- the charge distribution around the incident ion (which is a function of its velocity)

- the periodic nature of lattice structure.

Due to the many variables involved and due to the many types of interaction causing energy loss, a precise theoretical formulation that accurately predicts the amount of energy lost for any ion/target/energy combination is extremely difficult. The most unified theoretical description of stopping and range of ions with velocities lower than the Thomas Fermi velocity[13] has been done by Lindhard, Scharff and Schiott[14]. Ions of higher energies are well described by the Bethe–Bloch stopping formalism[15,16]. Ziegler[17] has combined various stopping theories for ions with energies in the medium range, to experimental stopping data and obtained very useful "universal stopping curves" for the stopping of H and He in various targets. The various numerical methods using computer simulations (Monte Carlo calculations) are providing increasingly accurate range predictions.

The theories and methods mentioned above will (among others) be briefly discussed in this chapter. The various factors influencing energy loss will also be looked into in more detail.

2. PROCESSES LEADING TO ENERGY LOSS: ELECTRONIC AND NUCLEAR STOPPING

Incident particles lose their energy primarily by a succession of Coulomb interactions with target atoms; though at very high energies (GeV range for

protons), energy losses due to nuclear excitations become significant. For the projectiles and energy range of interest to this study the two dominant processes of energy loss are, however:

(a) **Electronic stopping:** Energy is lost due to the interactions of the moving ion with bound or free electrons in the target. This stopping is due to a "frictional resistance'" the projectile encounters as it passes through the electron clouds surrounding each target atom. Electronic collisions may be elastic or inelastic, but because the electronic structure of a metal can quickly recover, no permanent damage remains after this type of interaction. The energy transferred to electrons is largely dissipated as heat.

(b) **Nuclear stopping:** Energy loss occurs due to the interactions of the moving ion with the screened or unscreened nuclei of the target atoms. Stopping occurs by way of a multitude of small–angle elastic scattering collisions of the projectile with the target nuclei. (Inelastic nuclear collisions only occur at very high energies beyond the energy range used in this study.) A component of the ion energy lost to nuclei is used to cause an increase in the lattice–vibrational behaviour of target atoms around their lattice sites (constituting the "phonon energy"). This energy is also dissipated as heat but not as quickly as that of the electronic dissipation. Damage due to nuclear interactions is readily incurred in the energy range used in this study and is investigated in more detail in a later chapter.

For high energy light ions (like protons) energy loss due to electronic excitation plays the dominant role. Nuclear (quasi–elastic) collisions are of

less importance in *energy loss*, but do, however, still play a role (though minor) in multiple scattering (deflection) of these particles. The slower and heavier the ion the more it is influenced by the nuclear component of stopping as regards both energy loss *and* multiple scattering; slower heavier ions are therefore deflected further and also lose more energy to the target due to nuclear collisions. A relatively heavy ion such as argon is therefore expected to induce significantly more radiation damage (e.g. displacements of target atoms from their lattice sites) than one would expect for a light ion such as H^+ or He^+.

From the above discussion it is obvious that the range distribution of both light and heavy ions is dependent on two separate processes: energy loss and scattering[14]. Except for very low incident energies (order of eV) electronic excitation is the main cause of energy loss. The nuclear interactions serve mainly to cause increasing scattering (thereby enhancing lateral spread but generally decreasing the range as a whole) the slower and heavier the ion.

The total stopping cross section can be viewed as a linear combination of both nuclear and electronic contributions[7c]:

$$S_{Tot} = S_e + S_n \qquad\qquad 2.1$$

The separation of the energy loss into two separate components ignores any possible correlation between the two; this correlation is probably not significant when many collisions are averaged over[18a].

The "perturbation approximation" serves to highlight two important

25

aspects of stopping and will therefore briefly be discussed. Figure 2.1 illustrates various parameters involved in the interaction between projectile and target. The projectile has mass M_1, charge z_1e and velocity v_0 before interaction, whilst the target atom, with mass M_2 and charge z_2e, is stationary. After interaction the energy transferred to the target atom has components both normal and parallel to the incident direction; the normal component being:

$$E_\perp = \left(\frac{2}{M_2}\right) \cdot \left(\frac{z_1 z_2 e^2}{p v_1}\right)^2 \qquad\qquad 2.2$$

where p is the "impact parameter", i.e. the distance of closest approach between two particles if the mass M_2 were held fixed in place while the projectile flew past along a straight trajectory. v_1 is the velocity of the incident particle after interaction.
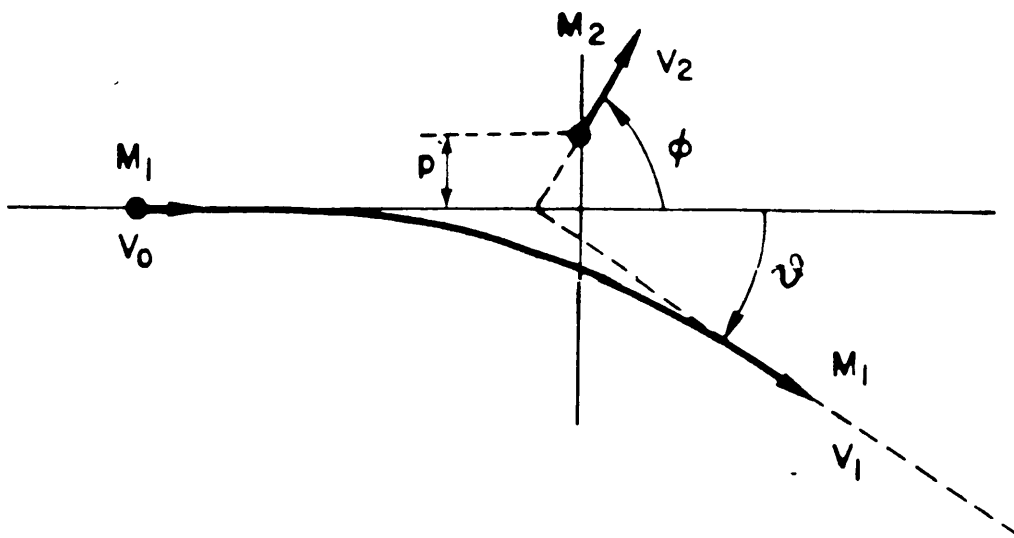
Figure 2.1   (Ref. 18c)   An elastic collision with impact parameter p.

For small perturbations (i.e. for incident energies where electronic stopping plays the dominant role) the total energy lost to the projectile is very close to $E_\perp$. Keeping this in mind and referring to equation 2.2, two significant observations can then be made:

(i)   It is evident that electrons (with much smaller mass) absorb more energy per encounter than nuclei.

(ii)   Note the proportionality of energy loss to the square of the charge on the ion.

3. THE ENERGY DEPENDENCE OF THE STOPPING CROSS SECTION

Typical stopping cross section plots for both nuclear and electronic stopping vs. energy are shown in figure 2.2.
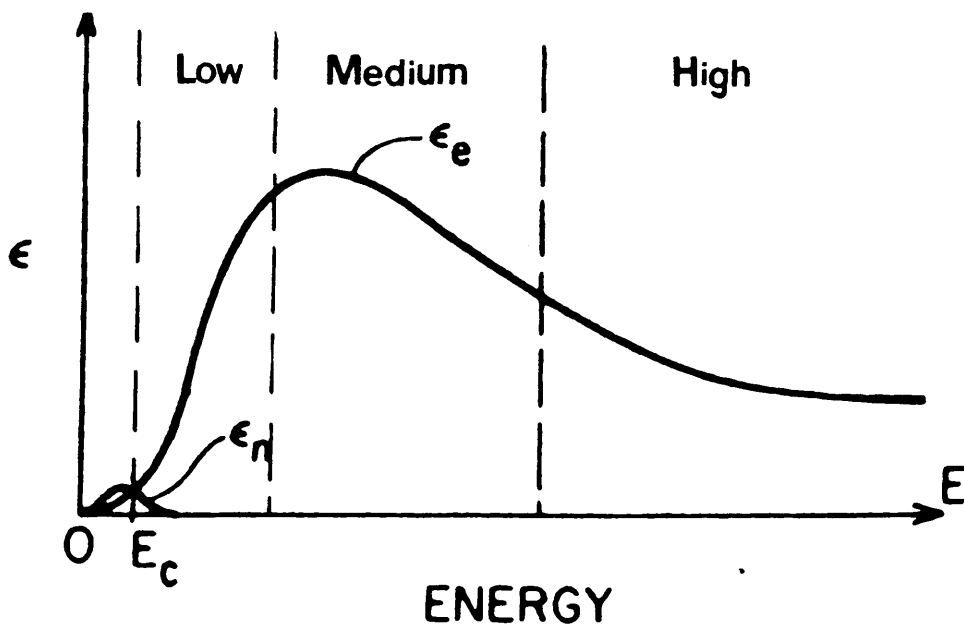
Figure 2.2 (Ref. 7e) The energy dependence of nuclear and electronic stopping.

(i)   **The very low energy region (eV range):**   Nuclear and electronic stopping are comparable in this region.   Due to the fact that this study involves particle interactions in the keV and MeV ranges, the contribution of nuclear stopping will not be discussed in detail. (The significant contribution of nuclear interactions to the *scattering* of particles must, however, be kept in mind.)

(ii)   **The very high energy region (GeV range):**   Stopping power increases due to the increasing role that nuclear reactions play at very high energies.   Stopping due to nuclear reactions is not indicated on figure 2.2 and is also not considered in this study.

(iii) **The high energy region (> 10 MeV):**   This range is well described by the Bethe–Bloch[15,16] stopping formalism where the energetic ion is considered to interact with an isolated atom consisting of a set of harmonic oscillators.   By using a simple model of scattering in a cloud of free electrons, Chu[7e] arrives at a result closely matching the Bethe–Bloch formula.   The complete formulation attributed to Bethe and Bloch is as follows:

$$Se = \frac{4\pi e^4 z_1^2 z_2}{m_e v^2}\left[\ln\frac{2m_e v^2}{<I>} - \beta^2 \ln(1-\beta^2) - \frac{c}{z_2} - \frac{\delta}{2}\right]\qquad 2.3$$

where S_e =   the electronic stopping cross section

        z_1, z_2 =   the atomic numbers of the projectile and target respectively

        I =   the mean ionization energy of target atoms

28

$$\beta^2 \quad = \quad \left(\frac{v}{c}\right)^2 \quad \text{where c is the velocity of light. The second}$$

and third terms in this formula are therefore

corrections due to relativistic effects

e, m = the electron charge and mass respectively

$\dfrac{c}{z_2}$ = a correction due to shell effects

$\dfrac{\delta}{2}$ = a density correction (only for very high energies)

Bohr[13] suggested that one might consider a heavy ion to be stripped of all electrons whose classical orbital velocities are less than the ion velocity. He derived the following velocity dependent expression for the fractional charge of a heavy ion:

$$\gamma \quad = \quad \frac{z_1^*}{z_1} \quad = \quad \frac{v_1}{v_0 z_1^{2/3}} \qquad\qquad 2.4$$

where γ = the ion fractional charge

z_1^* = the effective charge of the energetic ion

z_1 = the atomic number of the ion

v_1 = the velocity of the ion

v_0 = $\dfrac{e^2}{\hbar}$ ~ 2,2 x 10^8 cms^{-1}(the Bohr velocity)

Ions with velocities corresponding to the energy range of the Bethe–Bloch region are already fully stripped and therefore $z_1^* = z_1$. The minimum velocity where $z_1^* = z_1$ is called the Thomas Fermi velocity, v_{TF}, and may be obtained from equation 2.4 by setting $\gamma = 1$:

$$v_{TF} \quad = \quad v_0 z_1^{2/3} \qquad\qquad 2.5$$

Figure 2.2 also shows how the electronic stopping decreases when moving to higher energies in the Bethe–Bloch region. This is due to the fact that the higher the velocity of the ion, the less time it has to interact with each target atom it comes into contact with.

It is important to remember that an ion with incident energy corresponding to the Bethe–Bloch region will gradually lose more and more energy as it traverses the target so that it eventually will have energies corresponding to stopping powers in the medium, low and very low energy regions.

(iv) The low energy region (1 – 1000 keV)

Ions with energies in this range have velocities smaller than the Thomas Fermi velocity. It is more difficult to obtain a precise theoretical stopping formalism for these ions due to the fact that effective charges are not accurately known. The 150 keV Ar⁺ ions used for implantations in this study fall into this category. One may observe from figure 2.2 that the electronic stopping decreases proportionally with energy in this range. This is due to the increase in electron capture probability with decrease in ion velocity. Various models used for the determination of theoretical stopping powers in the low energy region will briefly be discussed.

(a) Firsov[19]: Electronic stopping of low velocity heavy ions (energies < 30 keV)

Firsov[19] proposed a semi–classical model wherein he considered two isolated atoms colliding with their undistorted electronic spheres penetrating each other. Using Thomas Fermi

atoms he was able to obtain electron distributions of the atoms and found that the electronic stopping cross section would increase proportionately to the heavy ion velocity.

(b)   Lindhard et al.[20]:   Electron gas model

For metal targets the low velocity energy loss is primarily caused by the conduction band electrons which may be accurately described by a free electron gas[18b].   In 1954 Lindhard et al.[20] presented a full treatment of a charged particle penetrating a free electron gas.   The following assumptions were made:

- the free electron gas consists of electrons at zero temperature on a fixed uniform positive background with overall charge neutrality.
- the initial electron gas is of constant density.
- the interaction of the charged particle is a perturbation on the electron gas.
- all particles are non–relativistic.

The electron plasma (of uniform density throughout) is divided into infinitesimal volume elements and the electronic stopping power is calculated for a particle interacting with each volume element.   The final stopping power, using this local density approximation, is then obtained by averaging over all these values, and may be expressed as follows:

$$Se \;=\; \int I(v,\rho)\left(z_1^*(v)\right)^2 \rho dV \qquad\qquad \textbf{2.6}$$

Where I = the stopping interaction function of a particle of unit charge with velocity v

ρ = the electronic density of the target

$z^*(v)$ = the effective charge of an ion with atomic number z_1

The electronic density of an atom is normalized so that its atomic number $z_2 = \int \rho dV$.

(c) **LSS theory:**[14] a unified approach

The approach of Lindhard, Scharff and Schiott[14] is commonly called the LSS theory. This work brought together all the pieces and bridging approximations made by various authors up to 1963, so that calculations of stopping and range distributions could, for the first time, be made with a single model. The LSS theory is applicable over the entire range of atomic species and energies up to the stopping power maximum; it is however (because of its being based on the Thomas Fermi model of the atom) most accurate for atoms with many electrons in the energy range where they are neither fully stripped nor almost neutral. Thus the LSS theory is applicable for the many–electron atom Ar in the low energy range currently being discussed. Disadvantages of the LSS theory is that it shows no shell effects and (as is the case for all the stopping theories discussed in this chapter) it does not take the effect of an ordered lattice structure into account.

The LSS theory may be briefly summarized as follows:

The range R and energy E of the interacting particle may be written in the following dimensionless variables:

$$\rho = R \cdot NM_2 \cdot \pi a^2 \cdot \frac{4M_1}{\left(M_1 + M_2\right)^2} \qquad\qquad 2.7$$

$$\varepsilon = E \cdot \frac{aM_2}{z_1 z_2 e^2 \left(M_1 + M_2\right)} \qquad\qquad 2.8$$

where ρ and ε are known respectively as the reduced range and the reduced energy

$$a = a_0 \cdot 0{,}8853 \left(z_1 + z_2\right)^{-\frac{1}{2}}; \quad a_0 \text{ is the Bohr radius:}$$

$$a_0 \sim 0{,}52916 \times 10^{-8} \text{ cm}$$

N = the atomic density of the target.

Using Thomas Fermi arguments the electronic stopping cross section was found to have the following proportionality to the velocity in the region $v < v_{TF}$:

$$Se = \xi_e \, 8\pi e^2 a_0 \left\{ \frac{z_1 z_2}{\left(z_1^{2/3} + z_2^{2/3}\right)} \right\} \cdot \frac{v}{v_0} \qquad\qquad 2.9$$

where $\xi_e \sim z_1^{1/6}$ and v_0 is the Bohr velocity.

Expressed in terms of the generalized quantities ε and ρ the electronic stopping may be expressed as:

$$\left(\frac{d\varepsilon}{d\rho}\right)_e = k\varepsilon^{\frac{1}{2}} \qquad\qquad 2.10$$

where
$$k = \xi_e \frac{0,0793 \, z_1^{\frac{1}{2}} z_2^{\frac{1}{2}} \left(M_1 + M_2\right)^{3/2}}{\left(z_1^{2/3} + z_2^{2/3}\right) \cdot M_1^{3/2} \, M_2^{3/2}} \qquad 2.11$$

Taking the nuclear stopping power $\left(\frac{d\epsilon}{d\rho}\right)_n$ also into account, integration of the inverse total stopping power, i.e. $\left[\left(\frac{d\epsilon}{d\rho}\right)_n + \left(\frac{d\epsilon}{d\rho}\right)_e\right]^{-1}$ then yields a simple but quite accurate estimate of the ion range (refer to equation 1.15). An example of reduced range versus energy curves for various values of k is illustrated in figure 2.3. The advantage of the unified LSS approach is that the parameters are chosen in such a way that any projectile/target combination can be represented as one point on the stopping power and range curves for each projectile energy (apart from the small differences introduced by different k–values). The LSS theory has been successful in predicting random stopping powers to an accuracy of 10–20%.
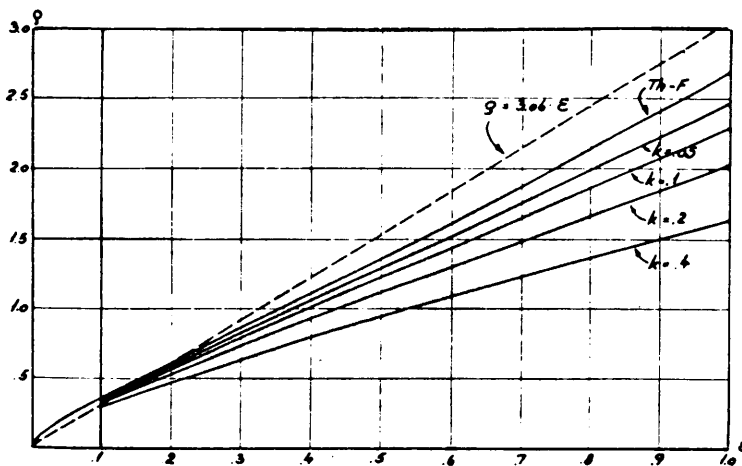
Figure 2.3 (*Ref. 14*) *Reduced range vs. reduced energy*

(v) The medium energy region (1 – 10 MeV)

As may be observed from figure 2.2 the electronic stopping

reaches a maximum in this energy range and then starts decreasing towards the Bethe–Bloch region. The medium energy range is of importance to this study due to the fact that it describes the stopping of the 1–2 MeV alpha particles used in channeling analyses. None of the theories used for the description of energy loss in the low energy region provides adequate explanations for experimentally observed stopping in the medium energy region. One reason for this could be the larger contribution of shell effects (which are ignored in the Thomas Fermi atomic model on which the LSS and Firsov theories are based). Because the Bethe–Bloch formalism also does not adequately describe the medium energy region, an accurate description can only be obtained by inter– and extrapolation of experimentally obtained data. This method was employed by Ziegler in his formulation of "Master Stopping Curves" for He ions incident on 92 different elemental targets[17].

Using a target independent scaling factor (the basic derivation of which is described at the end of this discussion) Ziegler was able to convert the much larger data base of hydrogen stopping powers to that of He stopping powers. Superimposing experimental He stopping data and scaled H stopping data, Ziegler was able to construct superior stopping curves for He ions.

Unluckily there were still areas on these plots for which no experimental data was available. Stopping data for these regions can be obtained if a theoretical stopping function is fitted between experimental data points on either side of the unknown area.

Theoretical stopping functions were obtained from the local oscillator model of Nesbet and Ziegler, as well as from an expansion of the electron gas model formulated by Lindhard.[17] Before being used for inter– and extrapolation purposes, however, these theoretical stopping functions were adapted to fit experimental data more accurately (by incorporating more realistic, experimentally obtained effective charges).

Consequently, by plotting experimental He stopping data, scaled experimental H stopping data and using adapted theoretical stopping functions to interpolate where no experimental data was available,
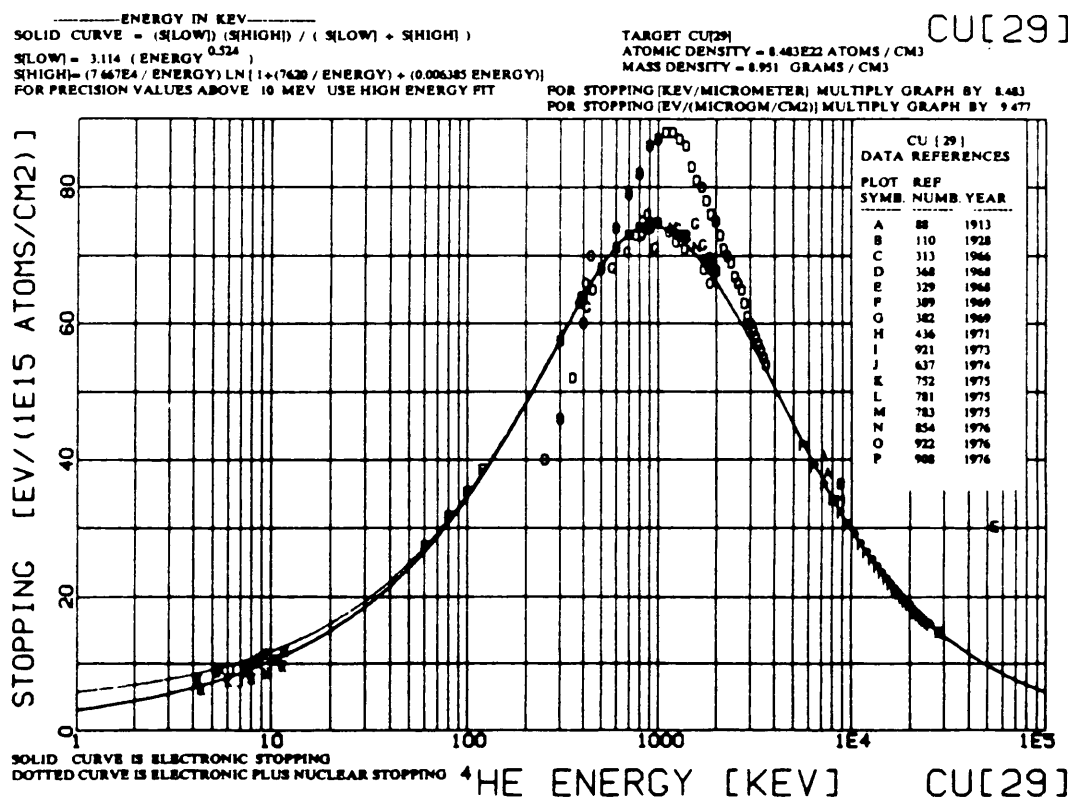
Figure 2.4   (Ref. 17)   A Ziegler He stopping curve

Ziegler was able to formulate the master He stopping curves previously mentioned. A typical example of such a stopping curve of S_e vs energy is illustrated in figure 2.4 for copper.

For a specific energy and target combination the He stopping power can be calculated from the following fitting function:

$$\frac{1}{S_{He}} = \frac{1}{S_{LOW}} + \frac{1}{S_{HIGH}} \qquad \text{2.12a}$$

where $\quad S_{LOW} = A_1 (E)^{A_2} \qquad\qquad$ 2.12b

and $\quad S_{HIGH} = \left(\frac{A_3}{E}\right)\ln \{1 + \frac{A_4}{E} + A_5E\} \qquad$ 2.12c

E is the He energy in keV and $A_1 - A_5$ are the five Ziegler fitting parameters.

When an energy value in keV units is substituted into equations 2.12 the stopping power is given in the form of a stopping cross section in units of 10^{-13} keV cm^2 per atom.

Derivation of the target independent H scaling factor

Ziegler[18b] quotes the following formula (which follows from the perturbation approximation where electronic energy loss is found to be proportional to the square of the charge on the ioncident ion).

$$\frac{S_{HI}(v_1,z_2)}{S_p(v_1,z_2)} = \left(\frac{z^*_{HI}(v)}{z^*_p(v)}\right)^2 \qquad\qquad \text{2.13}$$

where S_{HI} and S_p are the stopping powers for a heavy ion and a proton respectively, and z^*_{HI} and z^*_p are the respective effective charges.

For velocities greater than 200 keV the hydrogen ion can be assumed to be fully stripped, therefore $z_p^*(v) \sim 1$. Equation 2.10 may then be written as

$$\frac{S_{HI}(v_1, v_2)}{S_p(v_1, z_2)} = (z_{HI}^*(v))^2 \qquad \qquad 2.14$$

$$= z_{HI}^2 \cdot \gamma^2$$

where $\gamma = \dfrac{z_{HI}^*(v)}{z_{HI}} = $ the fractional effective charge of the ion. Northcliffe[21] set the Bohr concept of γ (equation 2.4) in the following explicit form:

$$\gamma^2 = 1 - \exp\left[\frac{-v_1}{v_0 z_1^{2/3}}\right] \qquad \qquad 2.15$$

Northcliffe reduced a wide variety of experimental data by dividing each ion/target/energy experimental stopping power by the stopping power of protons in the same target and having the same velocity. Within an accuracy of less than 10% he found equation 2.15 to provide an accurate description of the fractional effective charge to be substituted into equation 2.14. It is therefore safe to say that the ratio of the stopping power of any heavy ion to that of hydrogen is independent of the target material. (Though an *individual* stopping power is definitely not target independent!) Ziegler used equation 2.14 when converting experimental H stopping data to He stopping powers.

4.   COMPUTER SIMULATIONS OF STOPPING AND RANGE

Energy loss and range calculations may be done by considering each

ion/target interaction with a high speed computer. One of the advantages of such a computer simulation is that the ordered structure of a target lattice can be incorporated into the calculations. (The actual effect of lattice structure on energy loss will only be considered in the next chapter.) Generally computer simulations incorporating an "amorphous lattice" (random crystal ordering) predict range distributions which correspond to the LSS predictions for ranges of ions in amorphous materials.

The Monte Carlo type calculations, which are to be briefly discussed, calculate parameters such as the stopping and range distributions of incoming ions; the effect of the target on each incoming ion is therefore observed. The reverse situation, namely the effect the incident ion has on the target atoms themselves (such as displacements and cascade formation which lead to radiation damage phenomena) is not taken into account. Each new ion injected into the target model "sees" the same undisturbed random or ordered lattice from the beginning to the end of its trajectory. The lattice stays "static" in this sense, even though (in the instance of an ordered structure) the vibrations of atoms around their equilibrium positions (due to temperature effects) may be incorporated into the computer model.

The binary collision model originally used by Robinson and Oen[22] for channeling studies and also used by Barrett[23] and Robinson and Torrens[24] (the MARLOWE programme) will be discussed briefly. These authors took lattice structure into account.

The computer calculation developes thus: A large number of individual ion "histories" are followed in each target. Each history begins with a given energy, position and direction. The particle is assumed to change direction

as a result of nuclear collisions and to move in straight free–flight paths between collisions. The energy is reduced as a result of nuclear and electronic (inelastic) energy losses, and the history is terminated when the energy drops below a prespecified value, or when the particle's position is outside the target.

The MARLOWE programme uses a Thomas Fermi potential to describe the interaction between projectile and target atoms. Barrett used a similar interaction potential whilst Robertson and Oen used the Born–Mayer interaction. (See Chapter 3.) The general analytical approach used by both these sets of authors illustrates well how the computer follows the movement of an ion:

The following two parameters are evaluated at each nuclear encounter, thereby determining the new trajectory after each collision:

I   The centre–of–mass scattering angle θ

$$\theta \;=\; \rho \;-\; 2s \int_R^{\infty} \frac{dr}{r^2 f(r)} \qquad\qquad 2.16$$

II   The time integral τ:

$$\tau \;=\; (R^2 - s^2)^2 \;-\; \int_R^{\infty} \left\{ \frac{1}{f(R)} - \left(1 - \frac{s^2}{r^2}\right)^{-\frac{1}{2}} \right\} dr \qquad\qquad 2.17$$

where   S   =   the impact parameter

R   =   the distance of closest approach

V(r)   =   the interatomic potential

$E_r \;=\; E \cdot \dfrac{m_2}{m_1 + m_2}$

$f(r) \;=\; \left(1 - \dfrac{s^2}{r^2} - \dfrac{V(r)}{E_r}\right)^{\frac{1}{2}}$

Thermal vibrations may be simulated by giving each lattice atom a random displacement with coordinates x, y and z chosen from a Gaussian distribution of the form:

$$P(x) = \left(2\pi u_1^2\right)^{-\frac{1}{2}} e^{-\frac{1}{2}x^2/u_1^2}$$

<div align="right">2.18</div>

where u_1 = the thermal vibration amplitude

$$= \langle x^2 \rangle^{\frac{1}{2}} = \langle y^2 \rangle^{\frac{1}{2}} = \langle z^2 \rangle^{\frac{1}{2}}$$

The value of u_1 may be calculated from the Debye theory of thermal vibrations and is given in Angstrom units by

$$u_1 = 12{,}1 \left[\frac{\frac{\phi(x)}{x} + \frac{1}{4}}{M_2 \theta_D} \right]^{\frac{1}{2}}$$

<div align="right">2.19</div>

where θ_D = the Debye temperature (in kelvin)

T = the crystal temperature (in kelvin)

$x = \dfrac{\theta_D}{T}$

$\phi(x)$ = the Debye function which is tabulated by Appleton and Foti[25]

The value of u_1 generally ranges from 0,05 to 0,1.

The TRIM programme[26,27] which has been used to calculate projected ranges in this study, and has the capability of determining aspects pertaining

to radiation damage such as calculating target displacements, replacement collisions, ionization, phonon production, recoil energies, and number of vacancies formed per incident ion (see Chapter 6), is not a true Monte Carlo calculation in the sense of following an atom through a static lattice. Instead, it assumes a fictitious distribution of collision parameters and free pathlengths in an amorphous solid.

5. RANGE CONCEPTS

Implanted ion range profiles are generally determined experimentally by using techniques which involve the removal of thin sections from the surface of an implanted target, coupled with a measurement of the number of implanted atoms removed or remaining[28].
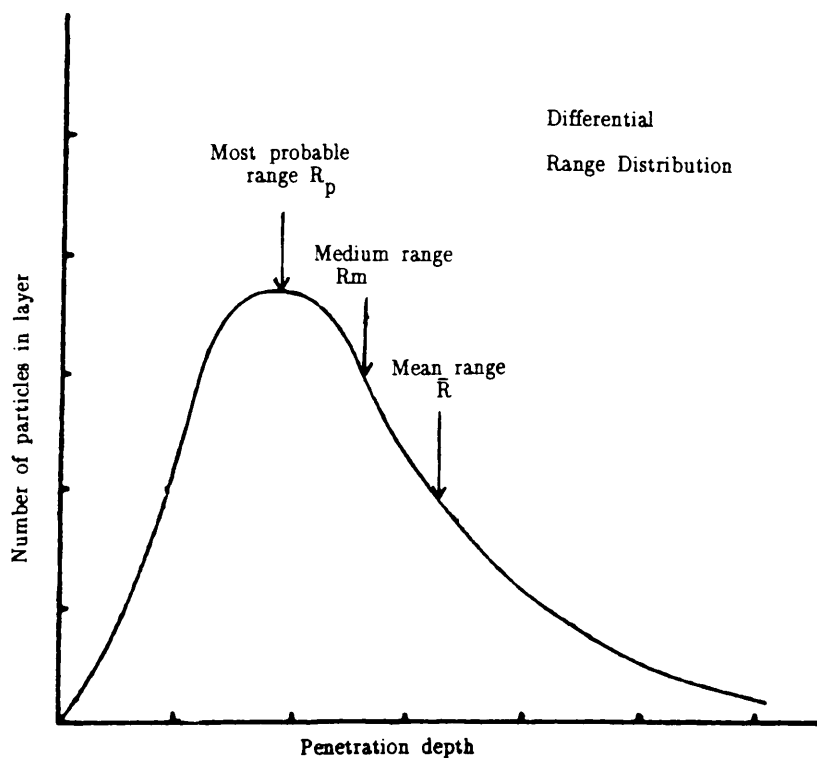
Figure 2.5 (Ref. 29)

The "range distribution" has already been defined as the probability density for finding a particle at rest in a given position inside the target. Since the projectile interacts with a large number of atoms before it comes to rest and the energy transfer in each collision is different, the range and stopping power are both statistical concepts.

Various statistical range parameters as defined by Bergström & Domeij[29] are indicated in figure 2.5. The most probable (or average) range, R_p, is given by the peak of the range distribution, whist the median (or mean) range, $\bar{R}$, is defined as that depth beyond which 50% of all projectiles penetrate further.

It should be remembered that experiments give the range projected on the direction of the incident particle. Only for the case where energy is lost via a large number of small angle scattering incidents, is the projected and true range approximately the same. This approximation is then fairly accurate for electronic stopping (due to reasons discussed earlier).
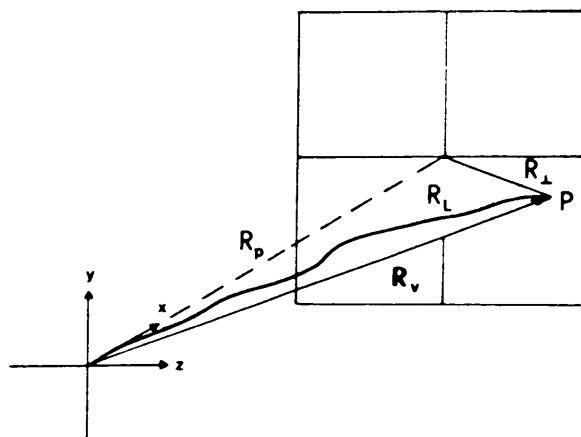
Figure 2.6 (Ref. 32) The various range parameters

Some basic geometrical concepts associated with an energetic particle passing through matter have been summarized by Lehmann[30a] and are illustrated in figure 2.6:

- *the linear (total, effective) range* R_L is the total path length traversed by the particle.

- *the vector range* R_v is the vector between starting point and stopping point.

- *the lateral range* $R_\perp$ is the distance of the stopping point of the particle from a straight line through its starting point along the starting direction. $R_\perp$ is thus a measure of the particle's wandering away from the fictive straight line path corresponding to no interaction. For normal particle incidence one would expect a heavier and slower ion to display a greater amount of this lateral straggling due to larger nuclear deflections.

- *the projected range* R_p is also indicated in figure 2.6. According to this figure the following relationship may be derived:

$$R_v^2 = R_p^2 + R_\perp^2 \qquad\qquad 2.20$$
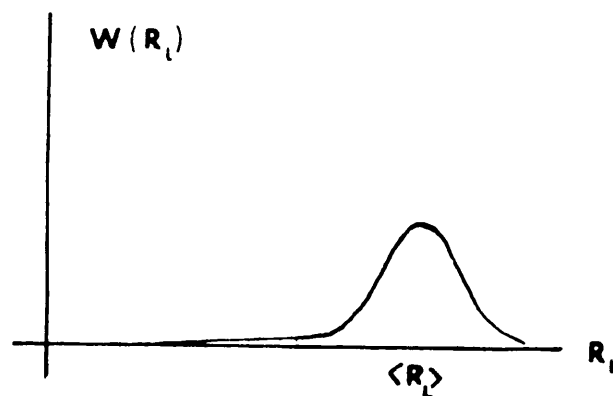
Figure 2.7 (Ref. 30c) The Gaussian range profile

Typical range distributions are often well approximated by a Gaussian[30b]. The normalized distribution $W(R_L)$ for the linear range R_L about the average $<R_L> = \int R_L W(R_L) dR_L$ is illustrated in figure 2.7 and may be formulated as follows:

$$W(R_L) = \{2\pi <\Delta R_L^2>\}^{-\frac{1}{2}} \exp \left\{ - \frac{(R_L - <R_L>)^2}{2<(\Delta R_L)^2>} \right\} \qquad 2.21$$

where $<(\Delta R_L)^2> = <(R_L - <R_L>)^2> = <R_L^2> - <R_L>^2$ is the mean square deviation from the average range $<R_L>$ at a given starting energy E_0.

CHAPTER 3

CHANNELING

1. INTRODUCTION

When an energetic beam of charged particles is incident in a direction parallel to one of the major crystallographic directions in a single crystal, a certain fraction of the particles will undergo small–angle scattering as they pass through the first plane of the crystal. There is a large probability that these deflections will be small enough so that the particles will suffer similar small–angle scatterings at the next atomic plane. This process, when repeated, causes the particles to be steered by successive glancing collisions along an "open passage" in the crystal.

This phenomenon, known as "channeling" is an example of "governed motion" where the regular structure of the crystal is a crucial factor for determining both the path and the properties of the ion trajectory.

The fraction of particles that become channeled depends on the angle which the incident beam makes with a crystallographic axis; and therefore also on the divergence or spread of the beam. Too large an incident angle results in particles approaching the rows of atoms too closely: relatively violent collisions with individual atoms will then occur. Such violent close–encounter individual collisions are contrary to the central concept of channeling which involves a gentle collective steering process due to many small–angle deflections from many target atoms.

A certain critical angle ψ_c therefore exits above which channeling does not occur. Associated with this angle is a "distance of closest possible

approach", ρ_c, as well as a critical maximum value for the transverse component of the beam energy, E_c.

Depending on the angle and degree of collimation of the incident beam, a fraction of the particles (known as the "random fraction") will not undergo channeling at all (due to angles of incidence being too large). Even if the ion beam is directed very accurately towards a channeling axis, the beam will always have a random component along with the channeled fraction. This is due to the fact that even a very well collimated incident beam will be forced to diverge somewhat during its progress through the target. Such beam spreading may be caused by irregular surface layers diverting some of the particles initially incident in a channeling direction, although a high nuclear encounter probability also exists for a perfectly regular surface structure (see section 8). Progressive beam divergence is caused by "delayed dechanneling" whereby each successive steering collision of an initially channeled particle increments the scattering angle slightly, eventually leading to the scattering angle becoming larger than ψ_c, resulting in dechanneling of the particle. Additional interactions due to thermal motion of lattice atoms, as well as due to interactions with electrons, further contribute to the incremental dechanneling of an initially channeled particle.

Some particles with incidence just above the critical angle ψ_c may undergo channeling for one or two oscillations but will then be deflected into a random direction due to their intrinsic instability. These particles are known as "quasi–channeled" particles.

A schematic two–dimensional lattice showing typical trajectories of a channeled (A), random (B) and quasi–channeled (C) particle is illustrated in figure 3.1.
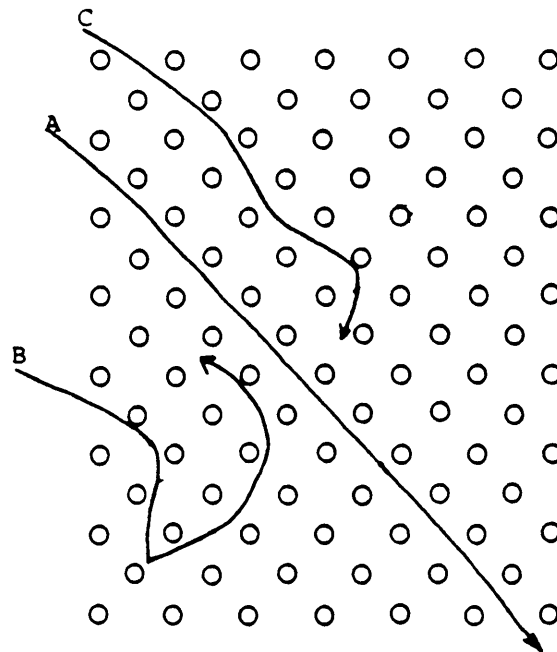
Figure 3.1 (Ref. 94) Channeled (A), random (B) and quasi–channeled (C) particles.

Channeling may occur when the incident beam is parallel to a set of atomic planes (planar channeling). Axial channeling, however, takes place along the intersection of two atomic planes so that the ion is steered down a specific "passage" or "axis" of the crystal. This type of channeling results in the detection of smaller minimum backscattering yields than those obtained for the planar case. The planes and axes responsible for both types of channeling are illustrated in figures 3.2(b) & (c).

The value of using the channeling technique in the study of ion irradiated single crystals, lies in the fact that dechanneling is caused by interstitial ions or at sites where defects, due to irradiation, have distorted the lattice. By collecting backscattering spectra for ions incident in a channeling direction it is possible to study both the range and level of radiation damage. Two important advantages of the channeling technique is that it is non–destructive and data accumulation is rapid.
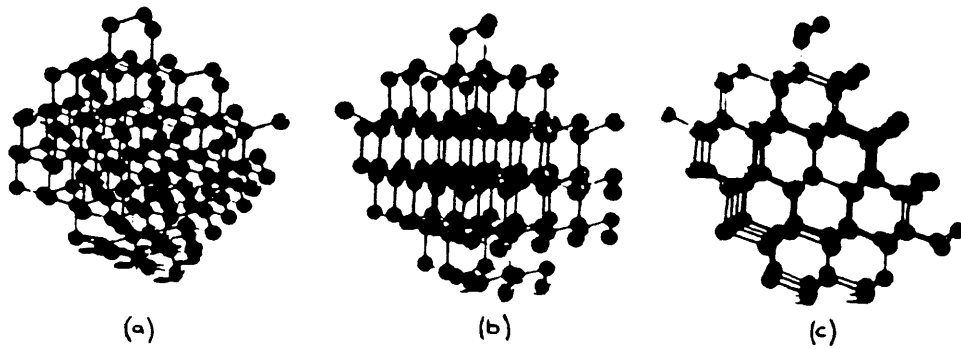
Figure 3.2 (Ref. 71) The atomic configuration of a diamond–type lattice viewed along (a) random, (b) planar and (c) axial directions.

2. A TYPICAL RBS CHANNELING EXPERIMENT

The set–up of a typical channeling experiment using Rutherford backscattering is illustrated in figure 3.3. A single crystal is oriented so that the incident beam makes an angle $\psi > \psi_c$ with a major crystallographic direction. For this orientation a random RBS yield is detected. The sample is then rotated in the direction of decreasing ψ. When the critical angle, ψ_c,
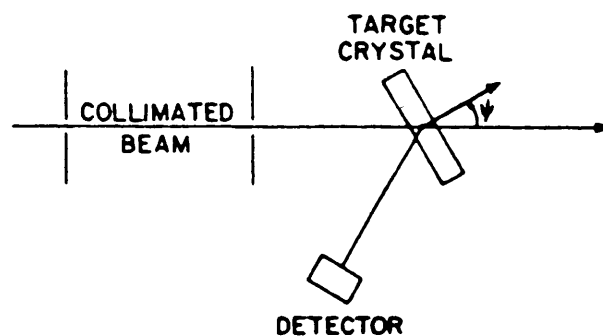
Figure 3.3 (Ref. 34) The set–up of a typical channeling experiment.

is reached the RBS yield at the detector starts decreasing as more and more incident particles are steered into channeling "passages". The minimum RBS yield is obtained when $\psi = 0$. Subsequent increase of ψ past the minimum

yield position, results in increase of backscattered yield until ψ_c is once again reached. (Refer to figure 3.5.)

Figure 3.4 shows a typical backscattering yield versus channel number (or energy or depth) spectrum as displayed on the screen of a multichannel analyser. The "aligned" spectrum is obtained for beam incidence in a maximum channeling direction of an undamaged crystal. This plot is compared to the random spectrum which is collected by holding $\psi > \psi_c$ whilst simultaneously rotating the crystal in a plane normal to the incident beam. It is obvious from figure 3.4 that a significant decrease in backscattering yield is obtained for alignment in a channeling direction.

The "surface peak" observed at the high energy edge of the aligned spectrum is caused by large angle scattering undergone by incident particles in the first few monolayers of the target. These first few surface layers may
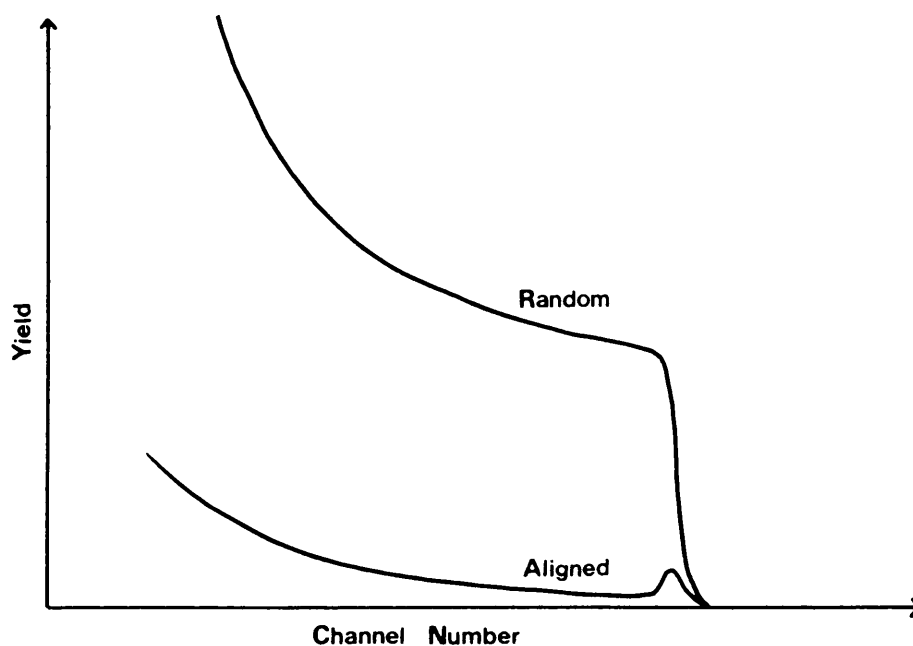
Figure 3.4   MCA spectra obtained for beam incidence in both aligned and random directions

not be as ordered as those deeper within the material due to general surface irregularities and possible oxidation processes. A high nuclear encounter probability also exists for a perfectly ordered surface structure (see section 8).

After the incident particles have penetrated the first few monolayers the RBS yield rapidly diminishes as the ordered lattice structure begins to assert itself and channeling occurs. The yield remains low up to a certain depth in the material, after which increasing electronic and nuclear large angle multiple scattering causes more and more initially channeled particles to become dechanneled resulting in an increasing probability for large angle backscattering and subsequent detection. The depth at which the yield starts increasing and the sharpness of the gradient depends on factors such as crystal temperature and the degree and depth of crystal perfection, as well as on the Miller indices of the axis being used for the channeling experiment.

When the yield from a single channel (corresponding to a depth x just below the surface peak of the aligned spectrum) is measured whilst doing an angular scan through the channeling direction, a plot as illustrated in figure 3.5 is obtained. In this figure the random yield obtained for $\psi > \psi_c$ has been normalized to "1".

$\psi_{\frac{1}{2}}$, defined as that angle which causes a yield halfway between the random and minimum values, can be accurately obtained experimentally and is used in calculating a rough estimate of the critical angle. At an angle just before the critical angle is reached, the yield takes on a value greater than 1, resulting in the formation of the typical "shoulders" on either side of the angular scan. This larger yield is due to the fact that an ion incident at

an angle very close to the critical angle "sees" an atomic density considerably higher than that of the random (average) value of the atomic density. (If the ion beam were scanned over a large enough area the sum of all the "shoulders" and "dips" (as illustrated in figure 3.5) should tend to the average normalized yield value of 1.)
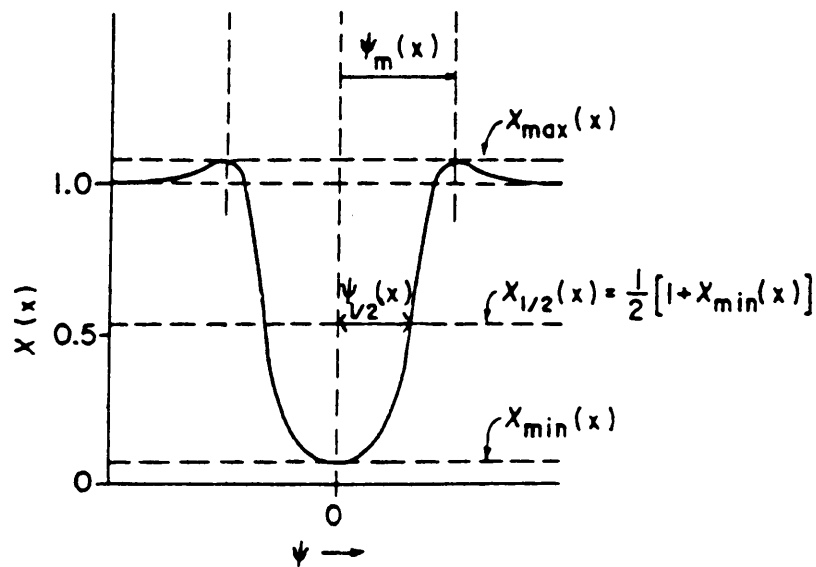
Figure 3.5 (Ref. 35) The normalized dechanneling yield as a function of the incident beam angle.

3. THEORETICAL AND NUMERICAL DESCRIPTIONS OF CHANNELING

Both the "continuum model"[31,32] and Monte Carlo[22,23,33] computer simulations provide adequate descriptions of the channeling phenomenon. Important channeling parameters such as critical angles and minimum yields may be obtained from these descriptions.

The continuum approach assumes each channeled ion may be treated as a localized wave packet to which the laws of classical mechanics may be applied. Bohr[34,35] discussed the conditions under which a classical orbital picture may be used to describe an individual collision between an incident particle and a target atom and found that, for the energy range of interest in channeling studies, and due to the small scattering angles required, classical mechanics cannot adequately describe the collision process. Lindhard[31] however demonstrated that if the channeling process could be described in terms of a series of many collisions (instead of individual interactions) a classical treatment is viable. He showed that the width of the wave packet for a channeled particle remains essentially constant during a set of collisions with a string, and that quantal corrections to the classical description actually decrease with increase in incident particle energy if a continuum approach is used. The theoretical concept of a continuum potential will be discussed after a brief overview of the general interaction potentials existing between projectile and target atoms.

4. INTERACTION POTENTIALS

The interaction potential between an incident ion (of charge $z_1 e$) and an isolated target atom (of charge $z_2 e$) can be adequately described by the stastistical Thomas Fermi model which assumes a Coulombic repulsion potential, $V(r)$, between the two bare nuclei modified by some function of the separation which describes the electronic screening:

$$V(r) = \frac{z_1 z_2 e^2}{r} \psi \left(\frac{r}{a}\right) \qquad 3.1$$

where   r   =   the separation distance between the two particles

         a   =   a screening parameter

         $\psi(\frac{r}{a})$ =   the Thomas Fermi screening function

The screening parameter, a, moderates the effect of the nuclear positive charge on the outer electrons (such a moderation is necessary due to the fact that the inner electrons shield some of the nuclear charge). Firsov[36] used numeral techniques to derive the interatomic potentials of two colliding Thomas Fermi atoms, and after fitting these potentials to equation 3.1 obtained a best fit for:

$$a = 0{,}885 \cdot a_o(z_1^{\frac{1}{2}} + z_2^{\frac{1}{2}})^{-2/3} \qquad \text{3.2}$$

a is called the "Firsov screening parameter" and a_o = 0,528Å (the Bohr radius).

The Thomas Fermi screening function, $\psi(\frac{r}{a})$, which reduces the potential V(r) due to inner electron screening, does not exhibit detailed features such as shell structure, but does approximate the results of Hartree calculations reasonably well (though at large distances it causes V(r) to become too large).

Though an explicit analytic form does not exist for $\psi(\frac{r}{a})$ there are various good analytical approximations:

(i)   The Lindhard approximation:

$$\psi(\frac{r}{a}) = 1 - \frac{r}{(r^2 + c^2a^2)^{\frac{1}{2}}} \qquad \text{3.3}$$

where c is normally set to $\sqrt{3}$

(ii)   **The Molière approximation:**

$$\psi(\tfrac{r}{a}) = 0,1 \, e^{-6r/a} + 0,35 \, e^{-0,3r/a} + 0,55 \, e^{-1,2r/a} \qquad 3.4$$

which has the advantage that at larger distances it tends to fall below the Thomas Fermi result and therefore comes closer to the Hartree value.

(iii) **The Bohr approximation:**

$$\psi(\tfrac{r}{a}) = e^{-r/a_B} \qquad 3.5$$

where $a_B = a_o(z_1^{2/3} + z_2^{2/3})^{-\frac{1}{2}}$ and is called the Bohr screening parameter.

This approximation of the screening function has the disadvantage of providing excessive screening at large distances.

(iv)   **The Born–Mayer approximation:**

$$\psi\left(\frac{r}{a_{BM}}\right) = A_{BM}\left(\frac{r}{a_{BM}}\right) \cdot e^{-r/a_{BM}} \qquad 3.6$$

where A_{BM} and a_{BM} are arbitrary parameters generally fitted to experimental data.

5.   THE CONTINUUM POTENTIAL

To a good approximation the motion of charged incident particles may

be described by a "continuum potential". This potential is obtained by replacing the actual periodic lattice potential, V(r), with a single "smeared out" potential averaged along the rows or planes of atoms steering the channeled projectile.

An assumption of this model is that the energy loss of a channeled particle is ignored. Both longitudinal and transverse components of the projectile energy are assumed to stay constant. Furthermore, the rows of target atoms forming the "smeared out" potential are assumed to be stationary. Thermal vibration effects are therefore ignored.
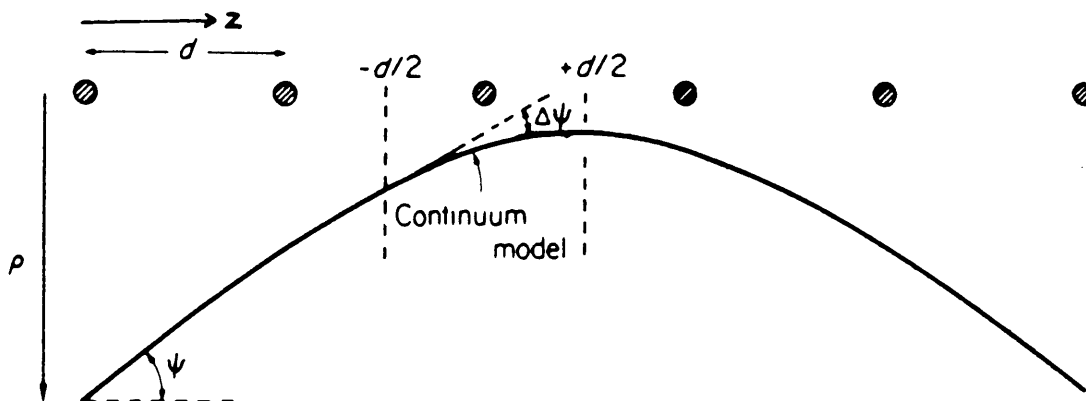
Figure 3.6 (Ref. 95) The channeling trajectory of an ion moving at an initial angle ψ to a row of atoms spaced at regular intervals d.

A continuum potential for axial channeling is derived as follows: Figure 3.6 illustrates an ion moving at an initial angle ψ to a row of atoms spaced at regular intervals d. The row is situated along the z–axis and the incoming ion is travelling on a plane containing the row. $\rho(z)$ is the shortest distance of the ion from the atomic string. The average interatomic potential

(or "continuum potential") experienced by an ion at $\rho(z)$ is then given by:

$$V_{RS}(\rho) \;=\; \frac{1}{d} \int_{-\infty}^{+\infty} dz \; V\left(\sqrt{z^2 + \rho^2}\right) \qquad\qquad 3.7$$

R indicates that the potential is due to a row of atoms while S symbolizes the static situation.   V is the interatomic potential between an ion–target pair.

Substitution of the Lindhard potential (using the Lindhard screening function of equation 3.3) into equation 3.7 yields

$$V_{RS}(\rho) \;=\; \frac{2z_1 z_2 e^2}{d} \; f_{RS}\!\left(\tfrac{\rho}{a}\right) \qquad\qquad 3.8$$

where

$$f_{RS}\!\left(\tfrac{\rho}{a}\right) \;=\; \tfrac{1}{2} \ln\left\{ \left(\tfrac{Ca}{\rho}\right)^2 + 1 \right\} \qquad\qquad 3.9$$

Equation 3.8 is called the Lindhard standard potential. (Molière, Bohr and Born–Mayer potentials may also be substituted into equation 3.7 yielding different functional forms of $f_{RS}\!\left(\tfrac{\rho}{a}\right)$.)

The "characteristic axial channeling angle" is defined by Lindhard to be

$$\psi_1 \;=\; \left(\frac{2z_1 z_2 e^2}{Ed}\right)^{\frac{1}{2}} \qquad\qquad 3.10$$

where E is the energy of the incident particle. When this expression is substituted into equation 3.9 one obtains:

$$V_{RS}(\rho) \quad = \quad \psi_1^2 E \ f_{RS}(\tfrac{\rho}{a}) \qquad\qquad 3.11$$

A similar expression containing a characteristic planar channeling angle may be derived for the planar case.

Equation 3.11 describes the continuum potential experienced by an axially channeled particle due to a single row of atoms. When the whole three–dimensional structure of the crystal is taken into account the total potential field in which the particle moves may be obtained by summing over all the potentials due to all the rows:

$$U_{RS}(\rho) \quad = \quad \sum_i V_{RS}(\rho_i) - U_{min} \qquad\qquad 3.12$$

where $U_{RS}(\rho)$ = the net continuum potential exerted on an axially channeled particle

  $V_{RS}(\rho_i)$ = the continuum potential exerted on the particle by the i–th atomic row

  U_{min} = a constant substracted in order to make the minimum value of $U_{RS}(\rho)$ equal to zero

A similar expression may be obtained for the planar situation.

The net continuum potential for alpha particles in the {001} transverse plane in copper[37] is illustrated in figure 3.7. The black circles indicate lattice atom positions. As may be expected, the total interaction potential reaches a minimum at the centre of the channeling passage.
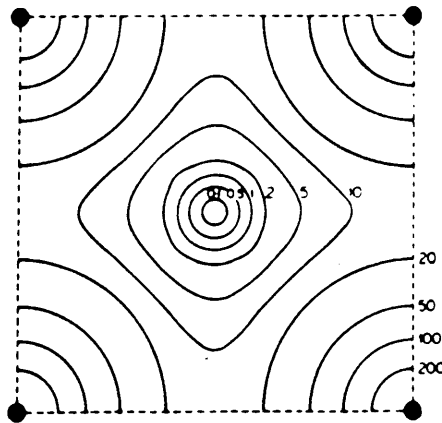
Figure 3.7 (Ref. 37) The net continuum potential for alpha particles in the {001} transverse plane in copper.

6. CRITICAL ANGLES

For axial channeling Lindhard calculated two expressions for the critical angle depending on the energy of the incoming ion:

$$\psi_c \simeq \psi_1 = \left\{\frac{2z_1z_2e^2}{Ed}\right\}^{\frac{1}{2}} \qquad \text{3.13}$$

$$\text{for } E > E'$$

where d = the distance between atoms along the $<hkl>$ direction in question and

$$\psi_c \simeq \psi_2 = 1,5^{\frac{1}{4}} \cdot \left(\frac{a}{d} \psi_1\right)^{\frac{1}{2}} \qquad \text{3.14}$$

$$\text{for } E < E'$$

where $E' = \dfrac{2z_1z_2e^2d}{a^2E}$ and a = the screening parameter

Expression 3.13 applies for conditions in which the screening is relatively unimportant and the interaction is essentially Coulomb in nature.

Equation 3.14 applies for conditions under which the exact nature of the

screening is important. For the 1–2 MeV alpha particles and the 150 keV Ar ions used in the various metals of this study $E > E'$ and equation 3.13 applies.

ψ_1 and ψ_2 are essentially theoretical parameters. $\psi_{\frac{1}{2}}$, defined earlier, is however an experimentally measurable quantity. For the high energy limit ($E > E'$) Lindhard suggested the following linear relationship between $\psi_{\frac{1}{2}}$ and ψ_1:

$$\psi_{\frac{1}{2}} = c\psi_1 \qquad \qquad 3.15$$

where c is a constant ranging between the values 1 and 2.

So far only static lattices have been discussed. If thermal vibrations are taken into account one would expect both the continuum potential and the critical distance of closest approach (and therefore also the critical and half angles) to be affected.

For MeV light ions Appleton and Foti[25] provide the following temperature–dependent expression for $\psi_{\frac{1}{2}}$:

$$\psi_{\frac{1}{2}} = 0{,}8 \ F_{RS}(\xi)\psi_1 \qquad \qquad 3.16$$

where $\quad \psi_1 = 0{,}307 \left(\dfrac{z_1 z_2}{Ed}\right)^{\frac{1}{2}}$ (in degrees)

$\qquad \quad$ d $\;=\;$ atomic spacing along axial direction

$\qquad \quad$ E $\;=\;$ incident energy in MeV

$\qquad \quad \xi \;=\; 1{,}2 \ \dfrac{u_1}{a}$ where $u_1 =$ the thermal vibration amplitude

$\qquad \quad F_{RS} \;=\;$ the square root of the adimensional string potential

Equation 3.16 predicts the value of $\psi_{\frac{1}{2}}$ to decrease with increase in ambient crystal temperature. This is to be expected due to the increased thermal lattice vibrations effectively reducing the cross sectional area of a channel.

7. MINIMUM YIELDS

A minimum backscattering yield is obtained when the angle between the incident beam and the channeling axis is zero. The continuum model predicts for axial channeling:

$$\chi_{min} = Nd\ \pi\rho_c^2 \qquad\qquad 3.17$$

where

χ_{min} = minimum rbs yield

N = the atomic density of the target

d = the spacing between atoms in the axial rows

ρ_c = the minimum approach distance for channeling to still occur

Due to the increase in thermal vibration of host atoms around their lattice sites with increase in ambient temperature, one would expect an increasing amount of initially channeled particles to become dechanneled with increase in temperature. Lindhard suggested the following temperature dependent expression for the minimum axial channeling yield: (this expression applies for $E > E'$)

$$\chi_{min} = Nd\pi(u_2^2 + a^2) + \chi_3 \qquad\qquad 3.18$$

where $u_2 = \langle x^2 + y^2\rangle^{\frac{1}{2}} \sim 2^{\frac{1}{2}}u_1$

and χ_3 is a contribution from the divergence produced in the beam by scattering in any amorphous region of the surface of the specimen.

Barrett[23] obtained values of the minimum yield using Monte Carlo calculations of 3 MeV protons along the <111> direction in W at various temperatures. He found the yield to increase with increasing temperature as may be expected from equation 3.18 but found a more suitable approximation for his results to be:

$$\chi_{min} \simeq Nd\pi\ c(\Delta)u_2^2 \qquad\qquad 3.19$$

where $c(\Delta)$ is dependent on the beam divergence Δ.
For $\Delta = 0$, $c(\Delta) \sim 3$.

Appleton and Foti[25] give the following expression for the minimum channeling yield:

$$\chi_{min} = Nd\pi(2u_1^2 + a^2) \qquad\qquad 3.20$$

A more accurate expression was obtained by an empirical fit to computer calculations:

$$\chi_{min} = 18,8\ Ndu_1^2(1 + \xi^{-2})^{\frac{1}{2}} \qquad\qquad 3.21$$

For energies of interest to this study $\xi = \dfrac{126u_1}{\psi_{\frac{1}{2}}d}$ ($\psi_{\frac{1}{2}}$ given in degrees).

8. OSCILLATIONS IN NUCLEAR ENCOUNTER PROBABILITY

An aspect of channeling which has not yet been considered is the large variation in nuclear encounter probability for an ion traversing the surface of a target material. An expression for the nuclear encounter probability, P, is given by Barrett[23] and was used in his computer simulations to obtain the plot of P versus penetration depth as illustrated in figure 3.8. This plot was obtained for planar channeling. The nuclear encounter probability is very high right at the surface of the material due to the random striking of incident ions. This is because of two factors: (a) Even if the ion beam is directed exactly along the crystal axis, a high probability exists for the ions to interact with the surface atoms due to the fact that they have not yet been "steered" into the "channels". (b) Relaxation of the first few surface layers also contributes to dechanneling of ions right at the surface. A large P causes an increase in the occurrence of backscattering collisions, resulting in the formation of the surface peak present in a typical RBS spectrum.
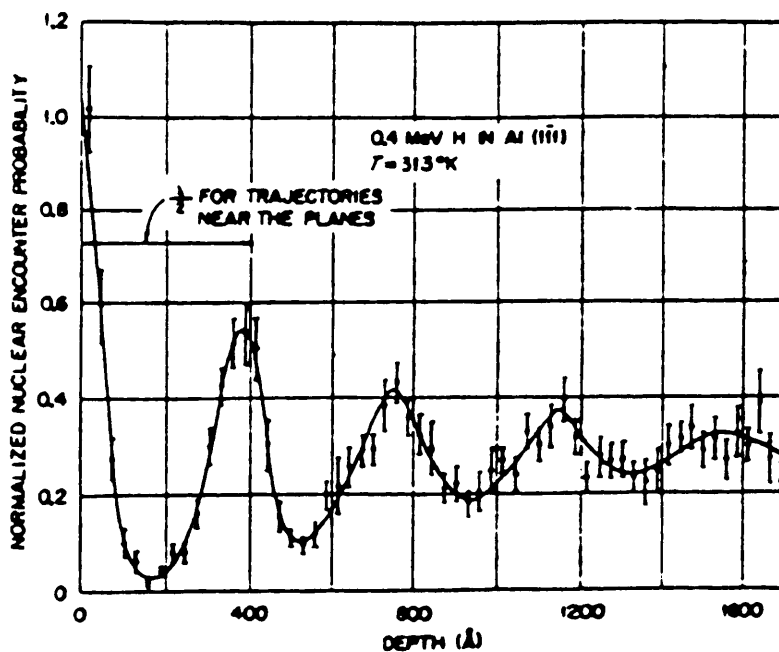
Figure 3.8 (Ref. 23) Oscillations in nuclear encounter probability.

A bit further into the material incident ions become channeled, and as they progress into the middle of a channel, P reaches the first minimum shown in figure 3.8. Ions proceeding further are deflected towards the wall of the channel, their closest approach distance corresponding with the second maximum shown in figure 3.8. Deflection back into the mid–channel region corresponds with the next minimum value of P, and thus the oscillation proceeds.

This variation in P tends to be dampened with increasing depth as the ion trajectories grow out of phase due to factors such as basic variations in wavelength causing a wide range of transverse energies to be associated with the different ions.

A similar dampened oscillation as the one shown in figure 3.8 for planar channeling, may be obtained for the axial situation. In this case, however, P would in general be much smaller. The general behaviour of the oscillation is more irregular due to the irregular way in which a trajectory moves from row to row in two dimensions rather than from plane to plane in one.

Statistical equilibrium is only reached at depths in the order of 1000 Å. It is therefore evident that minimum yields must be measured at depths well below the surface of the material to avoid these surface oscillations. Alternatively yields can be averaged over a depth interval which is large compared to the generally regular wavelength of the oscillations.

9. THE STOPPING AND RANGE DISTRIBUTION OF CHANNELED IONS

Besides using the channeling phenomenon as an analytical tool for the

study of damage ranges (using 1–2 MeV He ions) it is also necessary to investigate the role (if any) which channeling plays in the actual formation of the deep radiation damage incurred by metals implanted with heavy ions in the 100 keV energy range. The stopping of channeled ions must therefore be investigated for two different instances:

1. Stopping of 150 keV heavy (e.g. Ar) ions
2. Stopping of 1–2 MeV light (e.g. He) ions

One would expect a channeled ion, steered down a specific crystal axis by a series of glancing collisions, to generally experience less slowing down due to two factors:

1. The ion does not undergo close nuclear encounters (only large impact parameter gentle steering collisions).
2. The ion spends a large amount of its time in the mid–channel region where electron density is lower than in regions close to atomic nuclei.

Due to the first factor one might expect (except for very low energy ions) nuclear stopping of a channeled ion to be virtually non–existent. However, because even the amorphous stopping powers for ions in the energy ranges employed in this study have very small nuclear components associated with them, one would not expect the reduced nuclear stopping due to channeling to affect the overall LSS stopping power value significantly.

Eriksson[38] proved by a detailed study of the energy dependence of maximum channeling ranges in tungsten that electronic stopping is the only

significant mechanism of energy loss for a well–channeled ion. One would however also expect electronic stopping to be reduced in a channeling direction due to the lower electron densities encountered by the ion.

Due to the different degrees of openness associated with different <hkl> directions one would expect stopping powers to vary for beam incidence in various crystallographic directions. Even the stopping power for one specific <hkl> direction could be expected to vary depending on the angle of incidence of the channeled beam. A larger incident angle causes a closer approach of the incident particles to the wall of the channel (as they oscillate along the axis) thereby causing the stopping power to be larger than in the case of a smaller angle of incidence. Energy straggling is therefore enhanced in a channeling direction due to factors such as beam divergence.

The difference in the behaviour of ions implanted into amorphous material as opposed to various low index crystal directions is illustrated in figure 3.9 which shows the experimental range profiles of 40 keV radioactive ^{125}Xe implanted into bcc tungsten as obtained by Davies and Jespersgard[39]. (These profiles were obtained by measuring the remaining activity after successive layer removal.) Similar results have been obtained for the fcc metals nickel[40], copper and gold[41].

The LSS projected range for Xe in the bcc metal tungsten is about 70Å which corresponds to the amorphous curve in figure 3.9. For implantations in various crystal directions the curves illustrated in figure 3.9 may be subdivided into three regions:

(i) a rapid initial decrease in ion concentration with depth; roughly

80% of all the injected ions become scattered from the aligned direction whilst traversing the surface region of the crystal, and hence penetrate only to about the "amorphous" range.
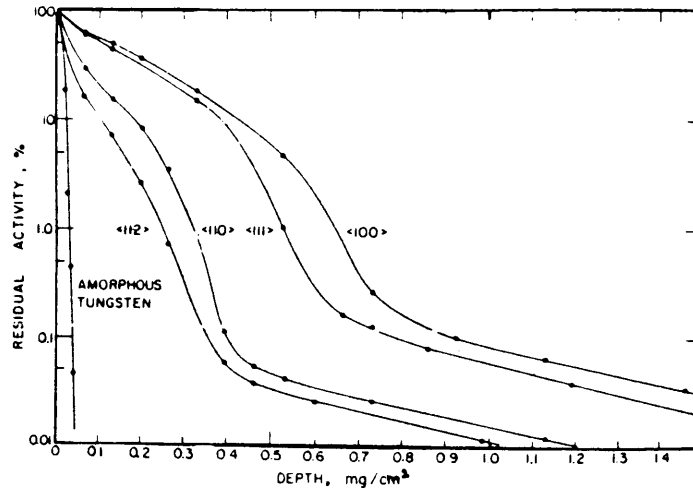
Figure 3.9 (*Ref. 39*) *Ranges of Xe ions channeled along various <hkl> directions in tungsten.*

(ii)   an intermediate (approximately exponential) region exists due to initially channeled particles undergoing large angle scattering. From figure 3.9 it can be seen that about 20% of the Xe ions penetrate from 2–8 times deeper than the LSS range (depending on the <hkl> direction involved) while about 10% penetrate 5–13 times deeper. (For the <100> and <111> directions about 40% to 50% penetrate 2–3 times deeper).

(iii)   Davies et al.[41] defined R_{max} as the deepest region to which very well channeled particles can penetrate. A sudden bendover towards this maximum range is observed in this example of bcc tungsten for about 1% of the incident particles. Depending on the <hkl> indices involved it may be seen in figure 3.9 that such perfectly channeled particles can reach depths of up to 50 times the LSS predicted

range. (For fcc metals Whitton[41] did not observe such a sudden cut–off at R_{max} as was found for bcc tungsten.)

Beyond R_{max} about 0,1% of the ions exhibit the "supertail", a pheno–menon whereby ions penetrate hundreds of times deeper than the LSS range. It has been established that this supertail is not an enhanced penetration or channeling effect[39] but rather that it is caused by a rapid interstitial diffusion process after perfectly channeled particles have lost their kinetic energy. This effect was only observed in bcc tungsten and not in the fcc crystals Al, Cu and Au.[41]

To summarize: It is obvious that stopping powers decrease and ranges increase in channeling directions. These parameters vary for different target/projectile/energy/<hkl> combinations.

Channeled stopping powers for 1–2 MeV Helium

Gibson[43] found the minimum channeled energy loss measured for 800 keV He ions in gold to be about 60% of the random (amorphous) energy loss. Eisen et al.[43] found the ratio between channeled and random stopping powers for He ions channeled in the <111> direction of Si, to reach a maximum of well above 50% (up to 90%!) in the medium energy region. (The LSS and especially the Bethe–Bloch stopping regions generally were found to correspond to about a 50% reduction.) One might therefore expect the energy loss of the medium energy 1–2 MeV alpha particles used in this study not to be very greatly influenced by channeling. The precise amount of reduction in He stopping powers along channeling directions is however not known and no adjustments were made to amorphous stopping powers when analyzing alpha particles incident in channeling directions.

The amount of error induced by such an approach (which results in an under–estimation of depth) may be minimized by setting up the experiment in such a way that the total path travelled by a detected particle consists of as small a channeled section as possible. This may be achieved by using a single–alignment backscattering technique (so that all detected backscattered particles travel back to the incident surface in non–channeling directions).

The channeling of heavy ions in the 100 keV range is discussed further in Chapter 6.

CHAPTER 4

DEFECTS OCCURING IN FCC AND BCC LATTICE STRUCTURES

1. DISCUSSION OF FCC AND BCC LATTICE STRUCTURES

The two types of cubic lattices of interest to this study are the body–centred cubic (bcc) and face–centred cubic (fcc) structures. The conventional unit cubes for both the fcc and bcc lattices are shown in figure 4.1. Super–imposed on each of these is found the rhombohedral form of the primitive unit cell associated with each structure.

(a)   (b)
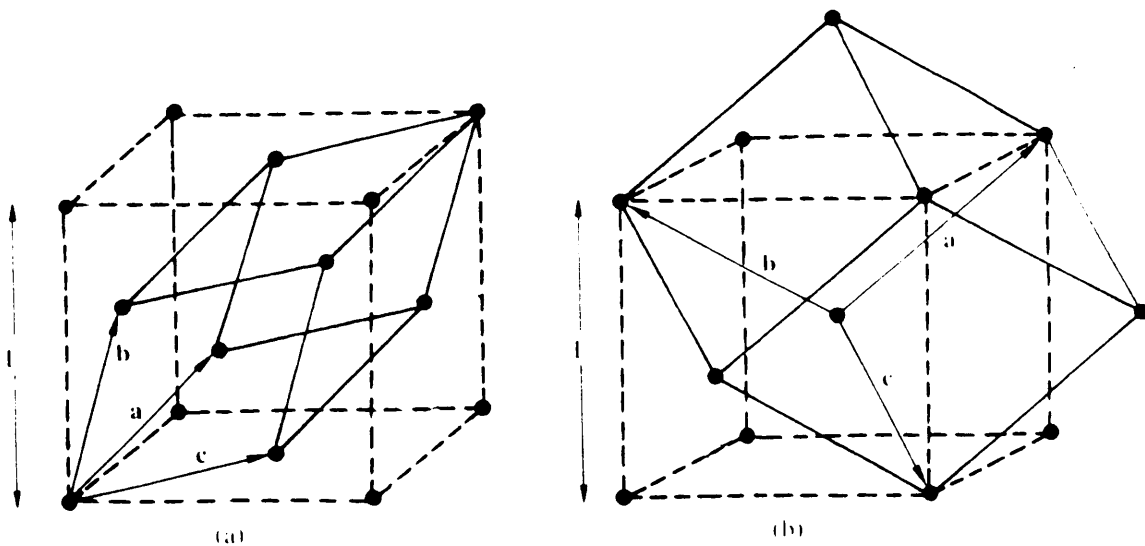
Figure 4.1   (Ref. 96)   Conventional unit cubes for (a) the fcc and (b) the bcc lattices.

Both unit cubes have lattice parameter a. In terms of a, the nearest neighbour distance (length of primitive cell vectors $\bar{a}$, $\bar{b}$ and $\bar{c}$) for the fcc structure is $a/\sqrt{2}$ and $\sqrt{3}\,a/2$ for the bcc structure. Ni (a = 3,52 Å),

Cu (a = 3,61 Å) and Pt (a = 3.92 Å) all occur in the fcc form, whilst the α–Fe (a = 2,87 Å) used in this study exists in the bcc form.

Fcc crystals are more densely packed than bcc crystals due to all the atoms being close–packed in an ABCABC stacking sequence. The conventional unit cube for a fcc crystal is 74% full as opposed to the 68% for the bcc unit cube where the ABABAB packing is not as close as in the fcc instance.

Ion beams travelling in directions in which the crystal is relatively "open" generally exhibit good channeling. Planes perpendicular to good channeling directions are, for both the fcc and bcc structures, the low index {111}, {110}, {100} and {211} surfaces. Specific examples of these planes are illustrated in figures 4.2 a,b,c and d. The arrangement of atoms on these four types of plane are shown for both the fcc $\left(\text{figure } 4.3(a)\right)$ and bcc $\left(\text{figure } 4.3(b)\right)$ structures. Also indicated in these figures are the results of planar atomic density calculations.

Robinson and Oen[22] define the "transparency" (ρ_{hkl}) of a crystallographic plane to be the number of <hkl> row lines passing through a unit area of an {hkl} plane. They list the transparency values for fcc copper (in Å^{-2} units) as well as for a fictional bcc copper. Taking lattice parameters into account the transparencies of Ni, Fe and Pt could be calculated from the copper data. The results are listed in Table 4.2.

For fcc crystals: $\rho_{(110)} < \rho_{(100)} < \rho_{(211)} < \rho_{(111)}$

For bcc crystals: $\rho_{(111)} < \rho_{(100)} < \rho_{(110)} < \rho_{(211)}$

TABLE 4.1

Element	Atomic Number z	Atomic Mass M	bcc or fcc	Lattice parameter a (Å)	Mass density g cm^{-3}	Atomic density atoms cm^{-3} × 10^{22}	Melting point (°C)	Thomas Fermi radius (Å)
α–Fe	26	55,847	bcc	2,867	7,87	8,50	1535	0,1056
Ni	28	58,71	fcc	3,524	8,91	9,126	1453	0,1042
Cu	29	63,546	fcc	3,615	8,93	8,45	1083,4	0,1035
Pt	78	195,09	fcc	3,923	21,47	6,62	1772	0,0844

Figure 4.2(a)   The {100} plane
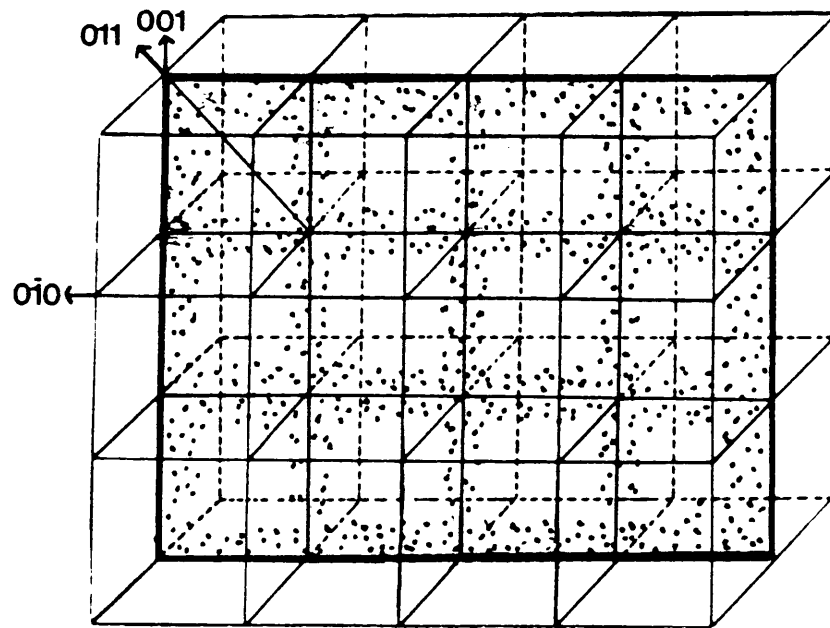
Figure 4.2(b)   The {110} plane
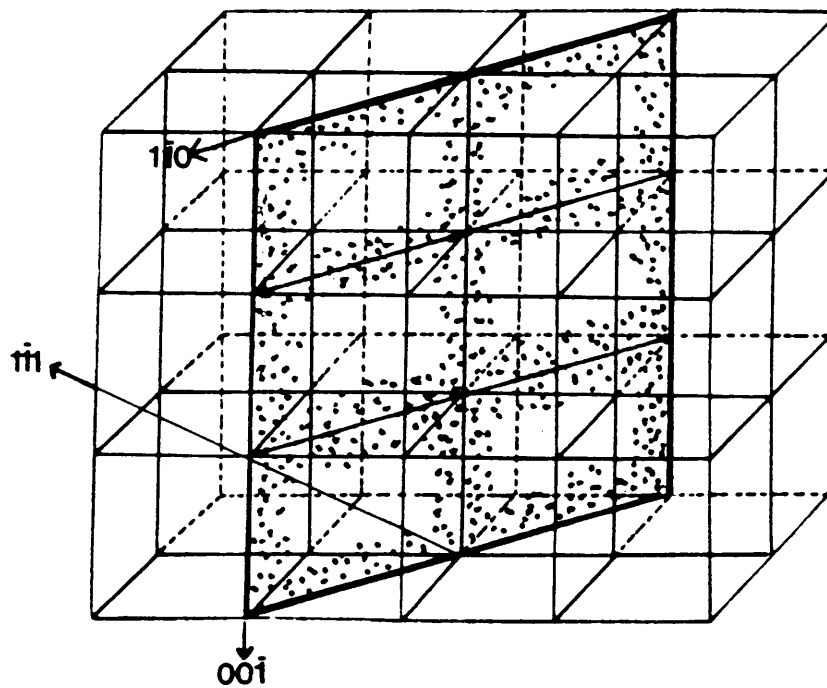
Figure 4.2 (c)   The $\{111\}$ plane

$0\bar{1}1$

$1\bar{2}1$
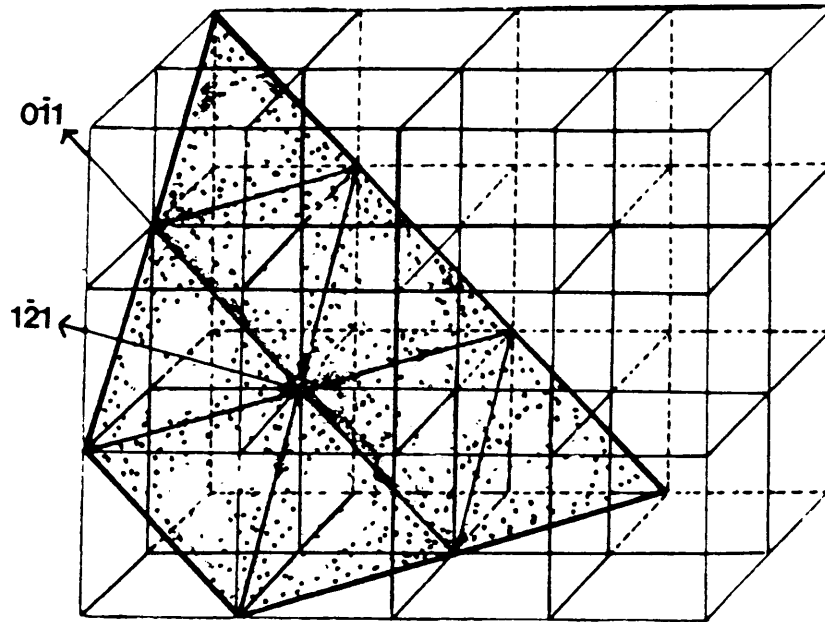
Figure 4.2 (d)   The $\{211\}$ plane

$0\bar{1}1$

$1\bar{2}0$

$1\bar{1}\bar{1}$
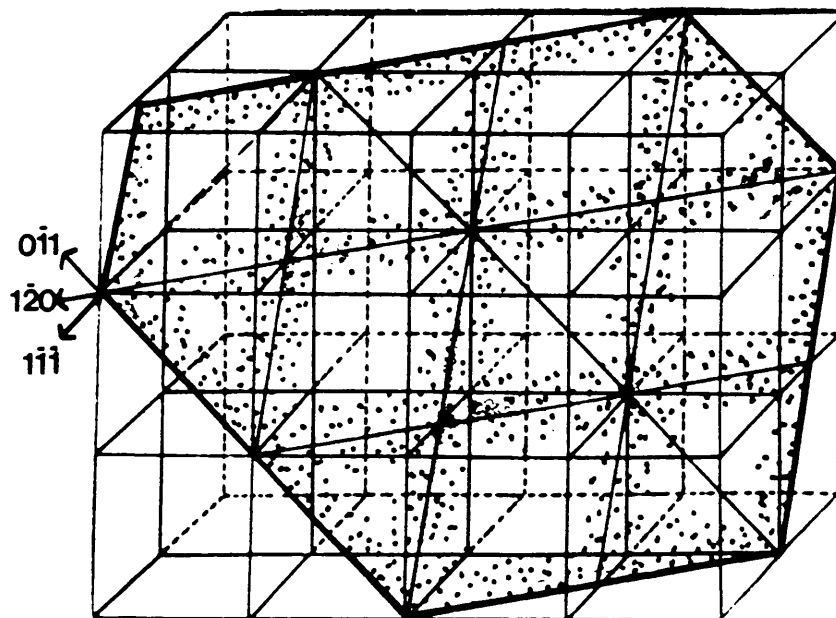
Figure 4.3(a) FCC Surfaces
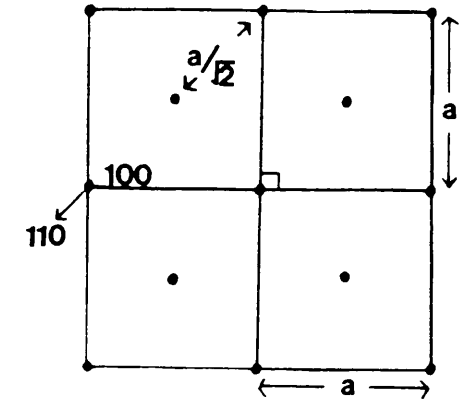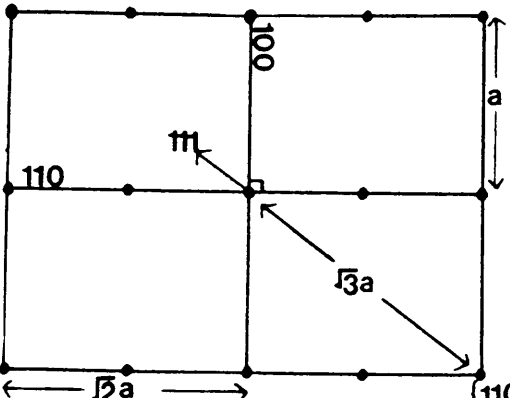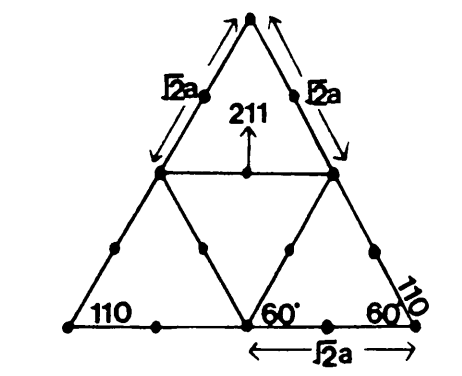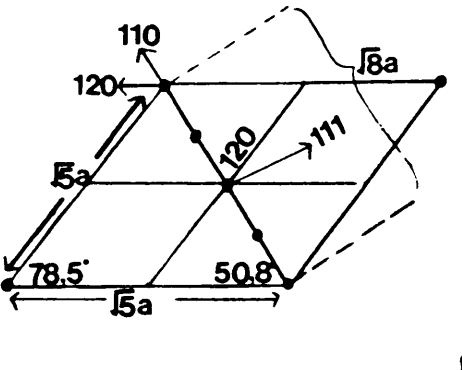
	Surface atomic density (atoms Å^{-2})	Atomic spacings along each row (Å)
{100}	$\ell_A = \dfrac{4\left(\frac{1}{4}\right)+1}{a^2}$ $= \dfrac{2}{a^2}$ $\longrightarrow$	$\langle 100 \rangle : 1a$ $\langle 110 \rangle : \dfrac{a}{\sqrt{2}}$ $= 0{,}71a$ $\longrightarrow$
{110}	$\ell_A = \dfrac{4\left(\frac{1}{4}\right)+2\left(\frac{1}{2}\right)}{\sqrt{2}\,a \cdot a}$ $= \dfrac{2}{\sqrt{2}\,a^2}$ $= \dfrac{1{,}41}{a^2}$ $\longrightarrow$	$\langle 111 \rangle : \sqrt{3}\,a$ $= 1{,}73a$ $\longrightarrow$
{111}	$\ell_A = \dfrac{3\left(\frac{1}{6}\right)+3\left(\frac{1}{2}\right)}{\frac{1}{2}\left(\sqrt{2}\,a\right)^2 \sin 60°}$ $= \dfrac{2{,}31}{a^2}$ $\longrightarrow$	$\langle 211 \rangle : \sqrt{2}\,a \sin 60°$ $= 1{,}22a$ $\longrightarrow$
{211}	$\ell_A = \dfrac{3+4\left(\frac{1}{4}\right)}{\left(\sqrt{5}\,a\right)^2 \sin 78{,}5°}$ $= \dfrac{0{,}82}{a^2}$ $\longrightarrow$	

Figure 4.3(b) BCC Surfaces
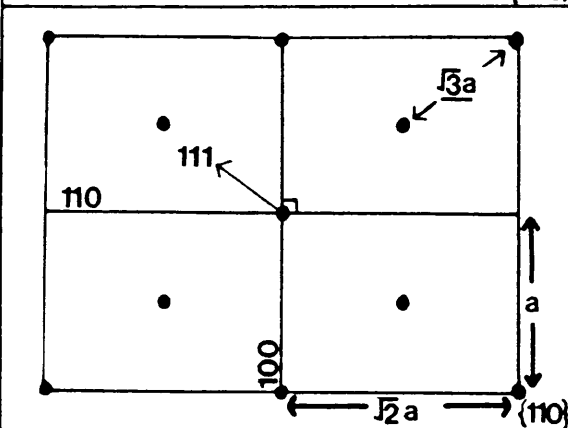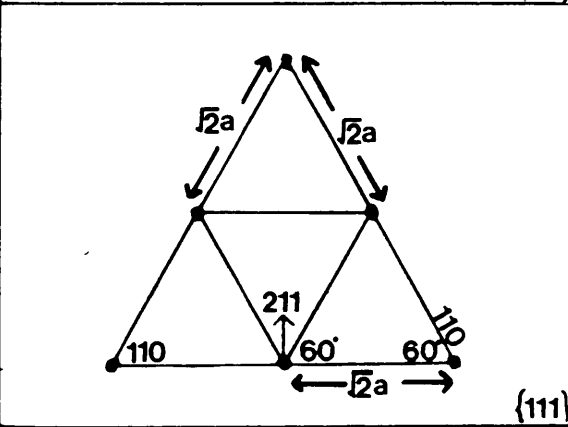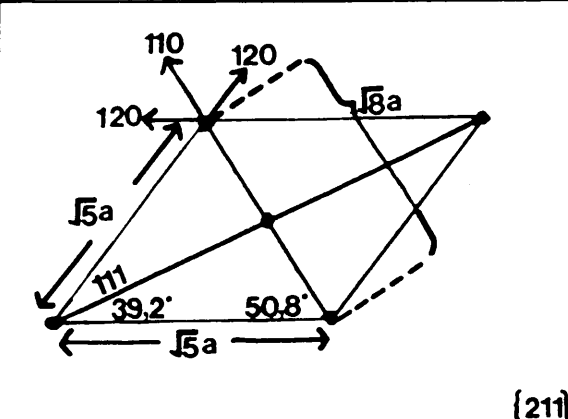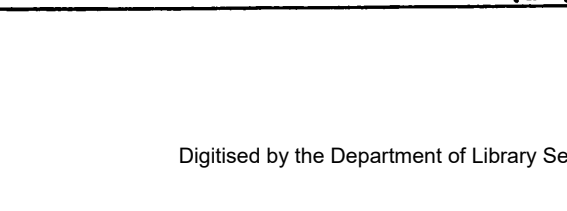
	Surface atomic density (atoms $\mathring{A}^{-2}$)	Atomic spacings along each row ($\mathring{A}$)
(100)	$\ell_A = \dfrac{4\left(\frac{1}{4}\right)}{a^2}$ $= \dfrac{1}{a^2}$	$\langle 100 \rangle : 1a$ $\langle 110 \rangle : \sqrt{2}\,a$ $= 1,41a$
(110)	$\ell_A = \dfrac{4\left(\frac{1}{4}\right)+1}{\sqrt{2}\,a \cdot a}$ $= \dfrac{1,41}{a^2}$	$\langle 111 \rangle : \dfrac{\sqrt{3}\,a}{2}$ $= 0,87a$
(111)	$\ell_A = \dfrac{3\left(\frac{1}{6}\right)}{\frac{1}{2}\left(\sqrt{2}\,a\right)^2 \sin 60°}$ $= \dfrac{0,588}{a^2}$	$\langle 211 \rangle : 2\cdot\sqrt{2}\,a \sin 60°$ $= 2,45a$
(211)	$\ell_A = \dfrac{4\left(\frac{1}{4}\right)+3}{\left(\sqrt{5}\,a\right)^2 \sin 78,5°}$ $= \dfrac{0,82}{a^2}$	

TABLE 4.2

Transparencies* ($\mathrm{\AA}^{-2}$) of various metals in various <hkl> directions (*the number of <hkl> row lines passing through a unit (hkl) plane).

<hkl> direction	Fe (bcc)	Ni (fcc)	Cu (fcc)	Pt (fcc)
<110>	0,512	0,228	0,217	0,184
<100>	0,364	0,322	0,306	0,260
<211>	0,889	0,395	0,375	0,318
<013>	–	0,512	0,487	0,413
<111>	0,314	0,558	0,530	0,450

The order of these results corresponds well to Robertson and Oen's calculated ranges of ions channeled in these four directions. By using a Monte Carlo computer programme they calculated the order of the ranges to be:

For fcc crystals: <110> > <100> > <211> > <111>

For bcc crystals: <111> > <100> > <110> > <211>

The smaller the calculated transparency value, therefore, the greater the penetration of an ion channeled in the specific <hkl> direction. It may be noticed that the areal atomic densities indicated in figures 4.3(a) and (b) do not correspond exactly with the order of transparencies and ranges found by Robertson and Oen. The planar atomic density may not be used as an accurate indication of the degree of "openness" due to the fact that atoms directly beneath a low areal density plane might block the passage normal to this plane.

It is interesting to note the spacing, d, of atoms along the $<hkl>$ row perpendicular to each $\{hkl\}$ plane. (These values are also indicated in figures 4.3(a) and (b) as well as being listed in Table 4.3.)

For fcc: $d_{<110>} < d_{<100>} < d_{<211>} < d_{<111>}$

For bcc: $d_{<111>} < d_{<100>} < d_{<110>} < d_{<211>}$

TABLE 4.3

Distances between atoms in various $<hkl>$ directions

$<hkl>$	fcc $(\times a(\text{Å}))$		bcc $(\times a(\text{Å}))$	
100	1	$\simeq 1,00$	1	$\simeq 1,00$
110	$1/\sqrt{2}$	0,71	$\sqrt{2}$	1,41
111	$\sqrt{3}$	1,73	$\sqrt{3}/2$	0,87
210	$\sqrt{5}$	2,24	$\sqrt{5}$	2,24
211	$\sqrt{6}/2$	1,22	$\sqrt{6}$	2,45
221	3	3,00	3	3,00
310	$\sqrt{10}/2$	1,58	$\sqrt{10}$	3,16
320	$\sqrt{13}$	3,61	$\sqrt{13}$	3,61
321	$\sqrt{14}/2$	1,87	$\sqrt{14}$	3,74
322	$\sqrt{17}$	4,12	$\sqrt{17}$	4,12
331	$\sqrt{19}$	4,36	$\sqrt{19}/2$	2,18
332	$\sqrt{22}/2$	2,35	$\sqrt{22}$	4,69
310	$\sqrt{11}$	3,32	$\sqrt{11}/2$	1,66
410	$\sqrt{17}$	4,12	$\sqrt{13}$	4,12
411	$\sqrt{18}/2$	2,12	$\sqrt{18}$	4,24

These sequences correspond once again to the order of ranges mentioned earlier. The more dense the atomic spacing of a row the better it is therefore able to keep a particle channeled (the more difficult is for a channeled particle to "leak out" of a row). This fact is also contained within equations 3.13 and 3.16, where the critical channeling angle is found to increase with decrease in the atomic spacing of a row.

2. DEFECTS OCCURING IN FCC AND BCC CRYSTALS

Defects, i.e. faults in the perfect crystal structure of a material, are almost always present in a crystal to a greater or lesser extent.

Generally defects may be divided into four types:
- point defects (vacancies and interstitials)
- line defects (dislocations)
- planar defects (stacking faults, faulted dislocation loops and grain boundaries)
- volume defects (voids, gas bubbles, precipitates and amorphous regions).

As is explained in greater detail in Chapter 6, the bombardment of energetic ions into fcc and bcc metals initially results in the formation of generally unstable vacancy (i.e. "missing atom") agglomerates called "voids". In the case of fcc metals these voids (which occur at depths corresponding roughly to the LSS predicted range of the ion) readily collapse onto low index planes where they form dislocation loops. The ensuing brief discussion of the types of dislocation loops and defects generally found in fcc and bcc metals, is followed by a more detailed description of the character and mobility of these defects.

In fcc crystals, vacancy–type sessile faulted Frank dislocation loops with $\bar{b} = \frac{a}{3} <111>$ have been observed as a result of void collapse.[44,45] These loops are in the form of discs of missing atoms lying on the {111} planes of the fcc structure. In silver and copper (both metals possessing low stacking energies) the Frank loops have been observed to undergo further dissociation towards stacking fault tetrahedra by the Silcox–Hirsh mechanism. With increase in the irradiation temperature of copper, English and Eyre[45] found an increase in the number of perfect glissile $\bar{b} = \frac{a}{2} <110>$ loops (with a simultaneous decrease in faulted loops).

Kirk et al.[46] found the voids in the bcc metal, α–Fe, not to collapse to loops very easily, except when using very high ion doses. Jenkins et al.[47], using low dose (10^{-12} ions cm^{-2}) 80 keV heavy ions to produce damage in iron foils, found TEM visible damage in the form of $\bar{b} = \frac{a}{2} <111>$ and $\bar{b} = a <100>$ vacancy dislocation loops. Irradiation with ions lighter than Ge caused no visible damage. Haussermann[48], also finding $\frac{a}{2} <111>$ vacancy dislocation loops in bcc molybdenum and tungsten, found the amount of damage to be appreciably smaller than that incurred by fcc copper and gold crystals irradiated under identical conditions.

Besides the presence of vacancy–type defects occuring roughly within the LSS range for ions, much deeper interstitial–type damage has been observed especially in the case of fcc crystals (see Chapter 6). This deep damage has been observed to be in the form of a dense network of dislocation loops and small defect clusters[49,50].

3. STACKING FAULTS AND DISLOCATION LOOPS

Insertion or removal of an extra half plane resulting in a disruption of

the stacking sequence of planes parallel to a plane under observation causes a two–dimensional disruption of the crystal called a stacking fault. If this disruption only occurs on a small section of a plane (i.e. the disruption is bounded on all sides by the "perfect" lattice structure) the defect is called a dislocation loop. Dislocation loops are generally found lying on low index planes of both fcc and bcc crystals. Depending on the planes on which they lie as well as on the degree of edge or screw character they possess, dis–location loops may be sessile (i.e. they will not slip if a stress is applied) or glissile (mobile).
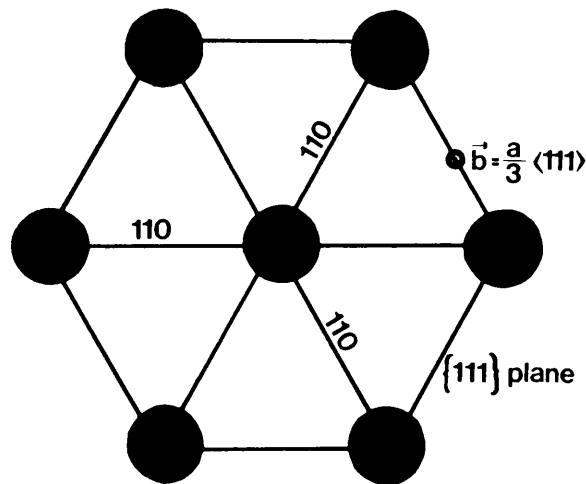
Figure 4.4 The hexagonal stacking fault on the {111} plane.

Dislocations may be perfect or faulted. An example of a faulted loop is that of the Frank dislocation loop that occurs on the {111} planes of fcc crystals (see figure 4.4). The insertion or removal of a {111} plane disrupts the regular ABCABC stacking sequence and results in a faulted area descri–bed by a hexagonal stacking sequence, e.g. BCBC. A single Frank dislocation loop is formed by the removal of the {111} plane while a double Frank loop is formed by its insertion $\left(\text{see figures 4.5(a) and (b)}\right)$. The burgers vector of a Frank dislocation, $\bar{b} = \frac{a}{3} <111>$, lies normal to the {111} plane in the <111> direction. It is immobile on this plane.
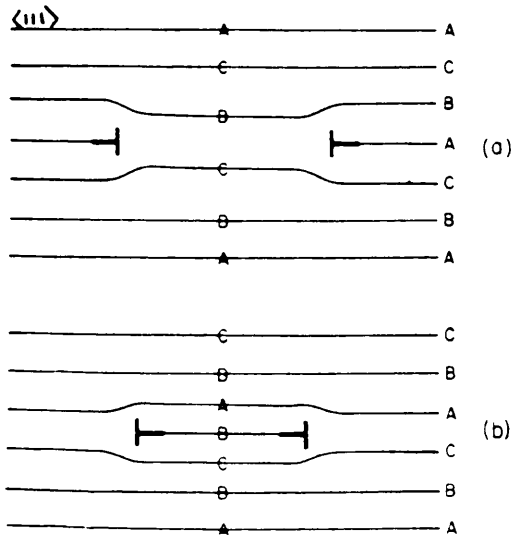
Figure 4.5 (*Ref. 52b*)   The (*a*) single and (*b*) double Frank stacking faults in an fcc crystal

While the stacking sequence is disrupted for a faulted loop, this does not occur in the case of a perfect dislocation. An example of a perfect dislocation loop is the $\bar{b} = \frac{a}{2} <100>$ loop which has been found to occur in fcc copper at elevated temperatures. Removal of a {100} plane in an fcc crystal does not disrupt the stacking sequence of atoms in the <110> direction. This is because all atoms are situated directly above or below one another in the <110> direction (see figure 4.6). Disruption is only present at the circumference of the "inserted" (interstitial–type) or "removed" (vacancy–type) plane and not inside the loop as occurs for the faulted instance. The defect is thus in the form of a closed one–dimensional dislocation line or "perfect prismatic dislocation loop". This loop is glissile in the <110> direction.

Perfect dislocation loops with $\vec{b} = \frac{a}{2} <111>$ lying on {110} planes are found in bcc crystals. An attempt to create Frank dislocations along the {110} closest packed planes of bcc crystals (which have an ABABAB stacking sequence with no possibility of a C position) will result in the juxtaposition
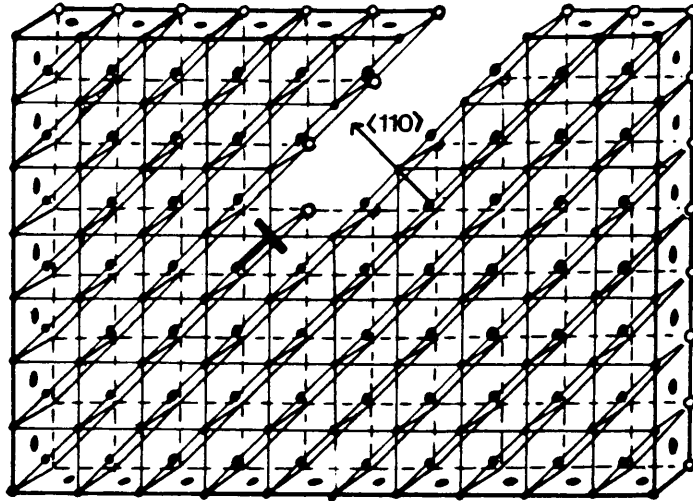
Figure 4.6 The removal of a {110} plane does not disrupt the fcc stacking sequence in the <110> direction.

of two A planes or two B planes. In order to restore the proper stacking sequence the planes may shift in a direction parallel to themselves. The ABABAB stacking sequence will then be restored except at the circumference of the removed or inserted plane, once more resulting in the formation of a perfect dislocation loop. Such $\frac{a}{2}$ <111> dislocations in bcc crystals are glissile, i.e. they become mobile on their slip planes under stress.

4. SLIP AND CLIMB

Defects have been found to move when subjected to low stresses or to increases in temperature.

During the process of slip one part of the crystal slides as a unit across an adjacent part. The surface along which slip occurs is known as the slip plane. Slip generally occurs along the close–packed planes of crystals, such as the {111} planes in fcc metals and the {110} and {211} planes in bcc metals. The preferred slip direction is along the line of closest atomic packing, i.e. the <110> direction in fcc and the <111> direction in bcc metals. (When

inhomogenous stresses are applied to a circular (or prismatic) perfect dislocation loop, it can be made to slip in a direction normal to the plane on which it lies.) Due to the phenomenon of slip, application of relatively low stresses on a crystal may result in the diffusion of defects out through the crystal surfaces with a resultant restoration of the perfect lattice structure inside the crystal.

When vacancies are present in a material, diffusion of these defects (due to an increase in temperature) may cause a dislocation to "climb". Figure 4.7 illustrates how lattice vacancies precipitating along an existing edge dislocation can eat away a portion of the extra half plane of atoms, causing the dislocation to "climb" at right angles to the slip direction. The migration of defects out of a crystal during annealing may be described by this process of climb.

(a)   (b)   (c)
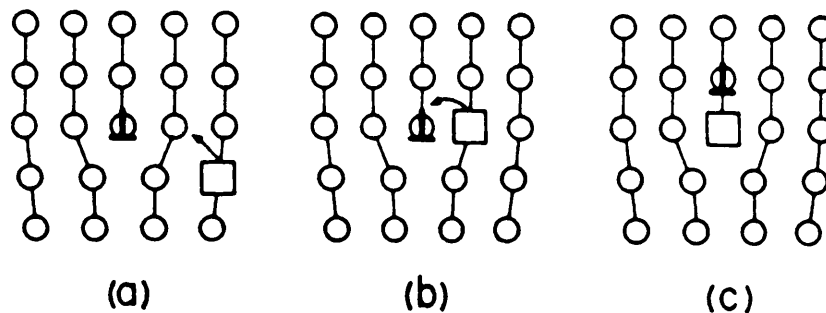
Figure 4.7 (Ref. 52c) The "climb" of an edge dislocation.

5. THE SELF–ENERGY OF A DISLOCATION

The displacement field of a dislocation line or stacking fault represents stored energy. This energy is called the "self–energy" of a dislocation and

has a magnitude proportional to the square of the burgers vector of the dislocation. Due to the energy stored within them, dislocations are found to exert either repulsive or attractive forces on one another. Such forces may either lead to mutual annihilation or to the conglomeration of high concentrations of defects in certain areas of a crystal.

6. THE PEIERLS–NABARRO FORCE

Due to the periodic potential existing between atoms in an ordered lattice structure, the self–energy of a dislocation moving through a crystal fluctuates with its position. Two possible periodic variations of dislocation energy with position are shown in figure 4.8.
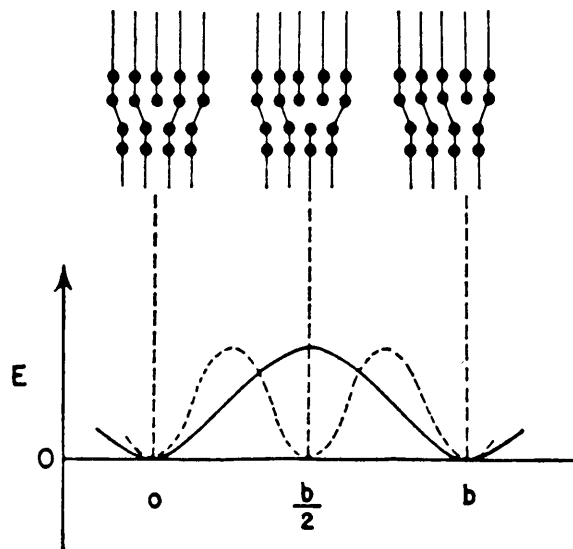
Figure 4.8 (Ref. 52d) Schematic diagram of the energy of an edge dislocation as a function of its position in the lattice.

A consequence of the periodic self–energy associated with a dislocation is the existence of a periodic force exerted by the lattice on dislocations. The

force is greatest where the slope of the energy curve is a maximum. An external force greater than this maximum force must be applied to a dislocation lined up along a crystallographic direction if the dislocation is to move freely over considerable distances. Peierls[51] was the first to draw attention to the periodic nature of the force a lattice exerts on a dislocation. The first extensive calculation of its magnitude was attempted by Nabarro. Thus the force is called a Peierls or Peierls–Nabarro force. A simplified calculation of the Peierls stress of a screw dislocation has been done by Weertman and Weertman[52a].

The Peierls stress opposes dislocation motion and is expected to decrease with increasing crystal temperature due to the greater ease of movement of defects at higher temperatures.

The Peierls stress opposing dislocation motion on a slip plane, also decreases with increasing planar packing density. Due to its overall lower atomic density, one would therefore expect the Peierls force in a bcc crystal to generally be larger than the force in a fcc crystal.

CHAPTER 5

DECHANNELING AT DEFECTS

1. INTRODUCTION

Distortion of a lattice due to the presence of defects decreases the steering effect experienced by a channeled ion, eventually resulting in dechanneling of the particle. The probability that dechanneling will occur is expressed by the "dechanneling cross section" which is dependent on both the nature and size of the defects as well as on the charge and energy of the channeled particle. The channeling technique can be used to provide information on both the amount of disorder (which is proportional to the magnitude of the dechanneling cross section) as well as on the depth of the damage incurred by an irradiated crystal. The energy dependence of the dechanneling cross section further yields information about the type of defects causing the dechanneling.

2. RUTHERFORD BACKSCATTERING SPECTRA OF RADIATION DAMAGED SINGLE CRYSTALS: ANALYSIS OF DECHANNELING YIELD TO OBTAIN AN INDICATION OF THE DECHAN–NELING CROSS SECTION

A typical energy spectrum of 450 keV channeled protons backscattered from boron–implanted Si is illustrated in figure 5.1[53] and provides a useful basis from which to discuss general dechanneling concepts. The insert in this figure contains a schematic diagram of the sample from which the spectrum has been obtained. It may be seen that disorder (in this case the formation of amorphous Si) has occurred in the region B at a certain depth below the surface.
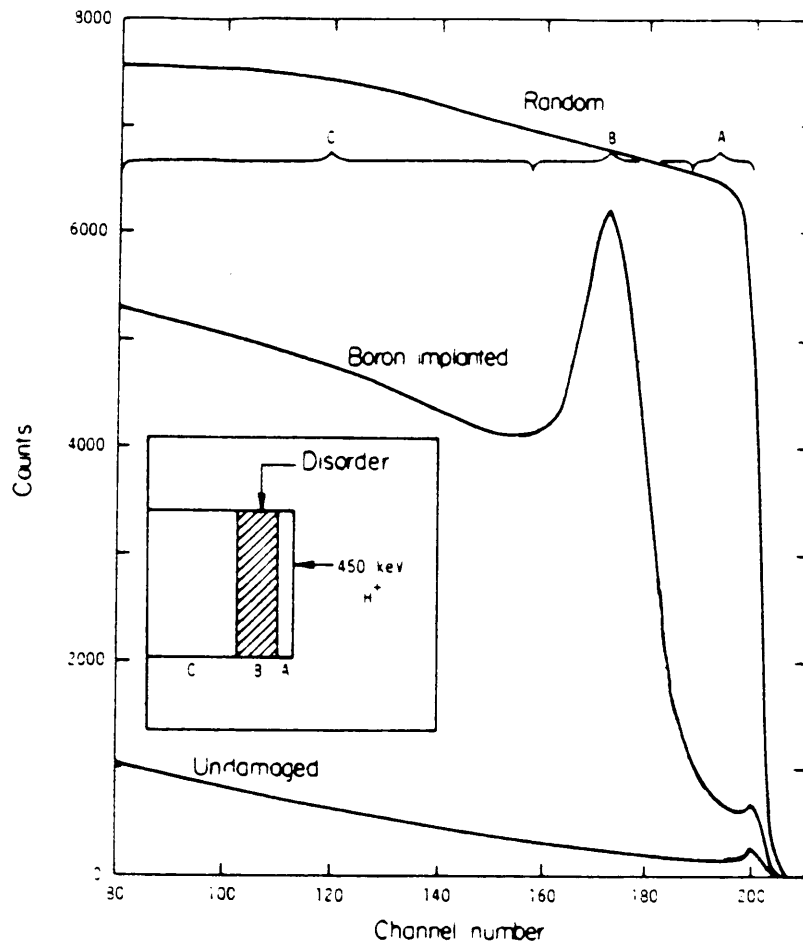
Figure 5.1 (*Ref. 53*) *A dechanneling spectrum of damaged silicon.* (*Damage occurs in region B of the insert.*)

The peak of the backscattering yield observed in the corresponding region B of the <110> damage spectrum is due to the scattering of initially channeled protons by displaced Si atoms in the damaged region of the crystal. The scattering yield from region C of the crystal, which is below the damaged region, is higher than the yield observed from the same depth in the undamaged crystal. This is due to the fact that the component of the incident beam managing to stay channeled during its progress through the damaged region B, emerges into the undamaged region C with a larger angular spread, and therefore has associated with it a larger dechanneling probability than is the case for particles at a similar depth in the undamaged

sample. Particles in the damaged sample will therefore, besides being dechanneled in region B, also have a larger probability of being dechanneled in region C, thereby causing a rise in the yield in both regions B and C.

The total dechanneling yield obtained from a damaged sample, and collected in a certain channel number m of its RBS spectrum, is not a direct indication of the density of the defects lying at the depth x corresponding to the channel number in question. (It is therefore also not an indication of the dechanneling cross section existing due to the defects at x.) The reason for this is the fact that the incoming analyzing beam (aligned along the specific axis) consists of both a random and a channeled fraction (refer to section 1 of Chapter 3). All channeled particles arriving at x, undergoing dechanneling specifically due to the defects at x, and eventually being detected in the backscattering experiment, constitute that fraction of the dechanneling yield (in channel number m) indicative of the defect density at x. The other contribution to the total dechanneling yield in channel number m is the yield due to backscattering of the random fraction at x. (As discussed in Chapter 3 the random fraction progressively increases with distance below the surface due to incremental beam divergence caused by interactions with thermally vibrating row atoms as well as with electrons.) If this random contribution can be separated from the total RBS yield at x, an indication of the dechanneling cross section (due to defects at x) can be obtained.

Such a separation may be achieved by bringing the dechanneling yield (at x) of the virgin (undamaged) spectrum into account. For a perfect crystal (no damage existing at x) the dechanneling yield from depth x is only due to backscattering of the random fraction of the incident beam. (An incident ion dechanneled (due, say, to the incremental beam divergence which causes delayed dechanneling) *at* x, is considered to be part of the random

fraction.) If $\chi_v(x)$ is the aligned yield normalized to the random yield in the virgin crystal, and $\chi_D(x)$ is the corresponding quantity in the damaged crystal, then the probability $P(x)$ for a projectile to be dechanneled at depth x is given by:

$$P(x) \quad = \quad \frac{\chi_D(x) - \chi_v(x)}{1 - \chi_v(x)} \qquad\qquad 5.1$$

$P(x)$ is an indication of the dechanneling cross section at x.

Quéré[54,55] as well as Grob and Siffert[56] assumed a simple additive form of both the channeled and random fraction contributions to the total dechanneling yield from x. They formulated the loss of channeled ion flux (Φ) per unit length at depth x as follows:

$$\frac{d\Phi}{dx} \quad = \quad -\, \Phi(x)[\xi + \sum_i \sigma_i N_i(x)] \qquad\qquad 5.2$$

where ξ describes the random fraction contribution to the loss of channeled ion flux and σ_i is the dechanneling cross section of type i defects whose concentration at x is $N_i(x)$.

Grob and Siffert resolved equation 5.2 and obtained for one specific type of defect i:

$$\Phi(x) \quad = \quad \Phi_v(x) e^{-\int_0^x \sigma_i N_i(z)dz} \qquad\qquad 5.3$$

where $\Phi_v(x) \quad = \quad \Phi_0 e^{-\xi x}$

and $\Phi_0 \quad = \quad \Phi_{beam}(1 - \chi_{min})$

where χ_{min} is the surface minimum yield and Φ_{beam} is the incident beam flux before any interaction with the target.

Grob and Siffert expressed the probability $P(x)$ for a projectile to be dechanneled at a depth x on a defect of type i in terms of the dechanneling flux:

$$P(x) \;=\; \frac{\Phi_v(x) - \Phi(x)}{\Phi_v(x)} \tag{5.4}$$

Substitution of 5.3 in 5.4 yields:

$$P(x) \;=\; 1 - e^{-\int_0^x \sigma_i N_i(z)dz} \tag{5.5}$$

Eliminating $P(x)$ from equations 5.1 and 5.5 yields:

$$\frac{\chi_D(x) - \chi_v(x)}{1 - \chi_v(x)} + 1 \;=\; e^{-\int_0^x \sigma_i N_i(z)dz}$$

$$-\ln \frac{1 - \chi_D(x)}{1 - \chi_v(x)} \;=\; \int_0^x \sigma_i N_i(z)dz$$

$$=\; I(x) \tag{5.6}$$

$I(x)$ is called the integrated dechanneling probability due to defects and is directly proportional to the dechanneling cross section σ_i.

3. A DAMAGE "KNEE"

In the case of crystalline metals the damage induced by ion irradiation is in the form of dislocations (see Chapters 4 and 6). Because dislocations usually lie on similar crystal planes their presence serves to collectively increase the channeling angle of all channeled analyzing ions. This results in an overall increase in the dechanneling probability of all channeled ions reaching the damaged region. Instead of a definite damage peak as illustrated in figure 5.1 (such a peak indicates the formation of amorphous surface material), the spectrum of the dislocation–type damage is typified by a distinctive damage "knee" or "kink" which is observed at the channel number corresponding to the maximum damage range (see figure 5.2). The high dechanneling probability of all channeled ions reaching the end of the damage region causes the backscattering yield not to decrease beyond the damage knee.
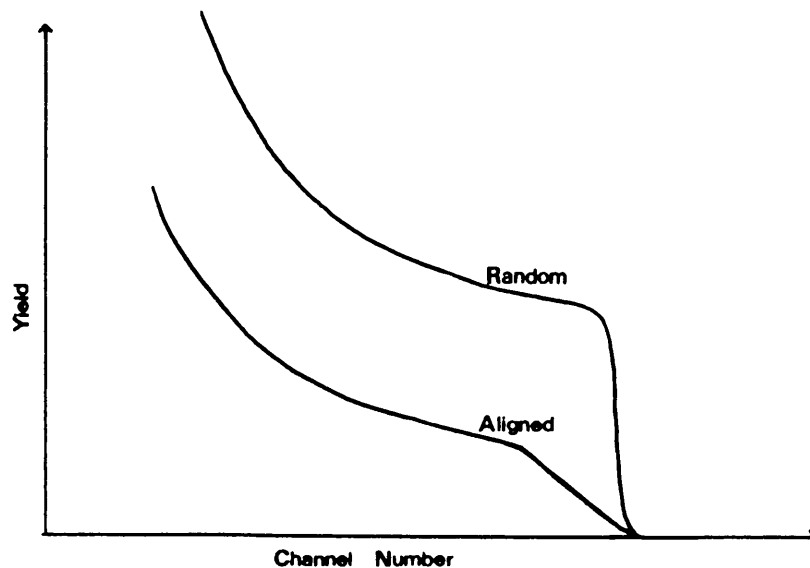
Figure 5.2 Dislocation–type damage is typified by the "knee" in the damage spectrum.

4. DEFECTS THAT CAUSE DECHANNELING

Dechanneling at defects can be due to obstruction, distortion or to both simultaneously.

(i) Obstructional defects

An obstructional defect, such as a point defect, a stacking fault, a grain boundary or a void, causes only a very small amount of distortion in its immediate neighbourhood. Such a defect will only cause dechanneling when the channeled particle hits it directly.

The dechanneling cross section is assumed to be negligibly small for isolated point defects (vacancies and interstitials). Jousset et al.[57] found that the dechanneling cross section, σ_p, for planar dechanneling due to interstitials could be expressed as follows:

$$\sigma_p = \frac{z_1 z_2 e^2 L \pi}{2\sqrt{E\,V(x_c)}} \qquad 5.7$$

where L = the halfwidth (in length units) of the channel

x_c = the maximum allowed value of x; x being the distance measured from the midpoint between two planes

$V(x_c)$ = a simplified power law planar potential

E = the energy of the channeled particle

The $E^{-\frac{1}{2}}$ dependence of σ_p was confirmed in experiments by the same authors. Such a dependence was also obtained by Lindgreen[58]. Axial dechanneling due to interstitials was found to have a much smaller cross section than that for the planar case[59]. This can be expected due to the higher potential barrier associated with an axial channel.

Quéré[55] formulates the cross section due to dechanneling at a stacking fault, as follows:

$$\sigma_{SF} \;=\; pS \qquad\qquad\qquad 5.8$$

where σ_{SF} = the dechanneling cross section for a stacking fault

p = an energy independent dechanneling probability

S = the projected surface of the stacking fault

The dechanneling cross section for a stacking fault is not affected by a change in energy of the channeled particle.

Figure 5.3 illustrates four situations which can occur when an initially channeled particle comes across a stacking fault. The channeling can be made worse (case 1) or beter (case 2), dechanne—ling may occur at the stacking fault (case 3), or dechanneling may occur further on (case 4).
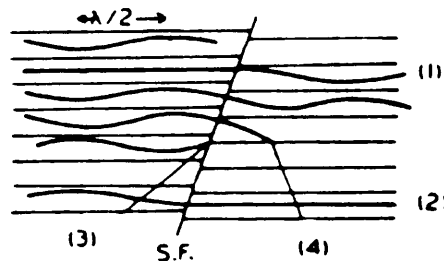
Figure 5.3 (*Ref. 97*) *An illustration of what occurs when an initially channeled particle encounters a stacking fault.*

In general the total channeling stopping power is not changed due to the presence of a stacking fault. This is because channeled ions have an equal probability to either increase (case 1) or decrease

(case 2) their transverse energies at the fault. (The effect of a defect on channeled energy loss has been theoretically demonstrated to be quite negligible also in the cases of dislocations and hydrogen interstitials[60].)

(ii)   **Distortional defects**

Defects which cause large distortions in relatively large regions in the surrounding lattice are called distortional defects. Examples of such defects are straight dislocations, dislocation loops and clusters. Distortion dechanneling results from some extra transverse energy given to channeled ions by the curvature of channels in the neighbourhood of the defect. Figure 5.4 illustrates how the distortion is the greatest near the core of an edge dislocation and then decreases with distance as the radius of curvature around the dislocation increases. Quéré[61] defines a "dechanneling cylinder" around the dislocation axis in which volume the amount of distortion is large enough to allow dechanneling. Outside this cylinder the dislocation has no further effect on dechanneling.

The mean diameter of the dechanneling cylinder has been defined by Quéré[61]:

For axial channeling: $\bar{A}_x(E) = \left(\dfrac{bdaE}{\alpha\, z_1 z_2 e^2}\right)^{\frac{1}{2}}$ 5.9

For planar channeling: $\bar{A}_p(E) = \left(\dfrac{bE}{8,6 z_1 z_2 e^2 N d_p}\right)^{\frac{1}{2}}$ 5.10
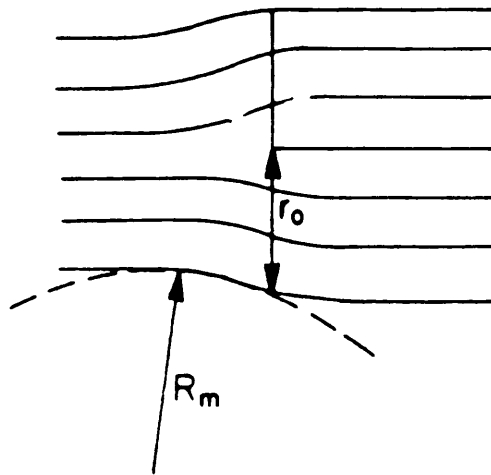
Figure 5.4 (Ref. 97) R_m *is the minimum radius of curvature of a channel at a distance* r_o *from an edge dislocation. At distances greater than* r_o *the radius of curvature is too large to influence the dechanneling probability of a channeled particle.*

where   d and d_p are respectively the widths of the axial or planar channel

b   =   the burgers vector of the dislocation

N   =   the atomic density of the material

E   =   the energy of the channeled ion

a   =   the Thomas Fermi screening radius

α takes on different values depending on whether the dislocation is edge, screw or mixed

The diameter of the dechanneling cylinder defines the dechanneling cross section per unit length (λ) of a dislocation. Both equations 5.6 and 5.7 indicate λ to be proportional to the square root of the energy of the channeled ion, although the absolute value of λ is much larger for the planar than for the axial case.

Mory and Quéré[43] found that equations 5.6 and 5.7 slightly overestimated the dechanneling probability due to various factors such as the possible dissociation of dislocations and the instance of non–straight dislocations (loops) not being taken into account. Mory and Ligeon[60] suggested the following equation for the dechanneling cross section per unit length of a dislocation loop:

$$\lambda(d) \;=\; \lambda_\infty \cdot \frac{d}{d + d_0} \qquad\qquad 5.11$$

where λ_∞ = λ for a straight dislocation

d = the diameter of the dislocation loop

d_0 = an adjustable parameter.

(iii) Identification of defects

Different types of defects and the depths at which they occur in a material may be identified by finding the relationship between dechanneling yield and energy of the incident beam at a certain depth. If the yield does not change with increase in beam energy, the presence of stacking faults or voids may be suspected. An $E^{\frac{1}{2}}$ dependence of the yield indicates the presence of dislocations, while a $E^{-\frac{1}{2}}$ value points to interstitial point defects being the cause of dechanneling. This identification is, however, not simple to achieve due to mixtures of different types of defects that may exist.

CHAPTER 6

HEAVY ION RADIATION DAMAGE AND THE TEMPERATURE DEPENDENCE THEREOF

1. INTRODUCTION

The reaction of the target atoms to energetic ions bombarded into various metals is considered in this chapter. One would expect a considerable amount of agitation to be introduced among the constituent metal atoms as a result of such ion bombardment (leading to defect formation as discussed in Chapter 4). Whether the extent of the agitation among the target atoms would coincide with or lie shallower or deeper than the depth of the implanted ions (as predicted by the LSS theory) and whether the range profile of the target atom disruption would be broader or thinner than that of the final incident ion distribution would depend on factors such as the amount of energy transferred to the target atoms (and what happens after the initial transfer).

Radiation damage profiles in the fcc crystals copper,[49,50,62,63,64,65,66] nickel[67] aluminium[50] and platinum[65] have been observed by various authors to lie many times deeper than the depths predicted by the LSS mean projected ranges of ions in the amorphous counterparts of these metals. The half width of the damage profiles have also been found to be broader than those predicted by the LSS theory[63]. The damage in the bcc metal α–iron has been found to be only slightly deeper than the LSS ion range for amorphous iron[65,67], although Linker et al.[68] has found considerably larger damages ranges in bcc vanadium than predicted by LSS. RBS dechanneling techniques have proved useful in the investigation of these deep damage ranges. From various dechanneling studies[49,50] it is known that the radiation

damage in single crystals consists of two parts: a shallow part extending to a depth roughly coinciding with the range of the implanted particles in the amorphous material as predicted by LSS range theory, and a deep part extending to much greater depths.

The shallow part of the damage has been observed to consist mainly of vacancy–type defects found in the region where cascade formation takes place.[45,49,50] The mechanism of collapse of the vacancy–rich inner cores of cascades to form vacancy–type dislocation loops is used to explain the presence of defects in the shallow damage region. The deep component of irradiation damage has been found to consist mainly of interstitial–type defects.[49]

For self–ion implantation in Cu, Vos and Boerma[49] found the deep damage ranges to increase gradually with increase in implantation temperature from 77 K to 660 K. This was also found by Lindgreen et al.[50,58] who self–implanted copper at both 300 and 555 K. Friedland and Alberts[65] similarly found damage ranges in Ar^+–implanted copper to increase from 77 to 300 K. While Sood and Dearnaley[63] found the deep damage ranges to increase for Mo^+ implantations into copper when increasing the substrate temperature from 77 to 300 K, they surprisingly found the deep damage ranges to decrease quite dramatically above 300 K until at 623 K no damage knee could be discerned in dechanneling spectra. To summarize: for Ar^+ and Cu^+ implantations into copper, damage ranges have been found to increase with increase in implantation temperature throughout the 77–660 K temperature spectrum.[49,50,58,65] The unexpected reverse trend observed for the Mo^+ implantations[63] above 300 K might have something to do with the choice of ion used. Similar dosages and implantation energies were used in all the

examples quoted above. Furthermore all implantations mentioned were done off–axially to avoid channeling as much as possible, the only exception being the work of Vos and Boerma[49] who implanted Cu^+ ions along various low–index <hkl> directions.

An increase in implantation temperature has also been found by various authors to cause a decrease in the levels of both shallow and deep components of the damage.[50,63,64] At sufficiently high temperatures a virtually defect free zone has been observed between the shallow and deep regions in copper.[49,50]

An important aspect to bear in mind as regards the influence of implantation temperature on deep radiation damage is that the temperature–dependent damage is incurred *during* implantation at the temperature of interest. Vos and Boerma[49] implanted copper crystals at room temperature and found that subsequent annealing to an elevated temperature, T, did not produce the same type of damage that was observed for the crystal implanted *at* the temperature T.

Three explanations have been proposed by various authors for the occurrence of deep, mainly interstitial–type damage in single crystals:

(i)   Sood and Dearnaley[63], Lindgreen et al.[50,58] and Vos and Boerma[49] proposed that deep radiation damage is caused by the migration of highly mobile self–interstitial atoms, which form clusters or loops at greater depths.

(ii)   Friedland et al.[64] considered an energy–dependent driving force,

created by strongly time–dependent strain–field gradients along the ion tracks, to be the major cause of deep radiation damage. Every ion stopped may create a shock–wave due to fast thermal expansions which can travel deep into the bulk. Defects, initially created in the shallow (cascade) region, may then be propagated deeper into the crystal under influence of this strain field. Sood and Dearnaley[63] also considered a compressive stress to be the cause of defect propagation, but suggested that such a stress was created due to defect accumulation in the lattice. (This explanation can, however, not explain the fact that damage ranges have generally been found to have either no[64] or very small[45] dosage dependence.)

(iii)   Diehl et al.[69], Eyre[70], Friedland et al.[64], Ecker et al.[40] Vos and Boerma[49] as well as Borders and Poate[62] discussed the probability that channeling could be responsible for the deep penetration of defects into single crystals. Although ions directed exactly in a main axial direction can be expected to penetrate deeper than the LSS projected ion range (due to channeling) the possibility that such channeled ions would be the cause of the deep damage is small due to the fact that only a small fraction of such ions penetrate to the R_{max} channeling depth defined by Davies et al.[42] (see Chapter 3 section 9)[64,67]. Deep radiation damage ranges have also been observed in single crystals which were implanted at angles well off low index <hkl> directions (as mentioned earlier) where the channeled component reaching R_{max} is expected to be even smaller.

In order to discuss all three these explanations in more detail, and thereby to obtain a greater understanding of the temperature dependence of deep radiation damage, an overview of the basic mechanisms and parameters

involved in radiation damage processes is given in sections 2 to 6. The current discussion is resumed in section 7.

2. THE FORMATION OF POINT DEFECTS

For the energy range of implanted ions used in this study, a considerable component of the projectile energy is lost through interaction with electrons. Due to the nature of the metallic bond (positive nuclei, vibrating around lattice sites, are surrounded by a "sea" of non–localized electrons) the electronic structure of a metal can quickly recover and no permanent damage is caused by electronic excitation. (The energy transferred to electrons is dissipated as heat.)

The mainly elastic nuclear interactions, however, do lead to radiation damage. According to classical elastic scattering theory[27], the incident ion transfers the following amount of energy to the first atom (nucleus) it encounters: (this atom is called the "primary knock–on atom" or PKA)

$$E = \frac{4E_0 M_1 M_2}{(M_1 + M_2)^2} \sin^2\left(\frac{\theta}{2}\right) \qquad 6.1$$

where
E_0 = the energy of the incident ion
M_1 = the mass of the incident ion
M_2 = the mass of the target ion
θ = the centre of mass scattering angle

The maximum energy transferred to the PKA occurs for a head–on collision, where $\theta = 180°$. Whatever the angle of collision, however, if the

energy transferred to the PKA is larger than a certain threshold energy, E_d, the lattice atom will vacate its regular position thereby leaving an empty lattice site or "vacancy" behind. The PKA may come to rest at an interstitial non–lattice site within the material. Collectively, such a "self–interstitial atom" (or SIA) and the vacancy left behind by it are known as a "Frenkel pair" (see figure 6.1). Both SIA's and vacancies are examples of point defects.
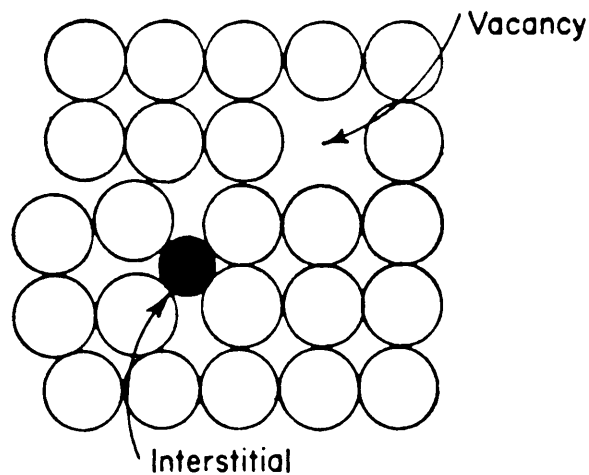
Figure 6.1 (Ref. 52e) A Frenkel pair.

The threshold energy for creating a permanently displaced interstitial, E_d, is anisotropic and has a value ranging between 15 and 50 eV (the smallest value is in the direction of the most densely packed atomic row). Since the separation distance of a Frenkel pair created with the threshold energy is only a few lattice parameters, the whole displacement event is completed within 10^{-14} to 10^{-13} seconds. For such a short time the surrounding lattice atoms, though exhibiting thermal vibrations, may be considered to be at rest because, in metals, their frequencies lie below 10^{13} Hz. The eventual response of the lattice to the formation of a Frenkel pair may cause it to

recombine if its constituents are not sufficiently well separated. The volume in which a Frenkel pair is unstable is defined as the "instability volume" [30c] which has a typical size of 100 atoms for metals. This instability volume is both orientation and temperature dependent. Gibson et al.[71] have also reported the existence of such an "annihilation zone" around a vacancy "upon entering which the interstitial atom occupies an ordering position and the vacancy disappears."

3. THE EFFECT OF TEMPERATURE ON THE MOBILITIES OF VACANCIES AND INTERSTITIALS

Townsend et al.[72] relate the amount of defect migration to the temperature by the following equation:

$$E_{act} \simeq 25 \; k_B T \qquad\qquad 6.2$$

where E_{act} = the activation energy for a defect to start migrating

T = the temperature in kelvin

k_B = the Boltzmann constant

This estimation is reasonably accurate for materials such as metals which have lattice vibration frequencies of $\sim 10^{13}$ Hz.

Eyre[70] divided irradiation temperatures into three groups (refer to Table 6.1):

(i) Temperatures at which vacancies and interstitials are both immobile (T < Stage I).

(ii)   Temperatures at which interstitials are mobile but vacancies are immobile (Stage I < T < Stage III).

(iii)   Temperatures at which both vacancies and interstitials are mobile (T > Stage III).

TABLE 6.1

Metal	Structure	Melting point temperature (K)	Stage I (K)	Stage III (K)
Ni	fcc	1728	60	375
Cu	fcc	1357	50	300
α–Fe	bcc	1800	120	375
Pt	fcc	2046	30	600

It is important to discern between two possible processes taking place during irradiation of metals: At low temperatures, where no interstitial or vacancy migration is possible, energetic ions only produce *disordering*. At higher temperatures both disordering and thermal migration of point defects can take place.

4. COLLISION CASCADES

Instead of immediately forming an interstitial, the PKA, if it has sufficient energy (in the order of 1 keV) may displace other atoms from their lattice sites. These secondary knock–on atoms (SKA's) may in turn displace further atoms which in turn create higher order knock–on atoms. This repeated process results in the formation of a displacement cascade which is illustrated in figure 6.2. A single ion can produce a succession of PKA's, (each of which produce a cascade) before it finally comes to rest.
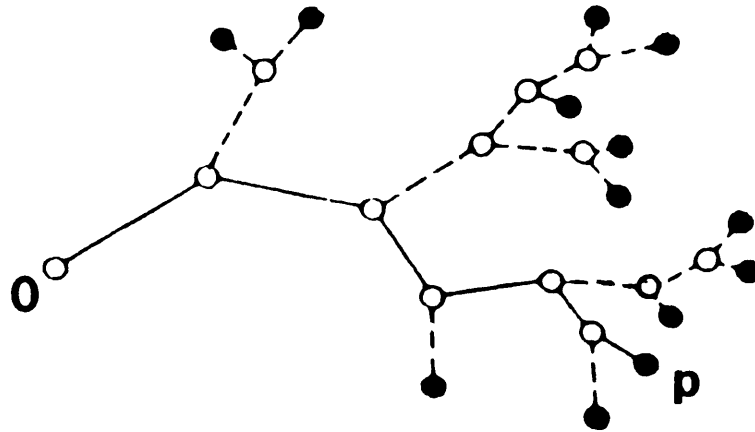
Figure 6.2 (Ref. 30f) Schematic representation of a displacement cascade: O, starting point of the PKA; P, stopping point of the PKA; ——, trajectory of the PKA; ○ vacancies; •, interstials; – – – –, trajectory of higher order knock-ons.

Calculations[73] of the energy distributions for even rather heavy projectile masses and high ion energies reveal that low energy transfers (mostly below 1 keV) are highly favoured between PKA and target atoms. The low energies involved cause the average spatial dimensions of the collision cascades to be rather small compared to the range of the implanted ions, leading to primary damage profiles (the shallow damage component) closely correlated to the projected ion range. The depth at which such displacement cascades occur therefore corresponds roughly to the LSS range of ions in amorphous materials.

Cascade developement with time may be divided into three phases:

(i)   **The collisional or displacement phase**

In this phase (which takes $\sim 10^{-13}$ seconds to complete) a large

number of Frenkel pairs which branch out due to various order knock–on collisions (as shown in figure 6.2) are formed. An example of the number of Frenkel pairs formed in this early stage of cascade development is illustrated in region I of figure 6.3. (This graph was obtained from a computer simulation for a 2,5 keV cascade in a bcc crystal.[74b])
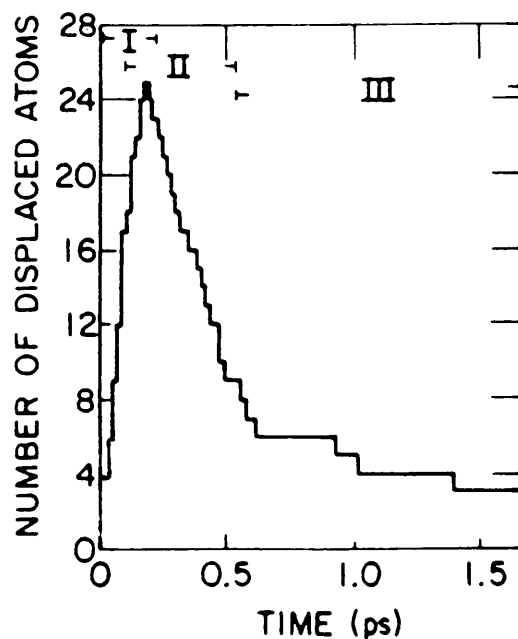
Figure 6.3 (Ref. 74b) The time evolution of the number of Frenkel pairs formed in a collision cascade.

During the collisional phase there is a tendency for vacancies to be located more towards the centre of the cascade region (CR) (where they form a "depleted zone") while interstitials tend to cluster at the peripheries of the cascade forming a shell around the vacancy–rich zone. This segregation of defects in a cascade can be understood if one considers the evolution of the displacement cascade as an explosion which starts at a point (first displacement), the extending front to the undisturbed lattice being formed by newly

displaced interstitials while the vacancies stay behind.

(ii)   **The Thermal Spike phase**

At the end of the collisional phase of the cascade, the relatively small percentage of the lattice atoms that took part in the cascade process, are in a highly excited (kinetic) state, while the rest of the lattice atoms in this volume remain unaffected. (An "athermal" state of excitation exists.) During the thermal spike phase the energy of the excited atoms is distributed among *all* the atoms in the cascade volume. (This distribution takes place mostly by way of pair collisional processes.[75]) All the atoms in the CR are therefore in a highly excited thermal vibrational state, a state to which a certain "highly localized temperature" as well as an "energy density" may be assigned. This state of agitation corresponds to Seitz and Koehlers'[76] concept of the "thermal spike" and lasts for $10^{-12} - 10^{-10}$ seconds, during which time the localized thermal energy is dissipated into the surrounding lattice until thermal equilibrium is finally attained. Temperatures as high as 10^4 K have been proposed to exist in the inner core of the CR during this ultra–short period of time[77]. (The inner cascade region may therefore be viewed as "molten".) During the thermal spike the centre or core of the cascade is therefore considered to be the hottest region, from where the temperature slowly decreases to the peripheries of the CR. Such a temperature gradient between the core and periphery of the cascade was observed by Averback et al.[78] in a molecular dynamic simulation of radiation damage in copper (using the relationship $E_k = \frac{3}{2} k_B T$ per atom). They found the average temperature in the centre of the cascade (radius < 10 Å) to be about 5000 K, and the temperature gradient outside the core to

be about 300 K/Å. The temperature only began to fall below the melting temperature of copper at about r = 17 Å, a radius which closely corresponds to the radius of the "disordered zone" obtained in their calculations. (MDS calculations are discussed at a later stage.)

Due to the high temperatures associated with the thermal spike, both vacancies and interstitials can be considered to be highly mobile in the cascade region. The larger the thermal gradient between the core and periphery of the CR, the larger the effect of the "thermo–transport" mechanism proposed by Protasov and Chudinov[75]. By thermo–transport is meant the phenomenon that vacancies produced in the displacement phase of the cascade migrate from its peripheries, up the thermal gradient to the centre of the cascade, where they form a region of high vacancy concentration (a "void"). Due to self–intersitial atoms diffusing to the peripheries of the cascade region and beyond (by way of replacement collision sequences – see next section), the cascade region at the end of the thermal spike phase is found to consist of a vacancy–rich core surrounded by high concentrations of interstitials (which tend to form clusters[78]). The size and concentration of the vacancy–rich core is determined by factors such as the size of the temperature gradient associated with the thermal spike as well as its lifetime.

The combination of thermo–transport of vacancies and diffusion of SIA's is an additional mechanism to explain defect segregation in a cascade, a process which has already been explained in the previous section using the collisional model.

Kapinos and Platinov[79] proposed a second mechanism for defect segregation occuring during the thermal spike phase. Their

description involves the nucleation of large vacancy clusters during the cooling stage of the thermal spike.

During the thermal spike stage of the cascade, computer simulations have shown that the large number of Frenkel pairs formed in the initial collisional phase drop rather drastically to a value much smaller than that predicted by the modified Kinchin–Pease expression.[80]

$$N(E) \sim \xi(m) \cdot \frac{E}{2E_d} \qquad\qquad 6.3$$

where N(E)   =   the average number of Frenkel pairs created by a PKA with energy E in a random collision cascade

E_d =   the effective displacement threshold energy

$\xi(m)$ =   varies between 0 and 1

According to the original Kinchin–Pease model[81] N(E) obeys the boundary condition:

$$N(E) \;=\; \left\{ \begin{array}{ll} 0 & E < E_d \\ 1 & E_d < E \leq 2E_d \end{array} \right\} \quad \text{for}$$

This model, however assumes hard–sphere scattering which leads to an overestimate of N(E). (A higher portion of energy is actually spent in subthreshold collisions $(E < E_d)$ than hard sphere scattering, and thus less Frenkel pairs are actually produced.)

The reason for the sharp reduction in the number of vacancies and interstitials at the end of the thermal spike phase (refer to

region II in figure 6.3) is obviously due to all the spontaneous recombination processes taking place in the "thermally agitated" state of the cascade.

Two important parameters used in the study of thermal spikes are "thermal spike lifetime" and "energy density". The lifetime of the thermal spike (TS) describes the time necessary to attain equipartion of energy, i.e. the time needed for the cascade to cool down to ambient temperature. The TS lifetime depends on the size of the temperature gradient between the cascade core and the outer crystal. The TS lifetime is also dependent on the thermal conductivity of the metal in which it occurs. The time duration of the thermal spike is of importance as it is a determining factor as regards the amount and type of defects eventually formed.

The term "energy density" (ED) of the TS refers to the amount of energy per atom distributed in the cascade region. It is a temperature dependent property of each material. Kim et al.[82] show the energy densities for metals used in this study to decrease in the following order: (the last 3 densities do not differ greatly)

$$ED_{Pt} > ED_{Cu} > ED_{Ni} > ED_{Fe}$$

This ordering corresponds to the ordering of the mass densities of the materials.

(iii)   **The relaxation phase**

At this stage the thermal energy of phase two has dissipated so that thermal equilibrium of the cascade region with the rest of the

crystal has been reached. In the relaxation phase, which lasts between 10^{-9} and 10^{-7} seconds, the lattice reacts to the formation of the cascade, e.g. the vacancy–rich core may collapse to form dislocation loops. Further Frenkel pair recombination can also take place as indicated in region III of figure 6.3. The number of Frenkel pairs slowly tends towards a value of one third of the Kinchin–Pease estimate.

It has been observed by various authors that the number of point defects after the final stage of the cascade is considerably overestimated by the Kinchin–Pease expression. Averback et al.[73] found the increase in the resistivity of copper foils after implantation with heavy ions to lead to a damage efficiency of only 35% relative to the modified Kinchin–Pease expression. Molecular dynamic simulations by Averback et al.[78] furthermore show that a 5 keV cascade in copper finally produces little more than 10 stable Frenkel defects whilst the Kinchin–Pease model predicts about 80. The overestimation of Frenkel pairs by the modified Kinchin–Pease expression is brought about by a *single* substitution of the *full ion* energy into equation 6.3. Friedland and Alberts[65] in their study of deep radiation damage in various metals used the TRIM programme to predict the number of vacancies created by various 100 keV ions. Because the TRIM code carries out the modified Kinchin–Pease calculation for *each* PKA, the number of vacancies reported by Friedland and Alberts[65] were considerably less than would have been the case had the *full ion* energy been substituted a single time into equation 6.3. Sood and Dearnaley[63] also found the amount of disorder induced by Cu, Au and Mo ions in copper to be considerably smaller than the Kinchin–Pease estimate.

5. REPLACEMENT COLLISION SEQUENCES (RCS)

A primary knock–on atom may displace a host atom from its lattice site but not retain enough energy to escape from that site after the collision. Such an event is called a "replacement collision". The knocked out atom may similarly proceed to knock out and take the lattice site of its nearest neighbour, the neighbour in its turn doing the same to the atom closest to it (see figure 6.4). Such a "replacement collision sequence" (RCS), focussed along a low index axis of the crystal, may cause an interstitial with relatively little energy to migrate unexpectedly large distances into the crystal, eventually coming to rest at an interstitial site when the kinetic energy has dissipated sufficiently so that no further replacements can occur. RCS therefore enable the formation of a stable, well separated Frenkel pair.

Silsbee[83] hypothesized that such atom–atom collision sequences were focussed along major crystallographic directions by way of an impulse, transferred from one atom to another, gradually coming closer and closer to the axis of the atomic sequence along which the energy is transferred. Kirk and Blewitt[84], in their investigation of radiation damage in ordered Ni_3Mn obtained very direct evidence for the existence and magnitude of RCS. Diehl et al.[69] proposed RCS to be responsible for the deep penetration of damage into copper and gold foils irradiated with 1–5 keV Ar ions.

Replacement collision sequences, which are most likely to occur at energies near the displacement threshold energy, E_d, occur mostly along the <110> and <100> close–packed directions for fcc crystals[85] and the <111> direction for bcc crystals. Due to RCS occuring at the extending front of a
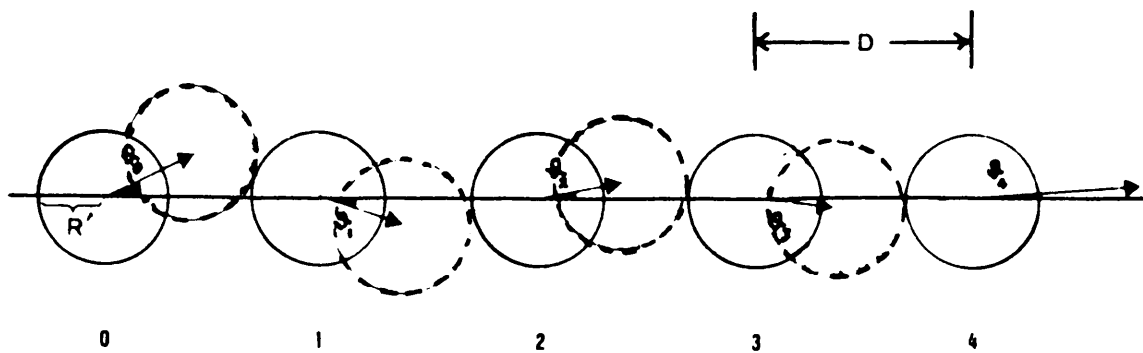
Figure 6.4 (Ref. 30g) Successive collisions along a row of equally spaced hard spheres.

cascade, the cascade develops principly in these close–packed directions[86b] (see figure 6.5).

The effect of elevated temperatures on RCS

Elevated temperatures, causing increasing thermal vibrations of host atoms around their lattice sites, have a defocussing effect on replacement collision sequences. Sequences that, with zero thermal vibration, could cause an interstitial to come to rest at about 200 atomic spacings from its nascent vacancy[87], become increasingly shorter with increase in irradiation temperature. The effect of temperature increase in the direction of cascade development is illustrated in figure 6.5. Agranovich and Kirsanov[86a] calculated crowdion trajectories (i.e. long chains of correlated displacements) in α–Fe at various temperatures by using Monte Carlo computer simulations. They found the trajectory of a 50 eV PKA suffering RCS along the <111> direction to extend over 22 interatomic distances, d. Incorporation of zero point vibrations resulted in a decrease of trajectory to 11d and at T = 42 K the sequence extended only over 8 atomic distances. Diehl et al.[69] found the ratio between room temperature and 130 K implantation of 1–5 keV Ar^+ ions to be 0,6 for Cu and 0,8 for Au.
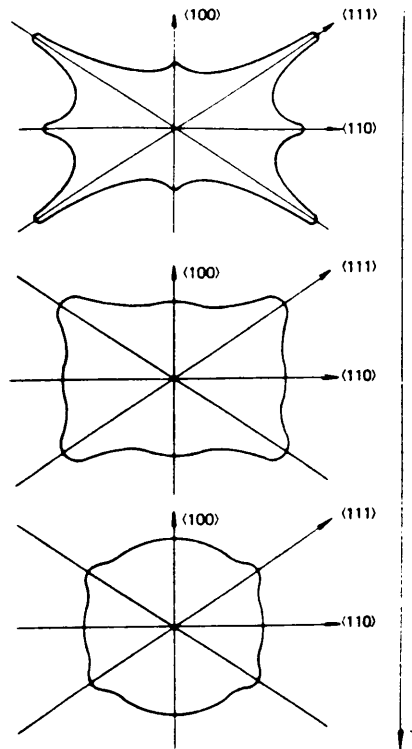
Figure 6.5 (Ref. 86b) The displacement threshold energy is dependent on the crystal direction. This anisotropy decreases with increase in crystal temperature. (As calculated for α–Fe by Kirsanov.)

This discovered reduction of crowdion trajectories with increase in temperature leads to a significant effect, namely to spatial localization of collision sequences. Self–interstitial atoms unable to escape the cascade volume due to increased lattice vibrations, cause there to be an intensification of recombination and replacement processes within the cascade region itself, leading to intensification of the thermal spike.

Kim et al.[82] stated that such collective motion in the CR during the thermal spike phase is the main cause of "ion beam mixing" (IM), i.e. diffusion induced in a metal by ion irradiation. They did a systematic study of the spread (or diffusion) of tracer impurities in thin metal films and concluded that such atomic mixing took place primarily during the thermal

spike phase of cascade development (the collisional phase contribution to IM was considered to be only of secondary importance). The greater the ion mixing of tracer impurities in metals, the greater therefore the amount of thermal agitation and collective motion taking place in the cascade zone during the TS phase.

Kim et al.[82] investigated the dependence of IM on matrix and thermo-chemical properties such as target mass, cohesive energy and energy density. Figure 6.6 contains a plot of mixing efficiency as a function of the square of the energy density (the ordinate) and as a function of the inverse square of the cohesive energy (the abscissa). Ion mixing or "mixing efficiency" values are situated inside the circles. The cohesive energy decreases from left to right on the abscissa. Also indicated are values of the melting point tempe-ratures for metals of interest to this study.
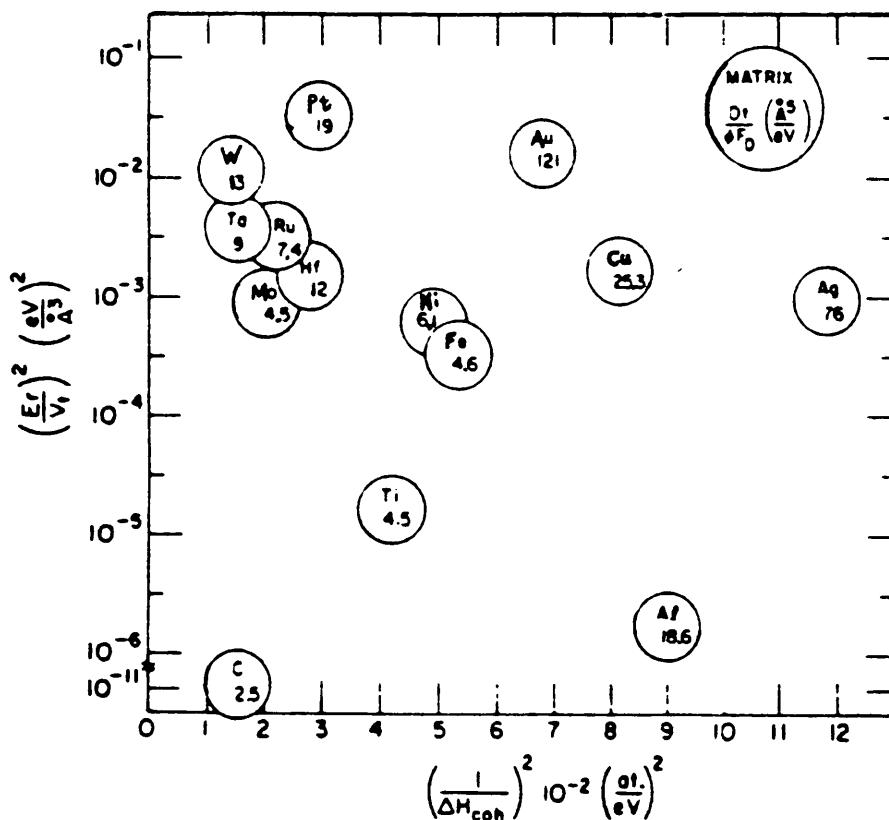
Figure 6.6 (Ref. 82) Mixing efficiency as a function of both the square of the energy density and the inverse square of the cohesive energy.

As might be expected, the mixing efficiency increases with increase in energy density (i.e. energy per atom in the CR during the TS phase) for elements with similar cohesive energies (and therefore also similar melting point temperatures). The ion beam mixing is also seen to increase with atomic mass for elements of similar energy densities.

The differences in deep damage incurred by various metals may be explained from figure 6.6. This will be done in section 7.

6. MOLECULAR DYNAMIC SIMULATIONS (MDS)

In order to review the general philosophy behind MDS one of the first applications as discussed by Gibson et al.[71] will briefly be described: By computer modelling they considered a Cu crystallite (at zero kelvin) containing a reasonably large number of atoms which interacted according to a Born–Mayer type potential. Atoms on the surface of the crystallite are supplied with extra forces simulating the reaction of atoms outside, as though the crystallite were imbedded in an infinite matrix. One atom is then initially endowed with an arbitrary kinetic energy and direction of motion, as though it had been struck by a bombarding particle. A high speed computer then integrates the classical equations of motion for the whole set of atoms inside the crystallite. The dynamic state (degree of disorder) of the whole crystallite is therefore followed by the computer (as opposed to the "static" type Monte Carlo simulations described earlier where the trajectory of an incident ion interacting with undisplaced lattice (or random) atoms is followed). After lattice agitation has died down below a certain threshold, a second ion is introduced and the whole calculation is done again; this process is repeated until sufficient statistics have been obtained.

The computer programme of Gibson et al.[71] was used to study various properties of lattice defects permitted by the model. Limitations of the calculations were small crystallite sizes (500–1000 atoms) and limited allowable energies for the PKA. (Due to the relatively large boundary surfaces of small crystallites, too large PKA energies would cause boundary effects to adversely influence the accuracy of calculations.)

With increase in computer capacity larger crystallites, disordered by more energetic PKA's, have been modelled. In 1988 Averback et al.[78] summarized results of MDS calculations of cascades in Cu and Ni at energies up to 5 keV. By way of molecular dynamic simulations both Averback et al.[78], as well as Protasov and Chudinov[75] have observed the important role played by the thermal spike in many properties of energetic displacement cascades. Figure 6.7 shows a disordered zone in a crystallite modelled by Protasov and Chudinov[75]. Though full MDS of highly energetic cascades is probably
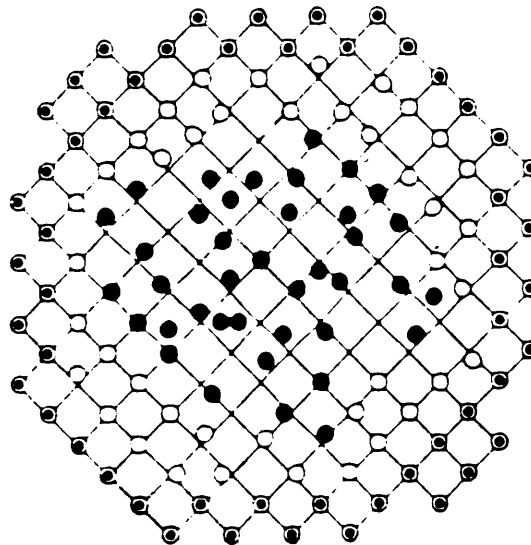
Figure 6.7 (Ref. 75) Spontaneous sites of atoms of the central part of a crystallite at the instant $\tau = 2 \cdot 10^{-12}$s (plane 100 of Cu); $\bigcirc$ denotes mobile atoms remaining at the initially given lattice sites, $\bullet$ denotes atoms which have left their initial sites; $\odot$ are immobile atoms.

beyond the scope of present day computers[88], investigations of cascade evolution during the thermal spike phase have been made possible by this computing technique.

7. EXPLANATIONS FOR THE OCCURRENCE OF DEEP RADIATION DAMAGE

The various explanations given for the occurrence of deep radiation damage will now be discussed in more detail. The influence of irradiation temperature on radiation damage will also be investigated.

(i) **The possibility that deep radiation damage might be caused by the migration of highly mobile interstitials to form clusters and loops at greater depths.**

Both Vos and Boerma[49] as well as Lindgreen et al.[50] proposed this explanation of deep damage formation. Although they did not discuss a possible mechanism as to how interstitial migration actually occurred, Diehl et al.[69] have proposed that replacement collision sequences could be the mechanism for deep interstitial migration.

The extent of RCS has, however, been shown to decrease with increase in irradiation temperature.[69,86b] This would be inconsistent with general observations of increase in the range of deep radiation damage with increase in irradiation temperature.[49,50]

Although replacement collision sequences have been reported to extend over 200 atomic spacings[87], such calculations omitted thermal vibrations of lattice atoms. Computations by Averback[78] as well as Agranovich and Kirsanov[86] taking such thermal activity into account, reveal that RCS rarely exceed distances of more than twenty atomic

lattice positions. Thermal migration of interstitials by way of RCS does therefore not provide a consistent explanation of deep radiation damage. Another mechanism for interstitial migration would have to be proposed.

As mentioned in section 4 of this chapter, the molecular dynamic simulations of Averback et al.[78] as well as the example illustrated in figure 6.3 show that significantly less stable Frenkel defects are finally formed than predicted by the modified Kinchin–Pease expression. It seems therefore unlikely that sufficient numbers of self–interstitial atoms are produced to effect the observed high damage density in the deep damage region (even if they manage to penetrate that far by interstitial migration).

Friedland et al.[65,67,89] considered the enormous differences in ranges of deep radiation damage observed in different metals and found this to be inconsistent with an interstitial migration theory due to the fact that the migration energies for interstitials are quite similar in many solids. (Sood and Dearnaley[63] quotes the migration energies in Cu to be as follows: for vacancies: 1,05 eV; for interstitials: 0,71 eV.)

Using the interstitial migration theory Lindgreen et al.[50] gave an explanation for the sharpness of the "kink" observed in the dechanneling spectrum corresponding to the deep radiation damage region. (The sharp kink indicates a rather sudden cut–off between the damaged and non–damaged regions.) After explaining the mechanism of interstitial clusters forming dislocation entanglements, and thereby creating the deep damage, they stated that the depth

limit at which such loop entanglement could occur must be sharp. Lindgreen said that at the outer limits of the deep damage region, the concentration of mobile defects becomes too low for fusion into large clusters. According to Lindgreen, the probability for cluster formation is proportional to C^n (where C is the concentration of coagulating defects and $n \geq 2$). Therefore the cut–off point between the situation where the interstitial concentration is high enough for coagulation and the situation where interstitial concentration is too low for cluster formation (and subsequent dislocation entanglent, thereby creating the deep damage) is sharp. However, if such a cut–off exists, one would expect the sharpness of the kink to be dependent on the ion dosage. Only a weak implantation dosage dependence has, however, been observed for deep damage ranges in Cu.[58] Friedland and Alberts[67], assuming an exponential type decrease in point defect density with depth and a continuous decrease in cluster formation with decrease in number of point defects, felt that the interstitial migration theory could not explain the sharpness of the "knee" in the damage spectrum.

(ii)   **The possibility that deep radiation damage is caused by a compressive stress field gradient propagating defects into the crystal**

It has already been discussed how most of the kinetic energy of the PKA is transformed to thermal energy resulting in the thermal spike associated with cascade development. Especially for heavy ions, this heat energy is released into a very small volume resulting in very high energy densities within the cascade region. One reason for the occurrence of such high energy densities is the fact that the lifetime of the thermal spike is an order of magnitude larger than the stopping time of the ion and therefore all the cascades created

by one single ion interact simultaneously with the lattice. For instance they all simultaneously release energy due to Frenkel pair recombination within the relatively small cascade region. In addition the phonon energy due to subthreshold collisions is released at the same time. Extremely high temperatures can then be expected to exist for a very short period in the vicinity of the ion track. Even if one assumes that a large amount of energy is dispersed by the electron gas it is feasible to assume that, due to thermal expansion, a strong stress field gradient will exist for a very short period of time.

Although it has been shown that considerably less interstitials are formed than predicted by the modified Kinchin–Pease expression, small interstitial–type clusters or loops that may have developed due to previous cascade damage (e.g. due to migration of interstitials to the peripheries of a previous cascade and subsequent clustering) may exist just beyond the molten region of the specific cascade under observation. Vacancy–type loops due to previous void collapse also exist. Both these interstitial– and vacancy–type defects may be propagated deep into the bulk of the material when subjected to the high stress field or shock wave.[90,91] The range of such dislocation propagation would depend on the crystal structure of the material because the Peierls force, resisting dislocation motion, depends sensitively on the crystal structure.

Although both vacancy– and interstial–type defects may be propagated, Vos and Boerma[49] explained that the final deep damage would be more of the interstitial–type due to the larger capture radius of interstitial loops for capture of interstitials as compared to

the radius for the capture of vacancies at vacancy loops.

The increase in deep radiation damage with increase in irradiation temperature might also be explained using the thermal spike model. Although crowdion trajectories have been found to be small, the definite reduction of these trajectories with increase in temperature (due to defocussing of replacement collision sequences by thermally vibrating lattice atoms) and the subsequent increase in localized replacement and recombination processes, lead to the intensification of the thermal spike (as discussed earlier). Such intensification is due to the increased amount of thermal motion within the cascade region, as well as to greater amounts of energy being released due to more Frenkel pair recombination incidents. An intensified thermal spike will have associated with it a greater stress field. Interstitial–type defects will therefore be propagated deeper into the crystal the higher the implantation temperature. Defect propagation should also be easier the higher the temperature of the substrate due to the fact that the Peierls force decreases with increasing temperature.

As the defect structures formed in the cascade regions in fcc crystals are rather immobile (as discussed in Chapter 4 the dislocation loops are of the $\vec{b} = \frac{a}{3} <111>$ type which are sessile) one would not expect these defects to move easily to form the damage that has been observed in the deeper radiation damaged regions of fcc crystals. A stress field of sufficient strength could however cause such defects to propagate. Furthermore, as mentioned in Chapter 4, evidence that defects in fcc structures become more mobile with increase in irradiation temperature has been supplied by

English and Eyre.[45] They found the number of sessile $\vec{b}$ = $\frac{a}{3}$ <111> Frank dislocation loops (initially formed in copper) to gradually decrease with increase in temperature whilst the number of perfect glissile $\vec{b}$ = $\frac{a}{3}$ <211> type loops simultaneously increased. (Although these defects were of the vacancy–type one might expect similar trends for interstitial–type defects lying in the cascade region.)

The effect of lattice atomic number on the deep component of irradiation damage has been investigated: Friedland and Alberts[67] found deep damage ranges in nickel to be appreciably smaller than those found in copper[89] under similar irradiation conditions. The deep damage produced in α–iron was found to be significantly shallower than found in either nickel or copper. In their study of deep damage incurred in single crystals of copper, platinum and α–iron, Friedland et al.[65] found extremely large, but comparable, damage ranges in copper and platinum, but once more found the range in iron to be much smaller.

Still using the model of stress field propagation due to the existence of a thermal spike, but turning now to the relationship between energy density, cohesive energy, melting temperatures and ion beam mixing as discussed by Kim et al.[82], one may interpret these differences observed in the deep radiation damaged regions of the various metal crystals: (refer to figure 6.6)

Copper and nickel both have similar energy densities. For identical incident ion energies and irradiation temperatures, both

therefore experience similar average distributions of energy per atom during the collisional phase of cascade development. Cu, however, possesses lower cohesive energy between constituent atoms (and therefore also a lower melting point temperature) and will therefore experience a greater amount of agitation inside the cascade region than Ni, which has a similar energy density but higher cohesive energy. Evidence that this is so is given by the higher IM value for Cu determined experimentally by Kim et al.[82], as well as obtained through MDS calculations by Averback et al.[78] Cu can therefore be expected to yield a more intense thermal spike than Ni irradiated under similar conditions, thereby causing defects to propagate deeper into Cu than into Ni.

Pt, as may be seen from figure 6.6, possesses a higher energy density than Cu and will therefore absorb more energy per atom in the TS phase than Cu. It, however, also possesses a higher cohesive energy than copper. These two opposing tendencies could counterbalance and cause both metals to experience similar amounts of agitation inside the cascade zone (corresponding to the similar IM values obtained by Kim et al.[82]). Similar thermal spike intensities leading to similar deep radiation damage depths will therefore result.

The phenomenon that deep radiation damage ranges in alpha iron have been found to be smaller than those found in similarly irradiated fcc metals[65,67] may be explained if one takes into account the strong dependence of dislocation motion on the crystal structure of a material. The bcc–structure of α–iron has a lower packing density than that of the fcc ordering and therefore the Peierls force opposing glide along planes of highest density in iron should be

appreciably larger than in the case of fcc metals. This would result in defects not being able to propagate as far into iron as they are able to in fcc crystals.

The collapse of voids to dislocation loops has been found to occur at temperatures as low as 20 or 30 kelvin.[46,92] The fact that a void can collapse at temperatures where (according to Table 6.1) both vacancies and interstitials are immobile (i.e. "athermal collapse" occurs) is further evidence for the existence of a "localized melted zone" where both interstitials and vacancies would be highly mobile.[46] Kim et al.[82] suggested the following mechanism for void collapse: The high mobility of vacancies in the thermal spike enables those vacancies created in the collisional phase of the cascade to precipitate out as loops during the lifetime of excitation. Averback et al.[78] suggested a regrowth mechanism for void collapse. Figure 6.8 illustrates void collapse as simulated by Protasov and Chudinov.[75]
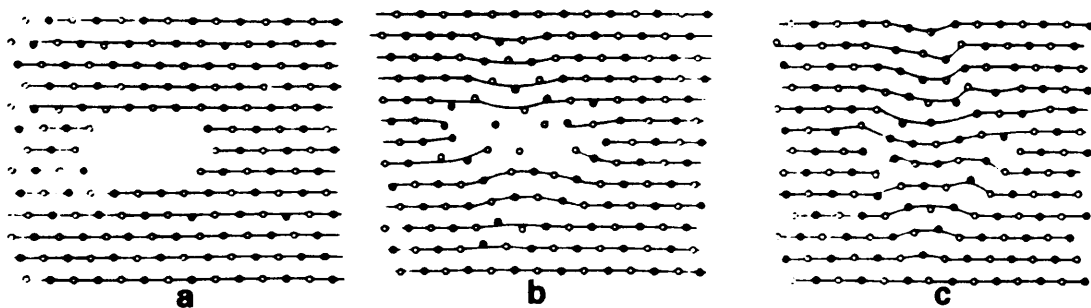
Figure 6.8 (Ref. 75) Successive periods of void evolution at the instants: $\tau = 0$ *s, (b)* $\tau = 2 \cdot 10^{-12}$ *s, (c)* $\tau = 5 \cdot 10^{-12}$ *s [plane (110):* $\bigcirc$*, atoms in the plane of the figure:* $\bullet$*, atoms in the next neigboring parallel plane].*

The overall level (amount) of radiation damage in both shallow and deep regions of self–implanted copper has been found to decrease gradually with increase in implantation temperature.[48,49] This phenomenon may also be explained within the compressive stress field model. According to Table 6.1, vacancies in copper become increasingly mobile from 300 K upwards. An increased implantation temperature should therefore allow an increased amount of vacancies to be emitted from the cascade volumes (in the shallow damage region) before onset of the thermal spike. The resulting voids should therefore be smaller and more stable after dissipation of the spike and are not expected to collapse as readily to form dislocation loops. The possibility exists that stable voids are not propagated as easily by the compressive stress (produced by the thermal spike). Only the small number of dislocations formed by voids that *did* collapse would then be propagated to the deep damage region – thereby explaining the decrease in the amount of deep damage observed with increase in implantation temperature. Vacancy emission may also cause the final *number* of voids in the shallow damage region to be less, further explaining the decrease in shallow damage levels with increase in implantation temperature. The very sharp decrease in damage levels that has been observed[45,64] in Cu for implantation at temperatures of 550 K and above could also be due to large amounts of vacancies being emitted from both voids and loops at these temperatures. The relatively defect–free zone reported[49,50] to exist between the shallow and deep damage regions at similarly high irradiation temperatures may also be due to increased vacancy emission: such vacancies (emitted from the shallow cascade region) could recombine with interstitial–type defects in the shallower part of

the deep damage region, thereby virtually clearing this intermediate region of all damage.

Shorter replacement collision sequences (due to defocussing) are also a result of increased implantation temperature, and may provide a further explanation for the decrease in overall damage levels. Reduced crowdion trajectories result in less interstitials being able to escape the cascade volume before onset of the thermal spike. Less interstitial–type loops or clusters will therefore form outside the cascade volume, resulting in there being less such defects available for propagation into the deep damage region. The defect density in both shallow and deep damage regions will therefore decrease with increase in implantation temperature. Less interstitials able to escape the cascade volume before onset of the thermal spike will furthermore result in a greater amount of Frenkel pair recombination processess within the cascade volume. Even if thermal vacancy emission did not occur, the subsequent voids would be smaller, in size and number, resulting in the formation of less overall damage as explained in the previous paragraph.

The number of Frenkel defects have been found both experimentally[73] and by computer simulation[78] to be considerably less than predicted by the modified Kinchin–Pease formula. This observation may have two explanations within the stress field model: Firstly, the very localized temperature within the cascade volume during the thermal spike phase of cascade evolution is expected to cause many initially formed Frenkel pairs to be annihilated within this "molten" volume. Secondly, the compressive stress field set up by the thermal spike will not necessarily only propagate defects

deeper into the crystal. An equal probability exists for the defects to be propagated in the opposite direction towards the surface. Many initially formed defects might then be annihilated at the surface, thereby causing observed damage levels to be less than predicted by the Kinchin–Pease estimate.

(iii) **The possibility that channeling could be responsible for deep radiation damage.**

In Chapter 3 section 9 an example was discussed in which channeled particles were found to reach (and exceed) depths coinciding with the deep damage ranges which have been reported. Various authors have reported similar findings in tungsten[37,42] (bcc) as well as in nickel[40], copper and gold[41] (fcc). Using figure 3.9 as an example it may be seen that, for beam incidence exactly along a channeling axis, generally a fairly small percentage of channeled particles reach the deep radiation damage depths. Due to the insufficient numbers involved, it is considered unlikely that the relatively few ions penetrating well past the LSS ion range could induce sufficient agitation to cause the relatively high levels of radiation damage that has been observed. Only for beam incidence exactly into the <100> and <111> directions do about 40% to 50% of the particles come to rest at depths significantly exceeding the LSS ion range. Although radiation damage might be induced by such a relatively higher percentage of ions (depending on the initial dosage), the fact that most of the damage ranges quoted in section 1 were induced for heavy ion beam incidence well off any main crystal axis, seems to rule out the possibility that high numbers of channeled ions could be held responsible for the deep damage.

In favour of channeling as a mechanism for deep damage production, the strong implantation orientation dependence of the deep damage range observed by Vos and Boerma[49] at temperatures up to 300 K, deserves mention at this stage. For copper self–implanted directly into the <110> direction they found the *damage* range to lie significantly deeper than for implantation 18° off the <110> direction. This is consistent with the decrease in channeled Ni ion penetration with increasing angle away from a main axial direction as observed in copper by Ecker et al.[39]. At temperatures of 300 K and less it therefore seems likely that channeling plays a significant role in deep damage production. This might have something to do with the larger channeling half angles existing at low temperatures which could cause a significantly larger amount of particles to reach depths coinciding with observed deep damage ranges. (Vos and Boerma[49] did not, however, mention whether an investigation had been done on the orientation dependence of damage ranges at temperatures *above* 300 K.)

Further evidence however exists that excludes the possibility of channeling being a significant mechanism in the production of deep damage:

The gradual increase in the deep damage range with increase in irradiation temperature which has been reported[49,50] is not consistent with the findings of Davies et al.[42] who proved (within a 3% experimental error) that the maximum channeling range R_{max} is completely independent of the lattice temperature.

Furthermore the gradually tapering off of channeling ranges for fcc crystals observed by Whitton[41] is not consistent with the rather sharp damage cut–off seen on RBS dechanneling spectra of irradiated fcc crystals.

Evidence that channeling cannot be held solely responsible for deep radiation damage has been cited by Diehl et al.[69]. Normal irradiation on copper and gold single crystal foils (having both <110> and <100> normals) was done at both 1 and 5 keV. A shift of only 40 Å in the damage distribution peaks was observed for these two different implantation energies, whereas a much larger shift would have been expected if channeling were the dominant process.

Oen and Robinson[93] (who modified the Kinchin–Pease expression to incorporate the possibility of channeling) suggested that once an energetic atom enters a channel it is much less effective in producing displacements since all its energy can be frittered away in sub–threshold collisions. This possibility further suggests that the role which channeling plays in the production of deep radiation damage might be slight.

CHAPTER 7

EXPERIMENTAL

SUMMARY

Radiation–induced damage was inspected in single crystals of Cu, Ni, α–Fe and Pt by analysis of dechanneling spectra of alpha particles accelerated by a Van de Graaff accelerator. The positions of three low index axes were carefully determined for each undamaged crystal by placing the crystal in a three–axis goniometer and tilting it until a minimum dechanneling yield was obtained. The crystals were then implanted (off–axially) with 150 keV Ar^+ ions at various temperatures. After being allowed to come to room temperature the crystals were once again inspected in the three axial directions previously determined. Experimental damage ranges were determined from the RBS spectra subsequently obtained.

1. EXPERIMENTAL SET–UP

The experimental set–up in this study is schematically illustrated in figure 7.1. The 2,5 MeV Van de Graaff accelerator at the University of Pretoria was used for analysis of the metal single crystals. High purity ^4_2He gas from the ion source within the dome of the accelerator was ionized (to singly charged particles) and subsequently accelerated. Energy selection (1,5 and 1,7 or 1,8 MeV) was achieved by the use of an analyzing magnet. The alpha particle beam was then collimated by two 1 mm apertures placed 3 m apart behind the analyzing magnet. No further focussing elements were used.

The single crystals were mounted on a three–axis goniometer in an

Figure 7.1 The Experimental Set-up.
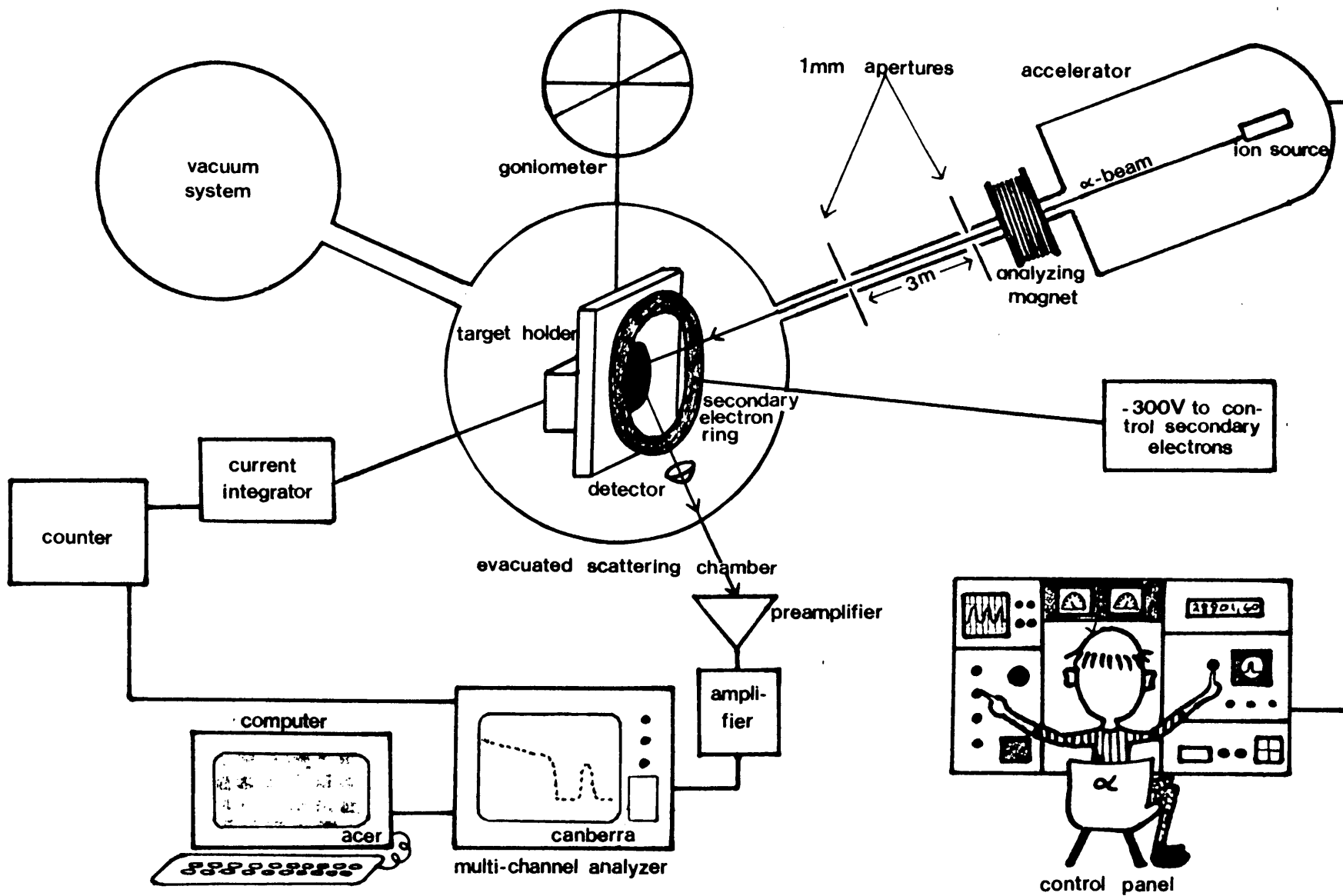
evacuated scattering chamber. Goniometer angles were digitally monitored and could be determined to an accuracy of one tenth of a degree.

An initial vacuum was achieved by use of a rotary pump used in conjunction with a turbomolecular pump. When a vacuum of about 10^{-2} torr had been attained the system was opened to the influence of an ion pump which achieved and maintained a vacuum of about 10^{-6} torr during data aquisition.

The alpha particle beam, which had a divergence of $0,02^{o}$ (which is small relative to critical He channeling angles of about 1°), made a beam spot of 1 mm diameter on the target surface. Direct measurements of beam currents on the target yielded values in the region of 25 nA. Secondary electrons were suppressed by application of a negative voltage of 300 V to an insulated ring in front of the target holder.

Both Ortec and Tennelec silicon surface barrier detectors were used for the detection of backscattered particles. The energy dependent output pulse of the detector system was pre–amplified and amplified by two Ortec amplification units after which the magnitude of the pulse was registered in one of the 512 energy dependent channels of a Canberra Series 80 multichannel analyzer (MCA). The spectrum obtained after sufficient information had been collected was stored in the files of a computer connected to the system.

In order to collect the same amount of *backscattered* charge during each run, a digital current integrator was used in conjunction with a counter to control the total amount of *incident* charge reaching the target surface. Generally $3,6 \times 10^{-6}$ C incident ion charge was collected for 1,5 MeV beam

energies and 5,4 $\times$ 10^{-6} C for the 1,8 MeV instance. More incident charge was collected for the higher energy bombardment due to the indirect proportionality of the differential scattering cross section to the square of the alpha particle energy.

2. DETECTOR CONFIGURATION, ENERGY RESOLUTION AND ELIMINATION OF ELECTRONIC PILE–UP EFFECTS

Figure 7.2 illustrates the configuration of the detector and target mounted inside the evacuated scattering chamber. Although the silicon surface barrier detector used has an active area of 25 mm^2, only $\pi(2,25)^2=15,9$ mm^2 of this surface was exposed to incoming backscattered particles due to the fact that a metal disc with a circular 4,5 mm diameter aperture was placed directly in front of the detector. The reason for the presence of such a partial shield was to prevent too large an amount of particles reaching the detector. Thus electronic pile–up effects were eliminated. (Pile–up effects can cause registration of low energy particles in high energy channels.)
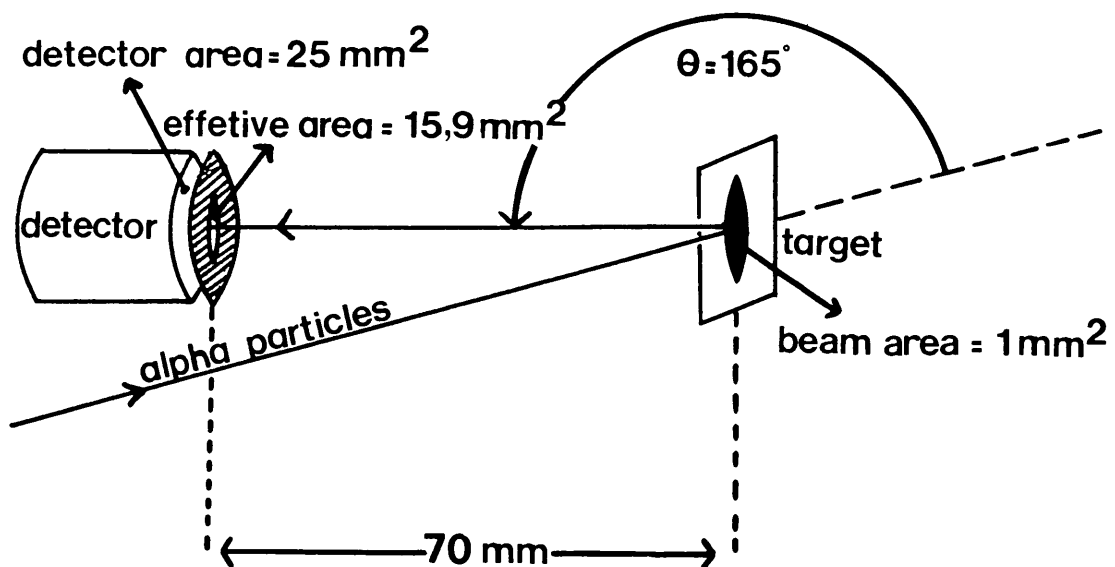
Figure 7.2   Detector and Target Configuration.

The alpha particle Rutherford scattering cross sections at 1,5 MeV (using a scattering angle of 165°) for the various metals of interest to this study are as follows: (in units 10^{-24} cm^2 sr^{-1}) Iron: 0,859; nickel: 1,033; copper: 1,167; platinum: 12,363. The backscattering yield for platinum is expected to be a factor of about 12 larger than the other metals investigated. It was found that the 4,5 mm aperture was too large to prevent a significant amount of pile–up during the analysis of Pt crystals (about 10% dead time was registered on the MCA). Adequate energy resolution could therefore not be attained. While the system resolution for Fe, Ni and Cu was in the region of 13 keV, the corresponding value for Pt was about 25. In order to improve the energy resolution for Pt backscattering an aperture of 2 mm^2 diameter was placed in front of the detector whilst analyzing the Pt samples.

The detector was mounted at a fixed angle of 165° off the direction of the incoming alpha particle beam in a plane containing both the midpoint of the target surface and the analyzing beam. The distance between the detector and the target surface was 70 mm. The solid angle Ω underspanned by the detector was calculated as follows:

$$\Omega \;=\; \frac{A}{r^2} \;=\; \frac{15{,}9}{(70)^2} \;=\; 3{,}2 \times 10^{-3} \text{ sr}$$

Of the various factors influencing the instrumental energy resolution (discussed in Chapter 1 section 5) the dominating component was that due to detector and electronic limitations. As mentioned earlier the beam divergence was only 0,02° and is considered mono–energetic within 1 keV. The lack of energy resolution due to the spread in the kinematic factor was also found to be very small. The latter contribution was calculated as follows:

Figure 7.3 illustrates the extent of the angle θ underspanned at any

point of the target surface by the 4,5 mm diameter effective detector surface: The deviation in scattering angle is then given by $\frac{\theta}{2}$ which was calculated to be 1,8°. The kinematic factors of the various metals were then determined for scattering angles between 165 − 1,8 and 165 + 1,8 degrees and a standard deviation in K of only about 0,09% was obtained. (The higher z_2 the smaller this percentage.)
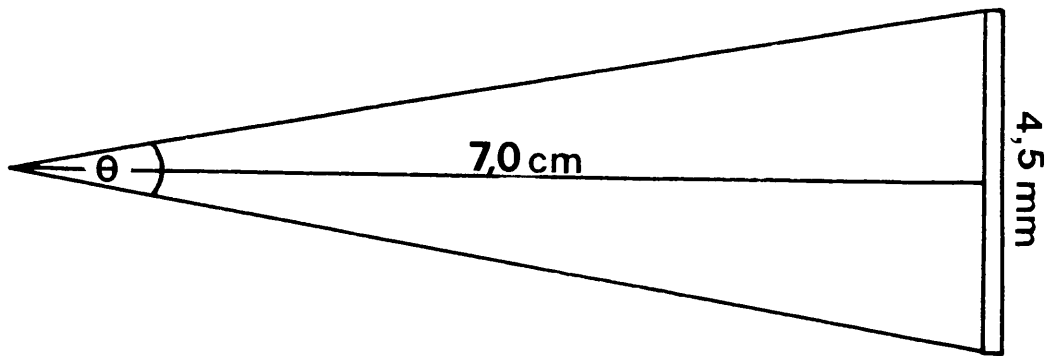
Figure 7.3   The angle θ underspanned by the effective detector surface.

3.   SAMPLE   PREPARATION

Small discs of approximately 2 mm thickness with diameters of 10 mm were cut by a spark erosion technique from single crystal cylinders of copper, nickel, iron and platinum. These cylinders had been grown along either the <100>, <110> or <111> crystallographic directions so that the resulting discs had surfaces normal to one of these orientations.

One face of each disc was mechanically polished with three different diamond resins varying in size from 15, 3 and 0,25 microns (in that order). Each sample was then ultrasonically cleaned in pure ethanol after which it was electrolytically polished in a solution of equal amounts of HNO_3, H_3PO_4 and HCl. This was done to remove the region damaged by the mechanical polishing process.

The quality of the surface was inspected by a dechanneling analysis. If the surface was found to be inadequate for the purposes of implantation and damage analysis the crystal was annealed at a temperature below its melting point in an evacuated oven. This method usually caused realignment of previously disturbed crystal ordering. (When annealing α–Fe the temperature had to be low enough in order to avoid the occurrence of a phase transition.) Subsequent mechanical and electrochemical polishing usually resulted in the crystal attaining the required degree of perfection. It must be noted that the combination of mechanical polishing, electrolytical polishing and annealing was done over varying periods of time and in different orders for the various crystals.

After channeling analysis of virgin crystals the samples were implanted at various temperatures with 150 keV Ar^+ ions using the Varian–Extrion implanter at the University of the Witwatersrand. During implantation the samples were tilted approximately 10° away from the ion beam direction to avoid low index crystal planes. Argon fluences were in the order of 10^{15} ions cm^{-2} at rates of 10^{13} ions $cm^{-2}s^{-1}$. The substrate temperatures were monitored during implantation by using a thermocouple in contact with the back of the target. After implantation the heated samples were allowed to reach room temperature before being exposed to the atmosphere. The samples irradiated at 77 K were however warmed to room temperature under atmospheric conditions. In order to prevent unnecessary oxidation and contamination of the surfaces during transport from Johannesburg to Pretoria all crystals were placed in an evacuated vessel.

4. ENERGY CALIBRATION OF THE MCA

The relationship between the energy and channel number of the MCA is linear within less than 1%. It is therefore only necessary to determine the

energy values corresponding to two different channels in order to achieve an acceptable calibration.

Two random spectra were collected for every axial direction inspected. One spectrum was obtained using a beam energy of 1,5 MeV and another using 1,8 (or 1,7) MeV alpha particles. The KE_0 value was determined for both incident energies and related to the channel number corresponding to the RBS yield halfway between the zero and maximum values of the high energy edge of each spectrum. The difference in KE_0 for 1,5 and 1,8 (or 1,7) MeV incidence was divided by the difference in channel number between the 1,5 and 1,8 (or 1.7) MeV spectrum edges. The value, δE, thereby obtained can then be used to associate a certain energy with each of the 512 channel numbers. δE was found to have values ranging between 2,4 and 3,7 keV per channel.

5. CRYSTAL ALIGNMENT PROCEDURES

Channeling was used as a simple method of orienting the various crystal axes used in this study. At first the crystal was positioned in the goniometer in such a way that its surface was normal to the incident alpha particle beam. (The angle ϕ (as indicated in figure 7.4) was positioned at the zero degrees goniometer setting.) This normal position was expected to be very close to either the <100>, <110> or <111> direction depending on the axis of the cylinder from which the crystal disc had been cut. The orientation of the crystal then proceeded as follows:

The rotational angle α (see figure 7.4) was held constant at the + 4 degrees goniometer setting (therefore roughly 4 degrees off the expected main axial normal direction). The crystal was then slowly tilted in the θ direction from $\theta = + 4^{\circ}$ to $\theta = - 4^{\circ}$ whilst continuously monitoring the RBS yield in

an energy area just below the surface yield of the metal spectrum. A definite sequence of planar minima was detected during the rotation, the positions of which were subsequently plotted on a graph of θ versus α. A similar angular scan and plot was done for α set at -4 degrees, after which the same procedure was carried out keeping θ constant (at respectively $+4$ and -4 degrees) and rotating through α. (During scanning both θ and α were only tilted from positive to negative values, and not in the opposite direction. Only after both angles had been brought up to 2 or 3 degrees *above* the angle at which the scan was to start, and *then* brought down to the correct starting angle, could scanning begin. This had to be done to avoid backlash.)
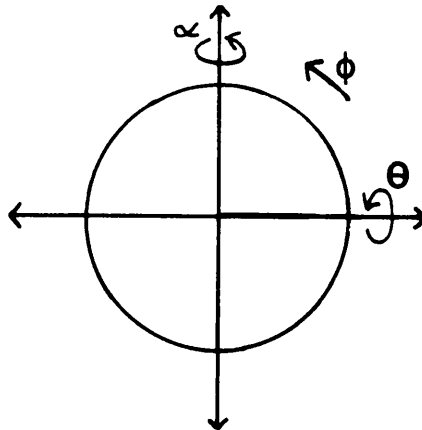
Figure 7.4 The goniometer angles.

The final plot of θ versus α enabled reconstruction of the stereographic projection of the crystal. This was done by connecting the various planar minima in such a way that each connecting line corresponded to a stereo-graphic plane. The intersection of the lines indicated the exact position of the crystal axis around which the tilting had been done in terms of the goniometer angles α and θ.

Plots corresponding to either the <111> stereographic projection (with {211} planes intersecting at 60° intervals as indicated in figure 7.5a), the <110> projection (with the {100} and {110} planes intersecting at right angles – see figure 7.5b), and the <100> projection (with alternating {100} and {110} planes intersecting at 45° intervals as indicated in figure 7.5c) were obtained.

(a) 111 plane   (b) 110 plane   (c) 100 plane
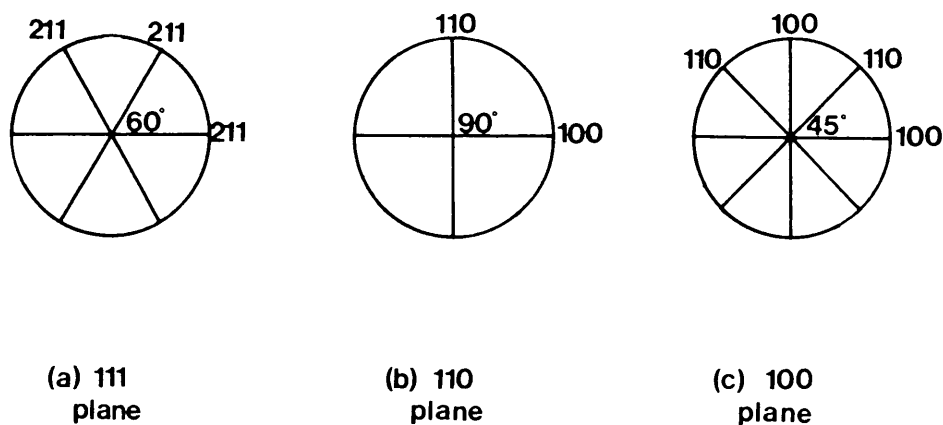
Figure 7.5   Stereographic projections obtained during crystal alignment procedures.

The standard stereographic projections for cubic crystals, which are illustrated in figures 7.6a, b and c, enabled the determination of the amount of rotation necessary in order to align the crystal along a different low index axial position that was also considered suitable for channeling damage analysis. The exact position of this new axis (in terms of α, θ and ϕ) could once more be determined by the tilting procedure.

6.   DATA AQUISITION AND ANALYSIS

RBS spectra were collected for each crystal both before and after Ar^+ implantation using both 1,5 and 1,8 (or 1,7) MeV alpha particle beams. The

Figure 7.6   (Ref. 25)   Standard projections for cubic crystals

(a)

(b)

(c)
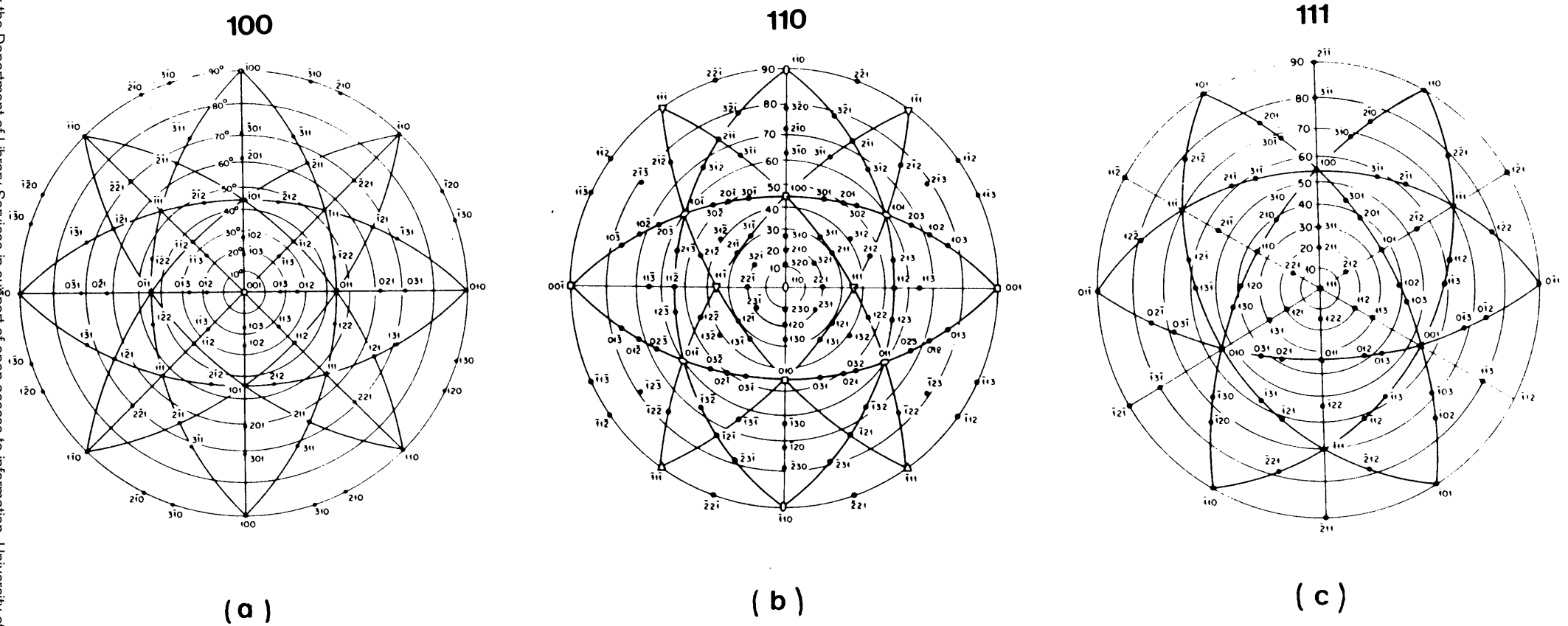
two different beam energies used provided an eventually larger data base from which to do statistical analysis, as well as enabling energy calibration of the MCA.

Two spectra were collected for each axis investigated: one in the "aligned" or channeling direction and the other at a "random setting", at which the axis was tilted 5 degrees away from the aligned orientation (along either α or θ) whilst rotating around ϕ during the whole period of data aquisition.

The suitability of an undamaged crystal for subsequent implantation and damage analysis was determined by studying the following aspects of the aligned and random spectra for each axis investigated:

-   The RBS yield integrated over a certain amount of channels just below the surface peak of the aligned spectrum was compared to the yield from the same channels of the random spectrum. Ideally the normalized minimum yield had to be in the order of 5% before the crystal was accepted for implantation, although minimum yields of up to 10% were considered adequate in some instances.

-   An aligned spectrum maintaining a very low RBS yield throughout (indicating a good crystal ordering up to great depths) was considered ideal for further damage analysis.

After implantation each crystal was once again subjected to channeling analysis; both aligned and random spectra being collected along each previously investigated channeling direction. All spectra were read

into the ACER computer connected to the multichannel analyzer from where spectrum analysis could be done. The Turbo Basic programme NORMSPEC was written and was used to divide the yield in each channel in an aligned spectrum with the yield in the corresponding random spectrum, thereby enabling a "normalized spectrum" to be displayed which facilitated the determination of the channel position of the typical "knee" indicating the extent of the radiation damage. In most cases the programme SPECFIT4 was used to superimpose a least squares fit (using a choice of polynomials) to a predetermined number of data points on the normalized spectrum, elucidating the knee position even further.

The energy loss factor [S] was determined from equation 1.20, using the surface approximation:

$$[S] \; = \; \frac{1}{\cos \theta_2} \left.\frac{dE}{dx}\right|_{KE_0} \; + \; \frac{K}{\cos \theta_1} \left.\frac{dE}{dx}\right|_{E_0} \qquad\qquad 1.20$$

which had been rewritten to incorporate the goniometer angles describing the position of the axis under consideration relative to the incident beam:

$$[S] \; = \; \frac{1}{\cos (\alpha - \theta) \, \cos \theta} \left.\frac{dE}{dx}\right|_{KE_0} \; + \; \frac{K}{\cos \alpha \, \cos \theta} \left.\frac{dE}{dx}\right|_{E_0} \qquad\qquad 7.1$$

where α and θ are the goniometer angles determined during crystal alignment procedures and $\beta = 180° - 165° = 15°$.

K, the kinematic factor, was determined using equation 1.5. The stopping powers $\left.\frac{dE}{dx}\right|_{KE_0}$ and $\left.\frac{dE}{dx}\right|_{E_0}$ were calculated by fitting the five

appropriate Ziegler coefficients to equation 2.12a, b and c and multi-plying the stopping cross sections thus obtained by the atomic density of the target material.

A factor δN (in units channels per 1000 Å) was then obtained by calculating the ratio of 1000 [S] and δE. The number of channels between the channel at the "knee" of the aligned damage spectrum and the channel corresponding to the yield halfway between the minimum and maximum positions of the leading edge of the random spectrum (indicating the surface position) were then counted and could be directly converted to a depth scale through the factor δN. Thus R_D, the experimental damage range, was determined.

CHAPTER 8

EXPERIMENTAL RESULTS AND DISCUSSION

1. SAMPLE IMPLANTATION

10° off–axis 150 keV Ar^{+} implantation was done in three nickel, three copper, two α–iron and four platinum single crystals. The temperatures, fluences and dosage rates are listed in Table 8.1

TABLE 8.1

Metal	Temperature (K)	Fluence (Ar^{+} cm^{-2})	Rate (Ar^{+} $cm^{-2}s^{-1}$)
Ni	77	5×10^{15}	$1,5 \times 10^{13}$
	300	5×10^{15}	$1,2 \times 10^{13}$
	523	2×10^{16}	$1,6 \times 10^{13}$
Cu	77	5×10^{15}	$4,8 \times 10^{12}$
	423	2×10^{16}	$1,6 \times 10^{13}$
	523	2×10^{16}	$1,6 \times 10^{13}$
Fe	77	5×10^{15}	$4,0 \times 10^{12}$
	300	5×10^{15}	$3,8 \times 10^{12}$
Pt	77	2×10^{16}	$1,6 \times 10^{13}$
	300	3×10^{16}	–
	423	2×10^{16}	$1,6 \times 10^{13}$
	573	2×10^{16}	$1,6 \times 10^{13}$

All samples were implanted with a similar Ar^{+} ion energy due to the fact that radiation damage ranges have been found to increase more or less linearly with increase in implantation energy.[63,64,65,67] Although the fluences

and dose rates vary slightly in Table 8.1, these fluctuations are not expected to influence radiation damage ranges significantly. Friedland et al.[64] did not find any significant dependence of damage range (in fcc Cu) on ion dosage, while Lindgreen et al.[50] found only a small dosage dependence in Cu (Linker et al.[68], however found both the damage *levels* and *ranges* to increase with increasing dosage for implantation of 150 keV Ga$^+$ in bcc vanadium.) As far as dosage *rates* are concerned, Lindgreen[58] found only a weak implantation tempo dependence of the deep damage range in Cu.

2. ENERGY CALIBRATION

The δE values obtained for each set of 1,5 MeV and 1,8 (or 1,7) MeV damage spectra are listed in Tables 8.4 (a), (b), (c) and (d). An example of the determination of δE for the <211> channel of the platinum sample implanted at 423 K follows.

For θ = 165° K_{Pt} = 0,9225

$$K_{Pt} \times 1500 = 1383,8 \text{ keV}$$
$$K_{Pt} \times 1800 = 1660,5 \text{ keV}$$
$$\text{Difference} = 276,7 \text{ keV}$$

Channel number corresponding to $K_{Pt}E_{1,5}$ = 369

Channel number corresponding to $K_{Pt}E_{1,8}$ = 447

$$\text{Difference} = 78 \text{ channels}$$

Therefore $\delta E = \dfrac{276,7}{78}$ = 3,548 keV/channel

TABLE 8.2

Pre–implantation experimental minimum yields (χ_{exp}) compared to the theoretical minimum yields (χ_{th}) for E = 1,5 MeV

⟨hkl⟩	Fe		Ni		Cu		Pt	
	χ_{th}	χ_{exp}	χ_{th}	χ_{exp}	χ_{th}	χ_{exp}	χ_{th}	χ_{exp}
⟨110⟩	0,032	0,04	0,019	0,06	0,029	0,04	0,017	0,02
⟨111⟩	0,019	0,02	0,049	0,25	0,074	0,12	0,045	0,11
⟨100⟩	0,022	–	0,027	0,04	0,042	0,05	0,024	–
⟨211⟩	0,052	0,07	0,064	0,09	0,097	0,04	0,062	0,05

3. THE DETERMINATION OF DAMAGE RANGES FROM BACKSCATTERING SPECTRA

Examples of typical aligned and random spectra obtained in this study are illustrated in figures 8.1(a) and (b). The specific example is that of the nickel single crystal implanted at 77 K and inspected along the ⟨100⟩ axis by means of a 1,5 MeV alpha particle beam before and after Ar^+ implantation. (**Note:** Due to a problem with the MCA, Ni and Cu spectra displayed a faulty dechanneling yield above the KE_o edge of each spectrum. This problem was eventually resolved, and did not occur in Fe and Pt damage spectra.)

The difference between the dechanneling yield in a channeling direction as opposed to the yield in a random direction can be observed for the un-damaged sample when comparing the spectra in figure 8.1(a). The two criteria for good channeling, namely a low normalized minimum yield (5,4%) in the surface region and the maintenance of a low yield throughout the spectrum can clearly be observed. (Table 8.2 lists the pre–implantation normalized minimum yields obtained experimentally for 1,5 MeV alpha parti-

Figure 8.1 (a) Undamaged and (b) damaged dechanneling spectra of nickel implanted at 77K and inspected along the (100) axis with a 1,5 MeV alpha particle beam
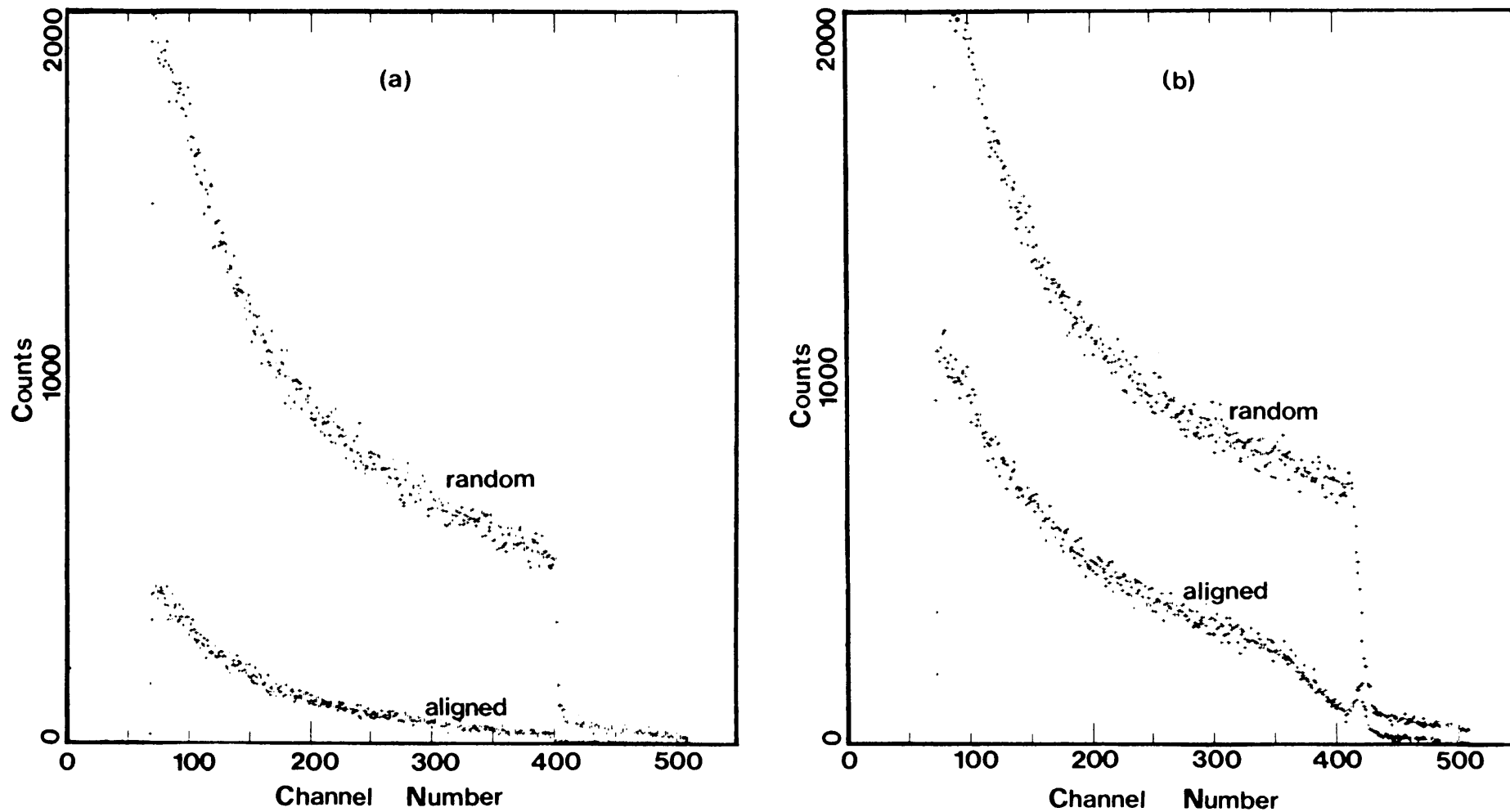
cles backscattered from the surface regions of all crystals investigated. These values are compared with theoretical minimum yields calculated from equation 3.21.)

A clearly enhanced dechanneling rate was observed in the aligned spectra of all the metal samples after Ar^+ implantation. This is illustrated for nickel in section (b) of figure 8.1. Beyond the enhanced surface yield the dechanneling yield progressively increases towards the typical "knee" which provides an indication of the range of the deep radiation damage incurred. Such knees were observed at varying depths in all damage spectra obtained for all metals investigated.
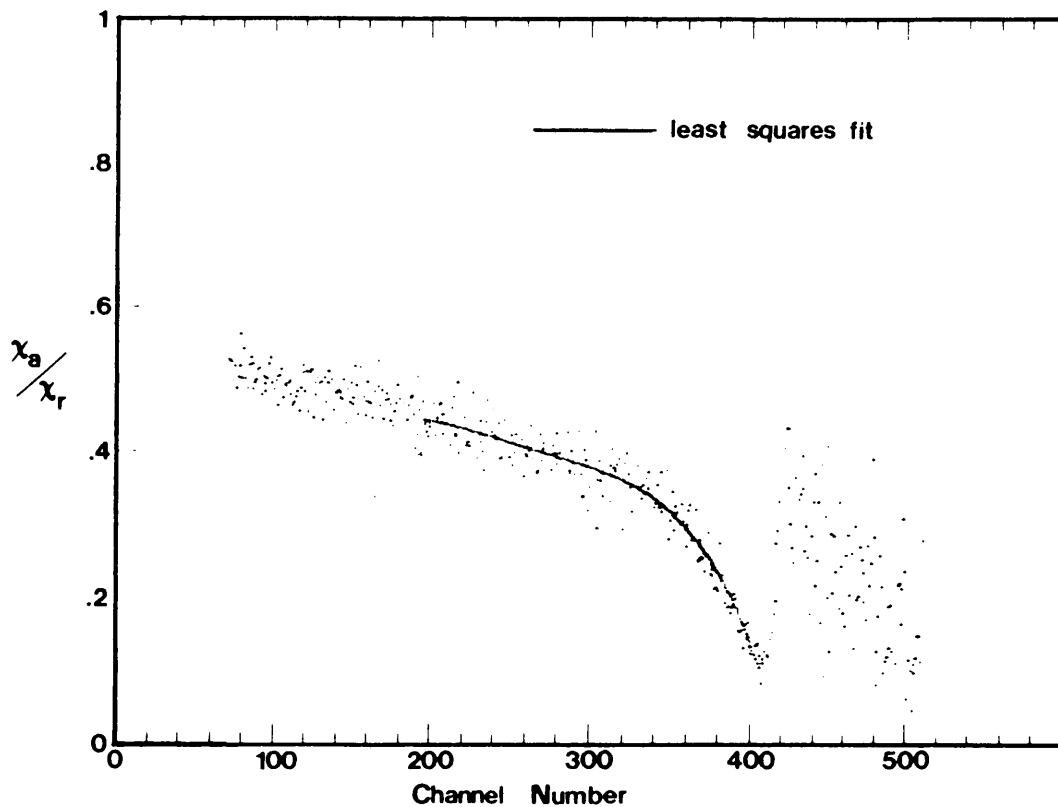
Figure 8.2   The normalized nickel 77 K spectrum.

Figure 8.2 shows how the position of the "knee" attains better definition after the normalization procedure, in which the yield at each point in the

aligned spectrum is divided by the corresponding value in the random spectrum. A least squares fit (using in this instance a 4th order polynomial) was superimposed on channel numbers 196 to 406. The channels between the "knee" and the random edge of the spectrum numbered 59.

The calibration factor, $\delta E = 2{,}592$ keV/channel was calculated for this instance. (The distance between the "knee" and the random edge in energy units is then $\Delta E = 2{,}592 \times 59 = 153$ keV.)

He stopping powers were obtained by substitution of the five Ziegler coefficients for nickel (refer to Table 8.3) into equations 2.12a, b and c:

TABLE 8.3
Ziegler coefficients for low energy (<10 MeV) He stopping

Element	A_1	A_2	A_3	A_4	A_5
Fe	5,013	0,4707	85,58	16,55	3,211
Ni	4,652	0,4571	80,73	22	4,952
Cu	3,114	0,5236	76,67	7,62	6,385
Pt	4,68	0,5247	244,7	2,749	0,8962

For $E = 1500$ keV:

$$S_{LOW} = A_1 E^{A_2}$$
$$= 4{,}652 \cdot (1500)^{0{,}4571} = \mathbf{131{,}65}$$

$$S_{HIGH} = \frac{A_3}{E/1000} \log \left(1 + \frac{A_4}{E/1000} + A_5 \frac{E}{1000}\right)$$

$$= \frac{80{,}73}{1{,}5} \log \left(1 + \frac{22}{1{,}5} + (4{,}952)(1{,}5)\right)$$

$$= \mathbf{168{,}97}$$

$$\varepsilon\left(E_{1,5}\right) = \frac{S_L \cdot S_H}{S_L + S_H}$$

$$= \frac{131,65 \cdot 168,97}{131,65 + 168,97}$$

$$= 73,97 \times 10^{-18} \text{ keV cm}^2 \text{ per atom}$$

The stopping power $\dfrac{dE}{dx}\bigg|_{1,5}$ can be obtained from this value of the 1,5 MeV stopping cross section $\varepsilon(E_{1,5})$ by multiplication with the atomic density of nickel:

$$\frac{dE}{dx}\bigg|_{1,5} = 73,97 \times 10^{-18} \cdot 9,126 \times 10^{22}$$

$$\equiv 6,750 \times 10^{-2} \text{ keV per Angstrom}$$

In order to use the surface approximation the stopping cross section for $E = K_{Ni} \cdot 1,5$ MeV was similarly determined (using $K_{Ni} = 0,7645$ as calculated from equation 1.5)

$$\varepsilon(K_{Ni}E_{1,5}) = 77,16 \times 10^{-18} \text{ keV cm}^2 \text{ per atom}$$

from whence the stopping power was obtained:

$$\frac{dE}{dx}\bigg|_{K_{Ni}E_{1,5}} = 77,16 \times 10^{-18} \times 9,126 \times 10^{22}$$

$$= 7,041 \times 10^{-2} \text{ keV per Angstrom}$$

The goniometer angles for the <100> axis of the Ni sample were:

$\alpha = -2,4$; $\theta = 2,3$ and $\phi = 1,0$. Substitution of calculated stopping powers,

the kinematic factor and using $\beta = 180° - 165° = 15°$ in the surface approximation (equation 7.1) yielded:

$$[S] = \frac{1}{\cos(\alpha-\beta)\cos\theta}\left.\frac{dE}{dx}\right|_{K_{Ni}E_{1,5}} + \frac{K_{Ni}}{\cos\alpha\cos\theta}\left.\frac{dE}{dx}\right|_{E_{1,5}}$$

$$= \left[\frac{1}{\cos(-2,4-15)\cos(2,3)} \cdot 6,750 \times 10^{-2}\right] + \left[\frac{1}{\cos(-2,4)\cos(2,3)} \cdot 7,04 \times 10^{-2}\right]$$

$$= 0,1255 \text{ keV per Angstrom}$$

The conversion factor δN was subsequently determined:

$$\delta N = \frac{1000 \cdot [S]}{\delta E} = \frac{125,5}{2,592} = 48,43 \text{ channels per 1000 Å}$$

The 59 channels between the "knee" and the surface positions on the damage spectrum therefore correspond to the damage range:

$$R_d = \frac{59}{48,43} \cdot 1000 = 1218 \text{ Angstrom}$$

Tables 8.4a, b, c, and d list the δE, ϵ, $[\epsilon]$, $[S]$, δN and R_d values obtained in the various crystal directions investigated in all four metals after implantation at various temperatures. Calculated R_d values can be expected to be slightly underestimated due to the fact that the Ziegler coefficients used for the determination of stopping powers do not take into account the reduced stopping of He in channeling directions.

The average R_d value, $<R_d>$, was calculated for each implantation temperature in all four metals by averaging over all the experimental ranges

TABLE 8.4

(a) Iron: K = 0,7540   N = 8,50 × 10^{22} atoms/cm^3

Implant-ation tempera-ture (K)	<hkl>	Goniometer angles a	θ	φ	energy (MeV)	Integrated beam current (× 10^{-6} C)	δE (keV) per channel	Ch. no. of random edge No. 1	Ch. no. of "knee" No. 2	No.1-No.2	ε(E_0) (× 10^{-18} keV cm^2 per atom)	ε(KE_0) (× 10^{-18} keV cm^2 per atom)	Stopping cross section factor [ε] (× 10^{-18} keV cm^2 per atom)	Energy loss factor [S] (keV per Ångstrom)	δN (channels) per 1000 Å	ΔE (keV)	R_d Experimental damage depth (Ångstrom)	Standard deviation in energy and depth due to energy straggling and limited system resolution Ω_s (keV)	Ω_{TOT} (keV)	δx (Å)	Ω_r (keV)
	<111>	0,2	-0,3	0,0	1,5	3,6	2,875			57	79,53	85,18	147,8	0,1256	43,69	164	800	5,37	14,1	112	
	<211>	19,5	2,4	0,0	1,5	3,6	2,875			37	79,53	85,18	148,8	0,1266	44,02	106	830	5,47	14,1	111	
	<110>	-34,6	-5,8	0,0	1,5	3,6	2,875			44	79,53	85,18	204,9	0,1742	60,58	127	720	5,10	14,0	80	
77	<110>	-34,6	-5,8	0,0	1,8	5,4	2,875			39	74,44	81.90	195,2	0,1659	57,70	112	680	4,95	13,9	84	13
	<211>	19,5	2,4	0,0	1,8	5,4	2,875			35	74,44	81.90	141,5	0,1203	41,85	101	830	5,47	14,1	117	
	<111>	0,2	-0,3	0,0	1,8	5,4	2,875			27	74,44	81.90	140,6	0,1195	41,56	78	640	4,80	13,9	116	
	<111>	-0,8	0,5	0,0	1,5	3,6	2,916			44	79,53	85,18	148,2	0,1260	43,20	128	1020	6,07	14,3	114	
	<211>	18,5	0,8	5,0	1,5	3,6	2,916			42	79,53	85,18	148,2	0,1260	43,23	122	970	5,91	14,3	113	
	<110>	-36,2	-0,1	5,0	1,5	3,6	2,916			61	79,53	85,18	209,9	0,1784	61,16	178	1000	6,01	14,3	80	
300	<110>	-36,2	-0,1	5,0	1,8	5,4	2,916			58	74,44	81.90	199,9	0,1699	58,26	169	990	5,98	14,3	84	13
	<211>	18,5	0,8	5,0	1,8	5,4	2,916			43	74,44	81.90	140,9	0,1198	41,09	125	1040	6,12	14,4	120	
	<111>	-0,8	0,5	0,0	1,8	5,4	2,916			37	74,44	81.90	140,9	0,1198	41,09	108	900	5,70	14,2	118	

TABLE 8.4

(b) Nickel: $K = 0,7645$ $N = 9,126 \times 10^{22}$ atoms/cm^3

Implantation tempera-ture (K)	<hkl>	Goniometer angles θ	φ	ϕ	a energy (MeV)	Integrated beam current (× 10^{-6}C)	δE (keV) per channel	Ch. no. of random edge No. 1	Ch. no. of "knee" No. 2	No.1-No.2	ε(E₀) (× 10^{-18} keV cm^2 per atom)	ε(ΔE₀) (× 10^{-18} keV cm^2 per atom)	Stopping cross section factor [ε] (× 10^{-18} keV cm^2 per atom)	Energy loss factor [S] (keV per Angstrom)	δN (channels) per 1000 Å	ΔE (keV)	R$_d$ Experimental damage depth (Angstrom)	Ω$_s$ (keV)	Ω$_{TOT}$ (keV)	δx (Å)	Ω$_r$ (keV)
77	<100>	-2,4	2,3	1,0	1,5	3,0	2,592	420	361	59	73,97	77,16	137,5	0,1255	48,43	153	1218	7,16	15,7	125	
	<100>	-2,4	2,3	1,0	1,7	4,5	2,592	479	422	57	71,66	76,00	134,6	0,1228	47,38	148	1203	7,11	15,7	128	
	<310>	15,5	-1,1	46,5	1,7	4,5	2,683	478	424	54	71,66	76,00	132,9	0,1213	45,20	145	1195	7,09	15,7	129	
	<310>	15,5	-1,1	46,5	1,5	3,0	2,683	421	372	49	73,97	77,16	135,9	0,1240	46,21	132	1060	6,68	15,5	125	14
	<211>	39,9	-3,7	179,9	1,5	3,0	2,428	421	360	61	73,97	77,16	159,1	0,1452	59,81	148	1020	6,55	15,5	106	
	<211>	39,9	-3,7	179,9	1,7	4,5	2,428	484	421	63	71,66	76,00	155,5	0,1419	58,47	153	1077	6,74	15,5	109	
300	<110>	13,0	5,1	0,0	1,5	3,6	3,142			57	73,97	77,16	135,8	0,1239	39,44	179	1447	7,81	17,8	144	
	<211>	19,9	3,9	125,0	1,5	3,6	3,018			60	73,97	77,16	137,8	0,1258	41,70	181	1400	7,68	17,7	141	
	<111>	-21,0	0,2	342,0	1,5	3,6	2,979			58	73,97	77,16	155,9	0,1423	47,77	173	1219	7,17	17,5	123	16
	<111>	-21,0	0,2	342,0	1,8	5,4	2,979			54	70,46	77,28	150,8	0,1376	46,18	161	1173	7,03	17,5	127	
	<211>	19,9	3,9	125,0	1,8	5,4	3,018			47	70,46	77,28	133,1	0,1215	40,26	142	1173	7,03	17,5	144	
	<110>	13,0	5,1	0,0	1,8	5,4	3,142			50	70,46	77,28	131,2	0,1197	38,09	157	1324	7,47	17,7	148	
523	<100>	4,6	0,7	1,0	1,7	4,5	2,832	488	416	72	71,66	76,00	132,3	0,1207	42,61	204	1690	8,44	17,2	143	
	<211>	28,7	-0,1	127,1	1,7	4,5	2,781	489	425	64	71,66	76,00	140,7	0,1284	46,17	178	1386	7,64	16,8	131	
	<110>	49,9	2,6	37,0	1,7	4,5	2,592	491	416	75	71,66	76,00	178,0	0,1624	62,64	194	1197	7,10	16,6	102	15
	<110>	49,9	2,6	37,0	1,5	3,0	2,592	432	375	57	73,97	77,16	182,0	0,1661	64,11	148	899	6,12	16,2	98	
	<211>	28,7	-0,1	172,1	1,5	3,0	2,781	434	370	64	73,97	77,16	148,9	0,1313	47,11	178	1359	7,57	16,8	126	
	<100>	4,6	0,7	1,0	1,5	3,0	2,832	434	354	80	73,97	77,16	135,2	0,1234	43,56	227	1837	8,80	17,4	141	

TABLE 8.4

(c) Copper: $K = 0{,}7803$ $N = 8{,}45 \times 10^{22}$ atoms/cm^3

Implantation temperature (K)	$\langle hkl \rangle$	Goniometer angles θ	ϕ	ψ	energy (MeV)	Integrated beam current ($\times 10^{-6}$ C)	δE (keV) per channel	Ch. no. of random edge No. 1	Ch. no. of "knee" No. 2	No.1–No.2	$\epsilon(E_0)$ ($\times 10^{-18}$ keV cm^2 per atom)	$\epsilon(KE_0)$ ($\times 10^{-18}$ keV cm^2 per atom)	Stopping cross section factor $[\epsilon]$ ($\times 10^{-18}$ keV cm^2 per atom)	Energy loss factor $[S]$ (keV per Angstrom)	δN (channels) per 1000 Å	ΔE (keV)	R_d Experimental damage depth (Angstrom)	Ω_s (keV)	Ω_{TOT} (keV)	δx (Å)	Ω_r (keV)
77	$\langle100\rangle$	-1,5	-3,0	0,0	1,5	4,8	3,345			71	71,08	73,73	133,1	0,1125	33,62	238	2110	9,30	17,7	157	
	$\langle100\rangle$	-1,5	-3,0	0,0	1,8	7,2	3,345			68	68,23	71,93	129,0	0,1090	32,58	228	2080	9,24	17,6	162	
	$\langle211\rangle$	35,9	-3,3	53,5	1,5	4,8	3,345			59	71,08	73,73	148,2	0,1252	37,44	197	1570	8,02	17,0	136	
	$\langle211\rangle$	35,9	-3,3	53,5	1,8	7,2	3,345			60	68,23	71,93	143,6	0,1213	36,26	201	1660	8,25	17,1	141	15
423	$\langle111\rangle$	1,3	-2,7	1,0	1,5	3,0	2,559	437	357	80	71,08	73,73	132,1	0,1116	43,60	205	1835	8,68	17,3	155	
	$\langle211\rangle$	22,9	-2,3	61,0	1,5	3,0	2,518	436	334	102	71,08	73,73	135,3	0,1143	45,41	257	2246	9,60	17,8	156	
	$\langle110\rangle$	34,2	1,0	244,2	1,5	3,0	2,518	436	342	94	71,08	73,73	145,7	0,1231	48,91	237	1922	8,86	17,4	142	15
	$\langle110\rangle$	34,2	1,0	244,2	1,7	4,5	2,518	498	380	118	69,19	72,59	142,7	0,1206	47,90	297	2463	10,05	18,1	150	
	$\langle211\rangle$	22,9	-2,3	61.0	1,7	4,5	2,518	498	406	92	69,19	72,59	132,5	0,1120	44,48	232	2068	9,21	17,6	157	
	$\langle111\rangle$	1,3	-2,7	1,0	1,7	4,5	2,559	498	400	98	69,19	72,59	129,3	0,1093	42,72	251	2294	9,70	17,9	163	
523	$\langle111\rangle$	2,1	1,8	1,0	1,5	3,0	2,838	443	351	92	71,08	73,73	131,7	0,1113	39,22	261	2346	9,81	17,9	161	
	$\langle211\rangle$	20,5	-1,1	199,7	1,5	3,0	2,945	443	355	88	71,08	73,73	133,8	0,1131	38,40	259	2292	9,70	17,9	158	
	$\langle110\rangle$	34,6	3,7	80,1	1,5	3,0	2,559	436	352	84	71,08	73,73	146,5	0,1238	48,38	215	1736	8,44	17,2	139	15
	$\langle110\rangle$	34,6	3,7	80,1	1,7	4,5	2,559	497	412	85	69,19	72,59	143,6	0,1213	47,39	218	1794	8,58	16,3	142	
	$\langle211\rangle$	20,5	-1,1	199,7	1,7	4,5	2,945	496	400	96	69,19	72,59	131,1	0,1108	37,62	283	2552	10,23	18,2	164	
	$\langle111\rangle$	2,1	1,8	1,0	1,7	4,5	2,838	498	410	88	69,19	72,59	129,1	0,1091	38,43	250	2290	9,69	17,9	164	

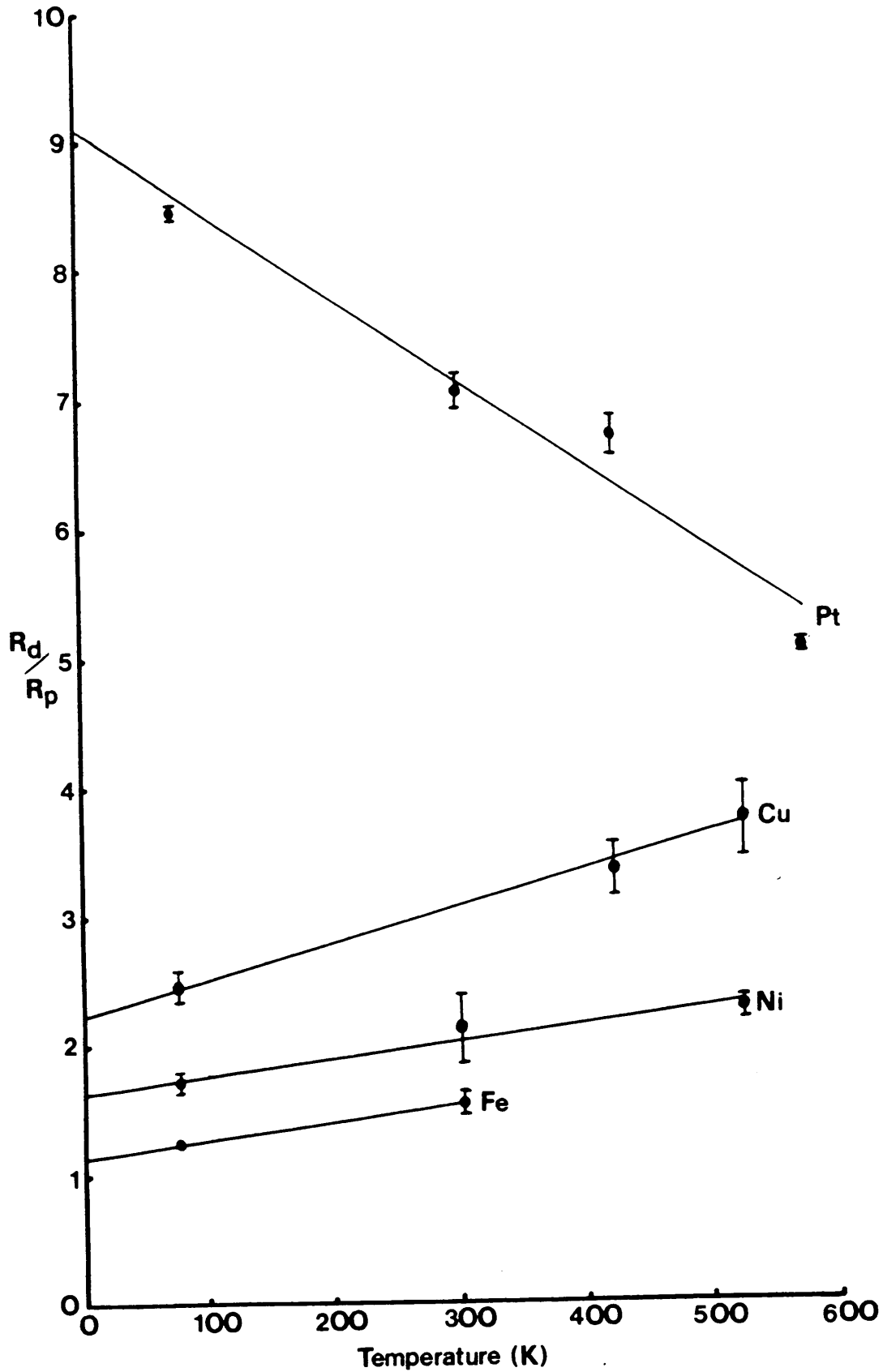Figure 8.4(b) Temperature depence of the relative damage ranges of Fe, Ni, Cu and Pt averaged over the 2̄11 direction

TABLE 8.4

(d) Platinum: K = 0,9225 N = 6,62 × 10^{22} atoms/cm^3

Implantation temperature (K)	⟨hkl⟩	Goniometer angles θ	φ	ψ	energy (MeV)	Integrated beam current (× 10^{-6}C)	δE (keV) per channel	Ch. no. of random edge No. 1	Ch. no. of "knee" No. 2	No.1–No.2	ε(E_0) (× 10^{-18} keV cm^2 per atom)	ε(KE_0) (× 10^{-18} keV cm^2 per atom)	Stopping cross section factor [ε] (× 10^{-18} keV cm^2 per atom)	Energy loss factor [S] V per (Angstrom)	δN (channels) per 1000 Å	ΔE (keV)	R_d Experimental damage depth (Angstrom)	Ω_s (keV)	Ω_{TOT} (keV)	δx (Å)	Ω_r (keV)
77	⟨111⟩	1,4	-0,6	1,0	1,8	5,4	3,460	477	353	124	106,9	109,5	212,1	0,1404	40,58	429,0	3066	17,4	31,3	223	
	⟨111⟩	1,4	-0,6	1,0	1,5	3,6	3,460	397	261	136	112,6	114,7	222,7	0,1474	42,61	470,6	3192	17,8	31,5	214	
	⟨211⟩	20,8	-3,3	46,0	1,8	5,4	3,595	474	337	137	106,9	109,5	214,5	0,1420	39,51	492,5	3455	18,5	31,9	225	
	⟨211⟩	20,8	-3,3	46,0	1,5	3,6	3,595	397	254	143	112,6	114,7	225,4	0,1492	41,49	514,1	3447	18,5	31,9	214	26
	⟨110⟩	36,3	-5,7	106,0	1,8	5,4	3,460	477	305	172	106,9	109,5	237,5	0,1572	45,42	595,1	3787	19,4	32,4	206	
	⟨110⟩	36,3	-5,7	106,0	1,5	3,6	3,460	397	215	182	112,6	114,7	249,2	0,1650	47,70	629,7	3816	19,5	32,5	197	
423	⟨111⟩	2,2	0,2	1,0	1,5	3,6	3,594	369	265	104	112,6	114,7	221,6	0,1467	40,80	374	2549	15,6	30,3	207	
	⟨111⟩	2,2	0,2	1,0	1,8	5,4	3,594	446	340	106	106,9	109,5	211,0	0,1397	38,86	381	2728	16,5	30,8	220	
	⟨211⟩	19,9	1,5	106,0	1,8	5,4	3,548	447	336	111	106,9	109,5	214,8	0,1422	40,09	394	2769	16,6	30,8	217	
	⟨211⟩	19,9	1,5	106,0	1,5	3,6	3,548	369	256	113	112,6	114,7	225,7	0,1494	42,10	401	2684	16,3	30,7	206	26
	⟨110⟩	37,0	2,0	46,0	1,8	5,4	3,594	446	313	133	106,9	109,5	241,7	0,1600	44,53	478	2987	17,2	31,2	195	
	⟨110⟩	37,0	2,0	46,0	1,5	3,6	3,594	369	231	138	112,6	114,7	253,9	0,1681	46,76	496	2951	17,1	31,1	185	
573	⟨111⟩	-1,6	0,6	1,0	1,8	5,4	3,691	445	359	86	106,9	109,5	214,0	0,1417	38,39	317,4	2240	14,9	30,0	212	
	⟨111⟩	-1,6	0,6	1,0	1,5	3,6	3,691	370	267	103	112,6	114,7	224,8	0,1488	40,31	380,2	2555	15,9	30,5	205	
	⟨211⟩	22,9	1,5	225,0	1,5	3,6	3,417	399	309	90	112,6	114,7	227,3	0,1505	44,04	307,5	2043	14,3	29,7	197	26
	⟨211⟩	22,9	1,5	225,0	1,8	5,4	3,417	480	394	86	106,9	109,5	216,5	0,1433	41,94	293,9	2050	14,3	30,0	207	
	⟨110⟩	34,1	-1,5	45,0	1,5	3,6	3,741	369	–	–	112,6	114,7	243,8	0,1614	43,14	–	–	–	–	–	
	⟨110⟩	34,1	-1,5	45,0	1,8	5,4	3,741	443	337	106	106,9	109,5	232,2	0,1537	41,09	396,5	2580	16,0	30,5	199	
300	⟨111⟩				2,0						103,3	106,1					2765				
	⟨111⟩				1,5						112,6	114,7					2865				
	⟨110⟩				2,5						95,5	98,3					2686				
	⟨211⟩				2,0						103,3	106,1					2856				
	⟨211⟩				2,5						95,5	98,3					2807				
	⟨211⟩				1,5						112,6	114,7					2950				
	⟨211⟩				2,0						103,3	106,1					2874				
423 then annealed at 600 K	⟨111⟩	2,2	0,2	1,0	1,5	3,6	3,741	370	255	115	112,6	114,7	222,2	0,1471	39,33	430,2	2924	17,1	31,1	211	
	⟨111⟩	2,2	0,2	1,0	1,8	5,4	3,741	444	342	102	106,9	109,5	211,6	0,1401	37,46	381,6	2723	16,5	30,8	220	
	⟨211⟩	19,9	1,5	106,0	1,8	5,4	3,691	445	320	125	106,9	109,5	213,7	0,1415	38,35	461,4	3259	18,0	31,6	223	
	⟨211⟩	19,9	1,5	106,0	1,5	3,6	3,691	370	243	127	112,6	114,7	221,5	0,1466	40,27	468,8	3154	17,7	31,5	212	26
	⟨110⟩	37,0	2,0	46,0	1,8	5,4	3,741	444	330	114	106,9	109,5	238,4	0,1578	42,18	426,5	2703	16,4	30,7	195	
	⟨110⟩	37,0	2,0	46,0	1,5	3,6	3,741	370	–	–	112,6	114,7	250,3	0,1657	44,30	–	–	–	–	–	

TABLE 8.5

The temperature dependence of damage ranges averaged over all the crystal directions investigated

Metal	Projected Ranges (Å) at various		Experimental damage ranges (Å) at various temperatures (K)					$\langle \frac{R_d}{R_p} \rangle$ at various temperatures (K)									
								PRAL					TRIM				
	PRAL	TRIM	77	300	423	523	573	77	300	425	523	573	77	300	425	523	573
Fe (bcc)	656	673	750 ± 80	987 ± 49				1,14 ± 0,12	1,55 ± 0.07				1,118 ± 0,12	1,47 ± 0,07			
Ni (fcc)	602	610	1129 ± 86	1289 ±119		1393 ± 340		1,86 ± 0,14	2,14 ± 0,20		2,31 ± 0,56		1,85 ± 0,14	2,11 ± 0,20		2,28 ± 0,56	
Cu (fcc)	649	675	1855 ±280		2138 ± 239	2168 ± 327		2,86 ± 0,43		3,29 ± 0,36	3,34 ± 0,50		2,75 ± 0,41		3,17 ± 0,35	3,21 ± 0,48	
Pt (fcc)	407	487	3459 ± 306	2828 ± 85	2778 ± 166 After annealing 2953 ± 250		2294 ± 2,62	8,50 ± 0,75	6,95 ± 0,21	6,83 ± 0,41 After annealing 7,26 ± 0,61		5,64 ± 0,64	7,10 ± 0,63	5,81 ± 0,17	5,70 ± 0,34 After annealing 6,06 ± 0,5		4,7 ± 0,54

Figure 8.3   Temperature depence of the relative damage ranges of Fe, Ni, Cu and Pt averaged over all the (hkl) directions investigated
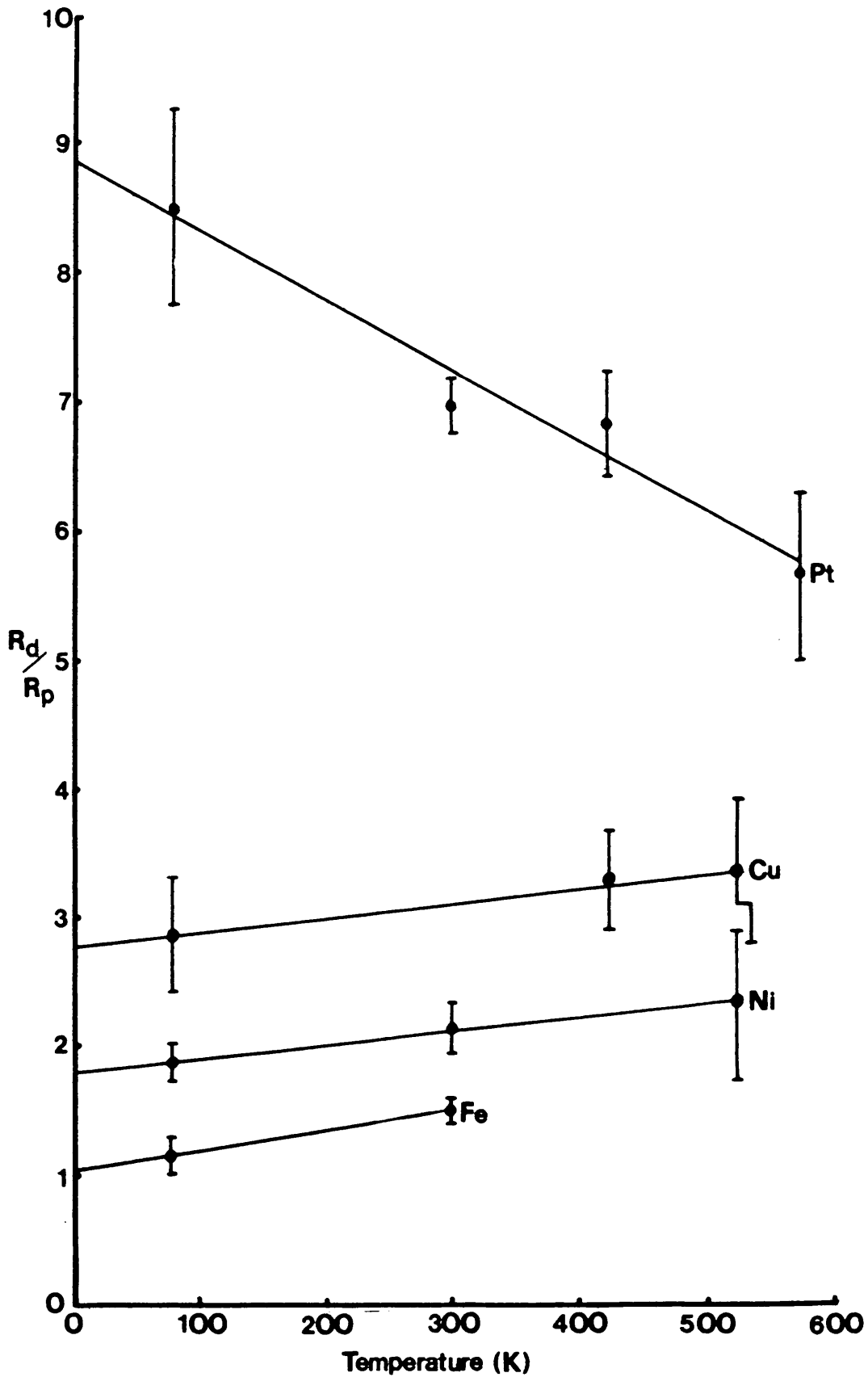
Figure 8.4(a) Temperature depence of the relative damage ranges of Fe, Ni, Cu and Pt averaged over the 110 direction
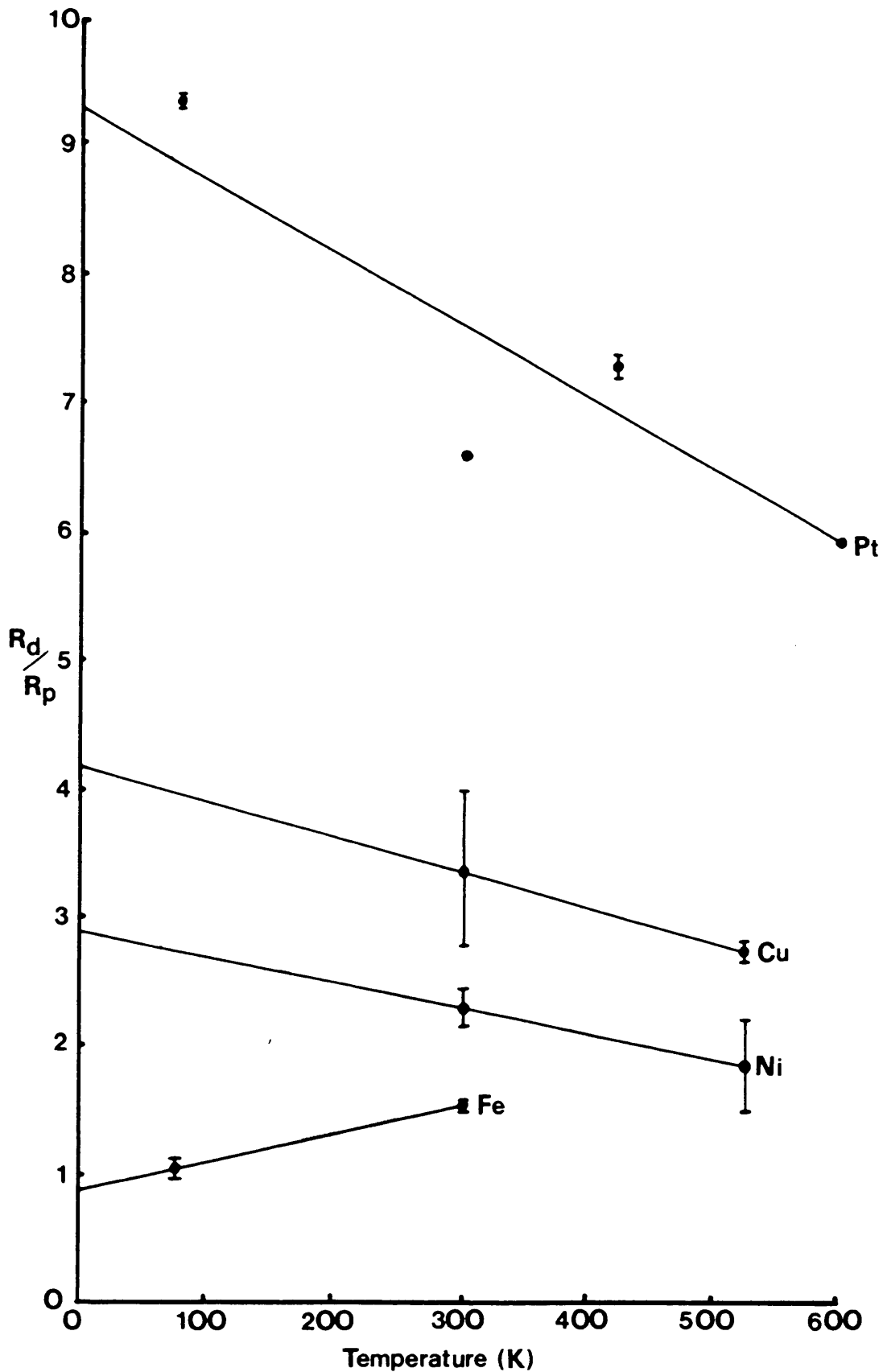
Figure 8.4(c) Temperature depence of the relative damage ranges of Fe, Ni, Cu and Pt averaged over the 111 direction
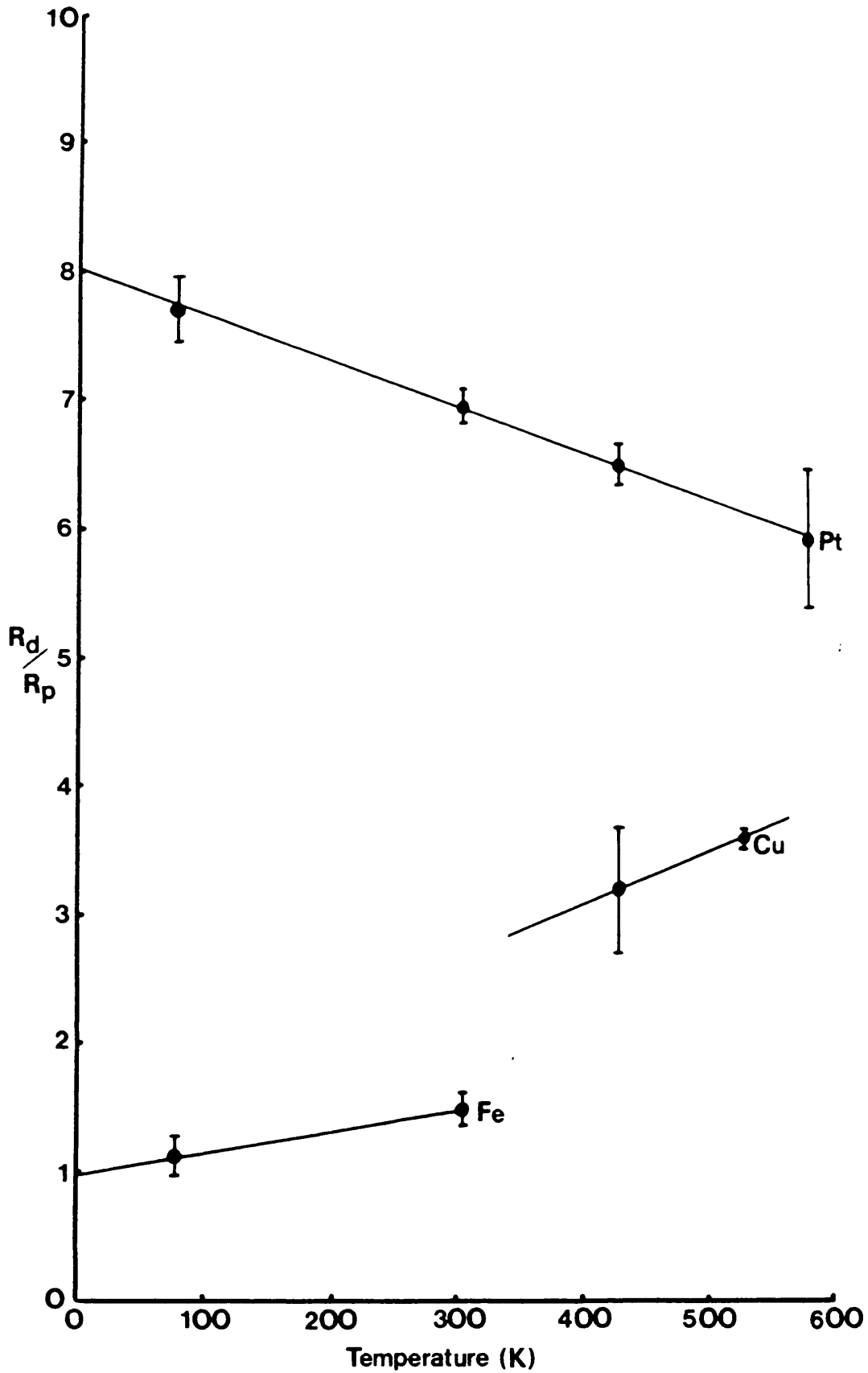
obtained in the various <hkl> directions investigated. These average damage ranges, listed in Table 8.5, generally show a mean square deviation ranging from 50 − 300Å.

Table 8.5 also lists the ratio of average experimental damage range $<R_d>$, to the projected range R_p, (as obtained from both the PRAL and TRIM86 programmes) for each metal implanted at the various temperatures. The relative damage ranges obtained from the PRAL data are plotted against implantation temperature in Figure 8.3. Error bars indicate the spread in experimental data. The $<\frac{R_d}{R_p}>_{PRAL}$ values for each metal have been con- nected by a straight line least squares fit. Looking only at the mean values obtained there seems to be a moderate increase in R_d with increasing tempe- rature for iron, nickel and copper, while platinum shows a gradual decrease in relative damage range with temperature. The range data obtained by avera- ging over all <hkl> directions for the iron and platinum samples gives a reasonably accurate description of what happens to the respective damage ranges with increase in implantation temperature. The average copper and nickel data, however, display very large standard deviations which lead to overlapping of the error bars in figure 8.3. It is therefore not possible to discern either a decrease or an increase in damage range with temperature for the copper and nickel samples. The accuracy of the observed decrease in $\frac{R_d}{R_p}$ for platinum, and the increase in $\frac{R_d}{R_p}$ (though slight) for iron is further displayed in figures 8.4(a), (b) and (c), where in each case the relative damage ranges along a specific investigated <hkl> direction is plotted against temperature. In all <hkl> directions plotted, i.e. <110>, <211> and <111>, a general decrease is discerned for platinum, while the reverse trend

occurs for iron. In the cases of nickel and copper, however, the relative damage ranges along the <110> direction display a slight decrease with increase in temperature, while the $\frac{R_d}{R_p}$ values increase with temperature along the <211> and <111> directions investigated. (Insufficient data points were available for the <111> direction in Ni, therefore the absence of Ni data in the <111> graph.) The reasons for the increase in damage range with temperature for Fe (as well as possibly for Ni and Cu if error bars are omitted in figure 8.3) as well as the decrease observed for platinum are discussed at a later stage. The following section investigates various factors which could contribute to the large standard deviations obtained in many of the average damage range values.

4. INVESTIGATION OF THE FACTORS CAUSING LARGE STANDARD DEVIATIONS IN DAMAGE RANGES

A gradual increase in radiation damage depth with temperature has been observed by various authors mentioned in Chapter 6 section 1[49,50,58,63,65] (although a reverse trend has also been observed[63]). This investigation was launched with the expectation of finding a similarly increasing trend. The large fluctuations in R_d values (especially in the data obtained from copper and nickel single crystals) make it difficult to come to any definite conclusions as regards the functional dependence of Ni and Cu damage ranges on temperature. It is considered appropriate at this stage to investigate some factors which could all contribute, to a lesser or greater extent, towards the spread in R_d values that was observed.

(i) Variation of damage ranges in different <hkl> directions

The fact that the average R_d value is calculated with range

values obtained from *various* <hkl> directions might explain the large standard deviations in damage ranges. R_d values in differing <hkl> directions might differ due to various possible factors:

(a)   Channeled ion stopping powers have been found to differ in varying <hkl> directions (as was discussed in Chapter 3 section 9). If the real damage lies at a depth X below the target surface an analyzing He ion channeled in, say, the very "open" <110> direction in an fcc crystal would have lost less energy by the time it was backscattered at X than would be the case for an ion channeled in the less open <111> direction. The He ion initially incident in the more open direction would therefore be recorded at a higher channel number in the MCA spectrum than would the ion incident in a less open direction; the distance between the surface edge and the "knee" channel would therefore be smaller and, if equal (Ziegler) stopping powers are used in the determination of R_d (as was done in this study), the R_d value for the alpha particle channeled along the <110> direction would be smaller than the R_d value obtained for He channeling along a <111> direction. In this section the possible occurrence of such a trend is investigated.

The average $< \frac{R_d}{R_p} >_{PRAL}$ values in various crystal directions were obtained from Tables 8.4 a,b,c and d. These values are listed along with their experimental standard deviations in Table 8.6. They are also plotted (with error bars) in figure 8.5. Furthermore the theoretical channeling half angles for 1,5 and 1,8 (or 1,7) MeV He in various <hkl> directions of the various metals implanted at

TABLE 8.6

$$< \frac{R_d}{R_p} >_{PRAL}$$ values in various crystal directions

$\langle hlk \rangle$	$\langle \frac{R_d}{R_p} \rangle$ for Fe		$\langle \frac{R_d}{R_p} \rangle$ for Ni			$\langle \frac{R_d}{R_p} \rangle$ for Cu			$\langle \frac{R_d}{R_p} \rangle$ for Pt			
	77 K	300 K	77 K	300 K	523 K	77 K	423 K	523 K	77 K	300 K	423 K	573 K
$\langle 110 \rangle$	1,07 ± 0,04	1,52 ± 0,01	—	2,30 ± 0,14	1,73 ± 0,36	—	3,38 ± 0,59	2,72 ± 0,06	9,34 ± 0,05	6,60	7,29 ± 0,06 After annealing at 600 K: 6,64	6,34
$\langle 111 \rangle$	1,10 ± 0,17	1,46 ± 0,13	—	1,99 ± 0,05	—	—	3,18 ± 0,5	3,57 ± 0,06	7,68 ± 0,24	6,91 ± 0,16	6,48 ± 0,16 After annealing at 600 K: 6,94	5,89 ± 0,55
$\langle 100 \rangle$	—	—	2,01 ± 0,02	—	2,93 ± 0,17	3,23 ± 0,03	—	—	—	—	—	—
$\langle 211 \rangle$	1,27 ± 0,00	1,53 ± 0,08	1,74 ± 0,07	2,14 ± 0,27	2,28 ± 0,03	2,49 ± 0,10	3,32 ± 0,19	3,73 ± 0,28	8,48 ± 0,01	7,06 ± 0,14	6,70 ± 0,15 After annealing at 600 K: 7,88	5,03 ± 0,01
$\langle 310 \rangle$	—	—	1,87 ± 0,16	—	—	—	—	—	—	—	—	—

various temperatures were calculated and are listed in Table 8.7. These half angles were determined using an equation similar to equation 3.16. (Debye temperatures $\left(\theta \; (^{\circ}K)\right)$ with which to calculate the thermal vibration amplitudes (u_1) at various temperatures were obtained from Mayer and Rimini[25]. The adimensional string potential was calculated by way of a modified Bessel function.) The various <hkl> directions listed in order of decreasing half angle may be obtained from these calculations (for all temperatures and energies investigated):

for the fcc crystals: 110   100   211   013   111

for the bcc crystals: 111   100   110   211

This order corresponds exactly to the ordering of increasing spacing between atoms along the various axes as well as to the ordering of "channeling transparency" values listed in Table 4.2. The relative size of the half angles may therefore be used as an indication of how well He ions are channeled along the various <hkl> directions: the larger the value of $\psi_{\frac{1}{2}}$ the deeper the ion is assumed to penetrate and the smaller the energy loss of an ion channeled along the specific axis. If stopping powers varied considerably along the various <hkl> directions used in this study, one would expect the $< \dfrac{R_d}{R_p} >$ values for the different <hkl> directions plotted in figure 8.5 to increase with decrease in half angle. However, due in part to the large error bars in figure 8.5, no such tendency can be discerned and therefore it may be accepted that He stopping powers up to the depths investigated in this study do no vary significantly in the various low index <hkl> directions employed. The large standard deviations in R_d are therefore not caused by greatly differing He stopping powers along the various <hkl> directions.

(b)   As discussed in Chapters 3 and 4, the facility of defect propagation decreases with increasing atomic spacing along a crystal axis in the following order for <hkl> directions investigated in this study:

for fcc crystals: 110 100 211 013 111

for bcc crystals: 111 100 110 211

The depth of the final damage (measured along a path normal to the target surface) after such defect propagation would however also depend on the angle which the specific <hkl> direction (along which propagation took place) makes with the surface normal.   The fact that damage is propagated with more ease along some of the <hkl> directions than others should (due to the analysis method employed) not cause the experimental R_d values obtained in this study to differ from one investigated crystallographic direction to another.   The reason for this may be discussed with reference to figure 8.6:
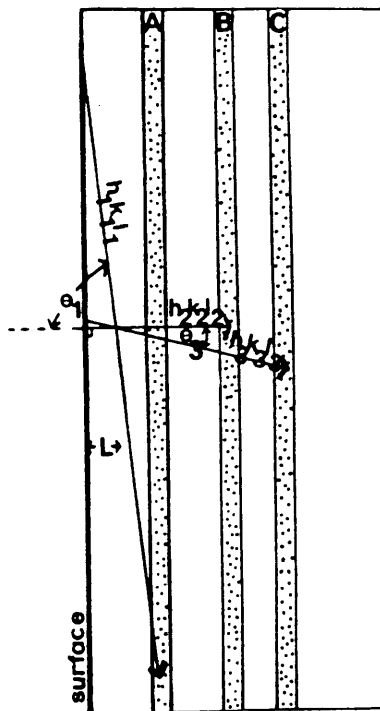
Figure 8.6   *Final damage may be propagated to various depths A,B and C depending on the ease with which a specific <hkl> direction is able to propagate defects, as well as on the angle which the <hkl> direction makes with the surface normal*

In this illustration, direction $<h_1k_1l_1>$ makes angle θ_1 with the surface normal, while direction $<h_3k_3l_3>$ lies $\theta_3(<\theta_1)$ degrees away from the normal vector. Direction $<h_2k_2l_2>$ lies normal to the surface. Furthermore, defects (initially lying in this instance at a depth L below the surface) are propagated two times more easily along the $<h_1k_1l_1>$ direction than along the $<h_3k_3l_3>$ direction and three times more easily than along the $<h_2k_2l_2>$ direction. For this specific example, defect propagation along $<h_3k_3l_3>$ results in final damage in a region C, relatively far below the crystal surface. Defect propagation along $<h_2k_2l_2>$ causes damage in the shallower region B, while final damage due to defects propagating along $<h_1k_1l_1>$ lies in the shallowest region A. When using alpha particle channeling for the damage investigation along any one of these three directions, *all* three damage ranges A, B and C will be discerned, irrespective of the channel along which the investigation is being done (equal He stopping powers are assumed). The same maximum R_d value (at depth C) will therefore be obtained along all directions investigated. It is therefore not possible, by way of a dechanneling analysis, to determine whether defect propagation specifically along, say, $<h_3k_3l_3>$ actually caused the damage at C.

Figure 8.6 further serves to illustrate the fact that a crystallographic direction, along which defects are very easily propagated, does not necessarily cause such damage to lie further below the target surface than would be the case for propagation along $<hkl>$ directions offering more resistance: Although defects are propagated, in this example, with the most ease along the

$<h_1k_1l_1>$ direction, the final damage (at A) lies the shallowest due to the large angle between the surface normal and the $<h_1k_1l_1>$ direction.

The only way in which the differing propagation facilities and the differing angles made by various $<hkl>$ directions may have an effect on the large standard deviations in R_d obtained in this study, lies in the fact that damage propagated to various depths below the target surface (e.g. A,B and C) will cause the damage "knee" in the dechanneling spectrum to become increasingly ill–defined ("spread out") the greater the distance of separation between these regions of damage. (Separate distinct damage knees for regions A, B and C would not be discernible due to the relatively small separations involved.) An ill–defined knee makes it very difficult to choose the best two lines, the intersection of which indicates R_d. The experimental error is therefore enlarged.

Note: The very fact that rather spread–out knees were obtained in this study, could be used as possible evidence that a stress field propagation of defects (which is directionally dependent) is the mechanism of deep radiation damage production.

(ii) **Inherent spread in real damage range due to energy straggling of Ar^+ ions during implantation**

As discussed in the previous section, "spread out" damage knees may be caused by differences in the ability of various $<hkl>$ directions to propagate defects. Another cause of bad knee definition could be energy straggling of Ar^+ ions during implantation:

During the Ar^+ implantation process the energy profile of the initially mono—energetic incident beam progressively broadens with increasing penetration into the target material. One would therefore expect the Ar^+ ions to come to rest within a finite volume of the material, the size (or dimensions) of which would depend on the amount of energy straggling which has occurred. The TRIM86 pro—gramme predicts the following half widths of Ar^+ ions in the final range profiles: 284 Å in Fe, 272 Å in Ni, 299 Å in Cu and 262 Å in Pt. If radiation damage had been found to occur at depths corresponding to the range of implanted ions, one would expect the damage "knee" in the corresponding RBS spectrum not to be very well defined due to the thickness (200 – 300 Å) of the layer in which the projectiles have come to rest.

Even though the depth at which radiation damage occurs in the single crystals investigated significantly exceeds the range of Ar^+ ions predicted by LSS calculations (except in the case of iron) the radiation damage may still be spread over a certain thickness of the target at the deep damage depths due to Ar^+ energy straggling. Within the compressive stress defect propagation model a spread in Ar^+ ion energy (due to straggling) could cause a spread in the energy and positions associated with the thermal spikes and therefore also a spread in the depth at which interstitial—type damage might come to rest within the material after being subjected to the "shock—wave". Due to energy straggling a certain amount of spread in damage range would therefore still occur even if preferential <hkl> propagation did not take place.

(iii) Energy straggling of channeled analyzing He ions and limits of the system resolution

A contributing factor to the large standard deviations in relative damage range is the limitation of the system energy resolution (especially the contributions to $\underset{\sim}{\Omega}_r$ of detector and electronic standard deviations – see Chapter 1 section 5). Uncertainty in the knee position can also be caused by energy straggling of analyzing alpha particles. As discussed in Chapter 1 the standard deviations associated with energy straggling $(\underset{\sim}{\Omega}_s)$ and system resolution $(\underset{\sim}{\Omega}_r)$ add up quadratically (equation 1.25a). The total energy spread $(\underset{\sim}{\Omega}_{Tot})$ is dominated by $\underset{\sim}{\Omega}_r$ in the high energy region of the spectrum and the contribution of $\underset{\sim}{\Omega}_s$ increases with deeper target penetration. In the case of Pt, where the damage profiles lie relatively far below the target surface, the contribution of energy straggling $(\underset{\sim}{\Omega}_s)$ is therefore expected to be larger than in the case of Fe (where the damage is found to occur closer to the surface). Furthermore, in the case of very deep damage as was found in Pt, the sharp rise in RBS yield at low energy channels due to a general increase in multiple scattering processes deep within the crystal, sometimes makes it virtually impossible to discern a damage "kink" at all (therefore the absence of some R_d data in Table 8.4d).

Bohr energy straggling values $(\underset{\sim}{\Omega}_B^2)$ were calculated for each <hkl> direction investigated at each implantation temperature using the following values of $\dfrac{\Delta_B^2}{N\Delta x}$: Fe: 27,05; Ni: 29,13; Cu: 30,17; Pt: 81,16 $\left(\text{in units of } 10^{-12}(\text{eV cm})^2\right)$. R_d was substituted for Δx in each instance. The standard deviation in energy resolution due to

system limitations $(\underset{\sim}{\Omega}_r)$ could be determined by counting the number of channels over which the RBS yield at the random edge rises from a minimum to half its maximum value, and multiplying this number with δE. $\underset{\sim}{\Omega}_{Tot}$ could then be calculated from equation 1.25a after which δx, the total standard deviation in depth units due to both He straggling and system resolution was obtained from equation 1.26 (previously determined [S] values were used). All values of $\underset{\sim}{\Omega}_s$, $\underset{\sim}{\Omega}_r$, $\underset{\sim}{\Omega}_{Tot}$ and δx are listed in Tables 8.4a,b,c and d. The average $\underset{\sim}{\Omega}_r$, $\underset{\sim}{\Omega}_s$, $\underset{\sim}{\Omega}_{Tot}$ and δx values are listed in Table 8.8. In each instance $<\delta x>$ is compared with $\bar{s}_{exp}$, the total experimental standard deviation in R_d. It may be concluded from Table 8.8 that $\underset{\sim}{\Omega}_r$ plays a large role in the formation of the large standard deviations in average damage ranges. The differences in δx and $\bar{s}_{exp}$ can be due to the difficulty in determining $\underset{\sim}{\Omega}_r$ accurately (the method of $\underset{\sim}{\Omega}_r$ determination only provides an estimate), as well as possible contributions to $\bar{s}_{exp}$ of the various factors discussed in (i) and (ii).

It may also be noted that the calculated He straggling values $(\underset{\sim}{\Omega}_s)$ do not take into account the fact that the He ions are being channeled along the incident direction. Due to the sensitivity of the He stopping powers to the channeling angle, the value of $\underset{\sim}{\Omega}_s$ may be higher. A slightly higher $\underset{\sim}{\Omega}_s$ taking channeling into account would however not significantly influence the final value of δx because in all cases $\underset{\sim}{\Omega}_s$ was found not to contribute very greatly to the value of $\underset{\sim}{\Omega}_{Tot}$ (even in the case of platinum.) Therefore, also, the error introduced by substitution of R_d as Δx in the calculation of $\underset{\sim}{\Omega}_s$ is assumed to be small.

TABLE 8.8

Average standard deviation in energy ($\langle \Omega_{Tot} \rangle$) and depth ($\langle \delta x \rangle$) due to energy straggling and limited system resolution: Comparison with standard deviation in experimental R_d values ($\bar{s}_{exp}$).

77 K					300 K					423 K					523 K					573 K				
$\langle \Omega_r \rangle$ keV	$\langle \Omega_s \rangle$ keV	$\langle \Omega_{Tot} \rangle$ keV	$\langle \delta x \rangle$ Å	$\bar{s}_{exp}$ Å	$\langle \Omega_r \rangle$ keV	$\langle \Omega_s \rangle$ keV	$\langle \Omega_{Tot} \rangle$ keV	$\langle \delta x \rangle$ Å	$\bar{s}_{exp}$ Å	$\langle \Omega_r \rangle$ keV	$\langle \Omega_s \rangle$ keV	$\langle \Omega_{Tot} \rangle$ keV	$\langle \delta x \rangle$ Å	$\bar{s}_{exp}$ Å	$\langle \Omega_r \rangle$ keV	$\langle \Omega_s \rangle$ keV	$\langle \Omega_{Tot} \rangle$ keV	$\langle \delta x \rangle$ Å	$\bar{s}_{exp}$ Å	$\langle \Omega_r \rangle$ keV	$\langle \Omega_s \rangle$ keV	$\langle \Omega_{Tot} \rangle$ keV	$\langle \delta x \rangle$ Å	$\bar{s}_{exp}$ Å
13	5,19	14,0	103	80	13	5,97	14,3	105	49															
14	6,89	15,6	120	86	16	7,37	17,6	138	119						15	7,61	16,8	124	340					
15	8,7	17,4	149	280						15	9,35	17,7	154	239	15	9,41	17,7	155	327					
26	18,5	31,9	214	306						26	16,6	30,8	205	149						26	15,1	30,1	204	28

After annealing at 600 K (423 K): 26, 17,1, 31,1, 212, 250

5. INVESTIGATION OF THE VARIOUS POSSIBLE CAUSES OF DEEP RADIATION DAMAGE AND THE TEMPERATURE DEPENDENCE THEREOF

(i)   Due to the fact that deep radiation damage has been observed by various authors after heavy ion implantation well off any main crystal axes, **channeling** is not expected to be the main cause of deep radiation damage because too few channeled ions are generally expected to penetrate to these depths to cause sufficient damage. From evidence obtained in this study, however, the very large relative damage ranges observed for platinum (especially at low implantation temperatures) might well be attributed to the channeling phenomenon.   Before this evidence is discussed in more detail, a short explanation of the expected differences in damage ranges for implantation exactly *along* a main crystal axis as opposed to *off–axial* implantation is needed:

For implantation along a main crystal direction one would expect a significantly larger number of ions to become channeled than for implantation well off the crystal axis.   Referring to the specific example illustrated in figure 3.9, implantation along the <100> or <111> directions of tungsten might cause about 40% to 50% of the incident beam to channel up to depths significantly exceeding the LSS ion range.   If this relatively large fraction of channeled particles (large enough to cause discernible damage) finally comes to rest at a depth B_1 (refer to figure 8.7), a stress field propagation of defects formed at this depth would cause damage to propagate to the depth B_2.   The non–channeled fraction (in this case about 50% to 60%) of the incident beam would meanwhile have

come to rest within the (shallow damage) LSS stopping region, indicated as depth A_1 in figure 8.7. A stress field propagation of defects formed at A_1 might cause propagation of damage up to depth A_2. Subsequent helium dechanneling analysis of such a directionally implanted sample would yield a spectrum indicating damage right up to B_2.
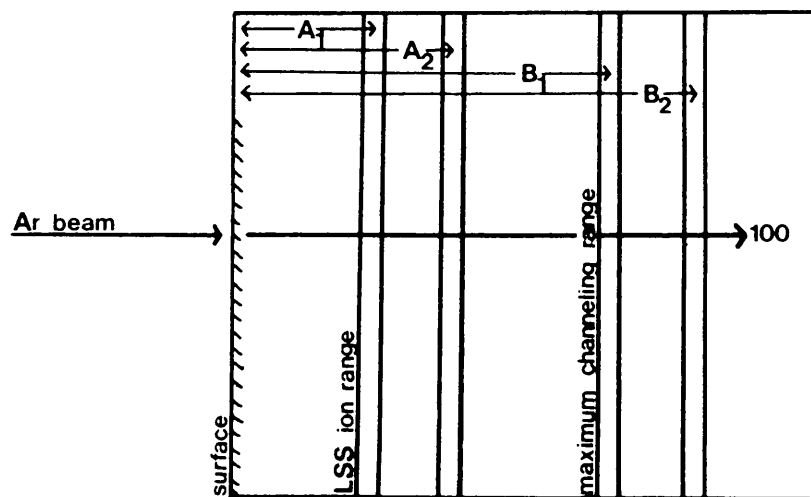
Figure 8.7 Discernible damage might extend up to B_1 and B_2 due to channeling.

However, for ions implanted in such a direction so that channeling along a main crystal axis is largely avoided (as was attempted in this study) the channeled fraction of the incident beam (a certain amount of channeling cannot be altogether avoided no matter what the incident beam angle[40]) reaching the depth B_1 would be too small to cause any discernible (cascade) damage at B_1 *or* subsequent "propagated damage" at B_2. Due to nearly all the incident ions causing cascade damage at A_1, subsequent He dechanneling analysis would only indicate (propagated) damage up to A_2.

The possible role of channeling in the very large relative damage ranges obtained for platinum will now be discussed: The approximate angles which various <hkl> directions make with the implantation direction can be determined by way of a simple dot product calculation or by referring to the stereographic projections illustrated in figures 7.6a, b and c. The results of such calculations are listed in tables 8.9a, b, c and d for the various metals investigated in this study. Also listed in these tables are the theoretical channeling half angles for Ar ions in the various <hkl> directions for the various implantation temperatures. (These half angles were determined in the same manner as the He half angles discussed in the previous section.) The expected decrease in half angle with increase in implantation temperature (due to defocussing processes) may clearly be discerned from tables 8.9a, b, c and d. Also discernible from these tables is the fact that quite a few relatively low index <hkl> directions possess half angles wide enough to allow channeling of Ar^+ ions for beam incidence 10° off the surface normal. In the case of platinum the half angles are significantly larger than for any of the other metals investigated. This allows possible channeling to occur along both the low index <111> and <211> directions of the 77 kelvin platinum implantation. For the specific beam direction employed none of the other metals exhibit as many very low index axes in a configuration favourable for channeling. Referring once again to figure 8.7 it therefore seems possible that in the case of platinum implanted at 77 K, a large enough fraction of the total ion beam is able to penetrate to the depth B_1 to cause detectable (propagated) damage at B_2, therefore the very large $<R_d/R_p>$ value. As the implantation temperature increases, the channeling half angle decreases and causes the ion fraction reaching

TABLE 8.9

Half angles for Ar⁺ channeling in various <hkl> directions and approximate minimum angle between each <hkl> direction and the implantation direction.

(a) Iron: $\theta(^\circ K) = 420;$ a = 2,867 Å

	77 K Implantation 10° off the <111> axis			300 K Implantation 10° off the <111> axis	
<hkl>	Minimum angle (degrees)	Half angle (degrees)	<hkl>	Minimum angle (degrees)	Half angle (degrees)
<332>	0	4,30	<332>	0	3,06
<322>	1	4,59	<322>	1	3,26
<221>	6	5,38	<221>	6	3,82
<211>	9	5,95	<211>	9	4,23
<111>	10	10,00	<111>	10	7,11
<321>	12	4,81	<321>	12	3,42
<331>	12	6,31	<331>	12	4,48
<311>	19	7,23	<311>	19	5,14
<110>	25	7,83	<110>	25	5,57
<210>	29	6,23	<210>	29	4,43
<310>	33	4,24	<310>	33	3,72
<100>	45	9,31	<100>	45	6,62

(b) Platinum: $\theta(^\circ K) = 225;$ a = 3,923 Å

<hkl>	Minimum angle (degrees) All implantations done 10° off the <111> direction	Half angles (degrees)			
		77 K	300 K	423 K	573 K
<332>	0	8,58	5,35	4,57	3,93
<322>	1	6,47	4,04	3,45	2,96
<221>	6	7,59	4,74	4,04	3,47
<211>	9	11,88	7,41	6,33	5,44
<111>	10	9,99	6,23	5,32	4,57
<321>	12	9,61	6,00	5,12	4,40
<331>	12	6,30	3,93	3,35	
<311>	19	7,22	4,50	3,84	
<110>	25	15,63	9,76	3,32	7,15
<210>	29	8,79	5,49	4,68	4,02
<310>	33	10,46	6,52	5,57	4,78
<100>	45	13,15	8,20	7,00	6,02

TABLE 8.9

(c) Copper: $\theta(^{o}K)$ = 315;   a = 3,615Å

	77 K Implantation 10° off the <100> axis			423 K Implantation 10° off the <111> axis			523 K Implantation 10° off the <111> axis	
<hkl>	Minimum angle (degrees)	Half angle (degrees)	<hkl>	Minimum angle (degrees)	Half angle (degrees)	<hkl>	(degrees)	(degrees)
<410>	4	3,85	<332>	0	2,84	<332>	0	2,55
<310>	8	6,22	<322>	1	2,14	<322>	1	1,93
<411>	9	5,37	<221>	6	2,51	<221>	6	2,26
<100>	10	7,82	<211>	9	3,92	<211>	9	3,53
<311>	15	4,30	<111>	10	3,30	<111>	10	2,97
<210>	16	5,23	<321>	12	3,18	<321>	12	2,86
<320>	24	4,12	<331>	12	2.08	<331>	12	1,87
<211>	25	7,07	<311>	19	2,38	<311>	19	2,15
<321>	27	5,72	<110>	25	5,16	<110>	25	4,65
<322>	33	3,85	<210>	29	2,90	<210>	29	2,62
<110>	35	9,31	<310>	33	3,45	<310>	33	3,11
<111>	45	7,82.	<100>	45	4,34	<100>	45	3,91

TABLE 8.9

(d) Nickel: $\theta(^{\circ}K) = 425$; $a = 3,524\text{Å}$

77 K Implantation 10° off the <100> axis			300 K Implantation 10° off the <100> axis			523 K Implantation 10 the <110> axis		
<hkl>	Minimum angle (degrees)	Half angle (degrees)	<hkl>	Minimum angle (degrees)	Half angle (degrees)	<hkl>	(degrees)	(degrees)
<410>	4	4,35	<410>	4	3,11	<320>	1	2,65
<310>	8	7,02	<310>	8	5,02	<331>	3	2,41
<411>	9	6,06	<411>	9	4,33	<210>	8	3,36
<100>	10	8,83	<100>	10	6,31	<321>	9	3,68
<311>	15	4,85	<311>	15	3,47	<221>	9	2,90
<210>	16	5,91	<210>	16	4,22	<110>	10	5,98
<320>	24	4,65	<320>	24	3,32	<332>	15	3,28
<211>	25	7,98	<211>	25	5,70	<310>	17	4,00
<321>	27	6,46	<321>	27	4,62	<211>	20	4,55
<322>	33	4,35	<322>	33	3,11	<111>	25	3,82
<110>	35	10,50	<110>	35	7,51	<100>	35	5,03
<111>	45	6,71	<111>	45	4,80			

B_1 to decrease correspondingly. The depth to which sufficient numbers of ions may penetrate via channeling to still cause detectable levels of damage, therefore decreases with temperature. Regions B_1 and B_2 in figure 8.7 move closer to the surface until they coincide with A_1 and A_2. This could possibly cause the gradual decrease in relative damage range with temperature which was observed in platinum but not in the other metals.

Further evidence that channeling plays a significant role in the large damage range obtained for the 77 K platinum implantation might be contained within figure 8.5. Whereas the damage ranges in all the other metals implanted at various temperatures do not exhibit a clear directional dependence, for some or other reason the damage ranges of the platinum samples implanted at 77 K decrease quite clearly (small error bars) in the following <hkl> ordering: <110>, <211> and <111>. This ordering corresponds exactly to the decrease in "channeling transparency" (i.e. how easily a certain crystal axis is able to channel a particle) discussed in Chapter 4. However, why such a trend is discernible is difficult to understand due to the inability of the alpha particle dechanneling analysis method to discern along which crystal direction initial defect (or Ar ion) propagation took place (as discussed in section 4 of this chapter). This seemingly directional dependence of the damage range for the 77 K implanted platinum sample might therefore be purely coincidental. (It cannot be attributed to large variations in He stopping powers because, if such variations existed, the exact opposite ordering would be expected.) More statistical data would have to be obtained to verify this trend. The very fact that the damage in this

instance lay very deep (which made it very difficult to discern the correct position of the damage "knee") forces one to be very cautious in the interpretation of a seemingly directional trend in the observed damage ranges.

A comparison of the axes available for channeling at 77 K in the iron sample (332, 322, 221 and 111) as opposed to those available in the copper (410 and 310) and the nickel (410, 310 and possibly 100) samples show that channeling cannot be the main cause of deep radiation damage in these metals because iron (for which $R_d/R_p \sim 1$) has about as many axes available for channeling as are available for nickel and copper, both of which have significantly larger relative damage ranges.

Evidence against the suggested role which channeling plays in the decrease in damage range with increase in temperature observed in platinum is supplied by Davies et al.[42] who proved (within a 3% experimental error) that the maximum channeling range in tungsten is completely independent of temperature. (However, the *number* of particles reaching the maximum range may still be temperature dependent.) The orientation dependence of the damage range (in copper) observed by Vos and Boerma[49] at temperatures below 300 K further substantiate a possible channeling mechanism in the production of deep radiation damage at low implantation temperatures.

(b) The applicability of the **thermal interstitial migration** model as an explanation of deep radiation damage can be investigated by studying the differences in the average damage ranges obtained in the various

metals. From Table 8.5 it can be seen that the $<R_d/R_p>$ values are approximately 1 for iron, 2 for nickel, 3 for copper and 7 for platinum. The extent to which radiation damage is deeper than the LSS predicted ion range therefore differs greatly from material to material and this agrees with the findings of Friedland et al.[65,67,89] If thermal migration of interstitials were responsible for this deep damage, one would not expect such a large variation because the migration energies for interstitials are quite similar in these solids.[67] Furthermore, if interstitial migration took place by way of replacement collision sequences, one would expect a decrease in damage range with temperature (due to defocussing as discussed in Chapter 6 section 7(i)) a trend which (except for platinum which might be explained by channeling) has not been observed in this study.

(c) A number of trends obtained from the data of this study seem to point to the existence of a **compressive stress field** (set up due to thermal expansion associated with the thermal spike) propagating defects deep into the crystal:

(i) The gradual increase in damage range with implantation temperature in iron (and possibly also in copper and nickel when only taking into account the mean $<R_d/R_p>$ values and ignoring the large error bars in figure 8.3) would be consistent with a compressive stress field propagation of defects: A reduction in crowdion trajectories with increase in irradiation temperature (as discussed in Chapter 6) would cause an increase in agitation within the cascade region resulting in a more intense thermal spike and therefore also a larger compressive

stress. Defects would then be propagated deeper with increase in implantation temperature. A slowly increasing damage depth with increase in temperature also seems reasonable if one considers that the Peierls force, which governs dislocation dynamics, decreases with increasing temperature.

(ii) The rather "spread out" damage knees might be an indication of defects being propagated further along preferred <hkl> directions, as discussed in section 4 of this chapter.

(iii) The distinct differences observed in the relative damage ranges of the various metals (1 for Fe, 2 for Ni, 3 for Cu and 7 for Pt) are consistent with the compressive stress field theory. The ordering of the relative range values for the various metals, namely $<R_d/R_p>_{Pt} > <R_d/R_p>_{Cu} > <R_d/R_p>_{Ni}$ are in agreement with the explanation given in section 7(ii) of Chapter 6 in which ion–beam mixing values, cohesive energies, energy densities and the thermal spike theory is taken into account. The fact that the experimental relative damage range in platinum is considerably higher than that in copper (which is not predicted in the discussion in Chapter 6) could in part be due to a domination of the energy density component of Pt which is too high to counterbalance the opposing effect of its higher cohesive energy. The role which channeling might play in the high $<R_d/R_p>$ value for Pt (especially at 77 K) should however also be kept in mind. The fact that the difference in experimental damage range and projected range is much smaller for bcc iron than for the three fcc metals investigated, is in

accordance with the higher Peierls force opposing dislocation motion in bcc metals. (The atomic packing is less dense.)

(iv) The change in the amount or level of deep radiation damage with increase in implantation temperature was also investigated. An indication of the level of deep radiation damage was obtained by determining the normalized minimum yields in both the damaged and undamaged spectra (respectively χ_d and χ_v) at the channel number corresponding to the damage "knee" for each metal/temperature combination investigated (only the 1,5 MeV α–particle spectra were used). These values were incorporated into equation 5.6, thereby obtaining the integrated dechanneling probability due to defects (represented by the symbol I). The results of these calculations are listed in Table 8.10 and are also represented graphically in figure 8.8. (Least square linear fits were once again employed to connect data points.) For all the metal samples investigated, I decreases slightly with increase in implantation temperature, though such a trend must once again be viewed with caution due to the relatively large statistical deviations in the data used to obtain the lines in figure 8.8. (Error bars are not indicated in this figure but they would overlap.) A decrease in the level of deep radiation damage with increase in irradiation temperature would agree with the results obtained by the authors discussed in Chapter 6[49,50,63]. Within the stress field propagation model a reduction in crowdion trajectories with increase in irradiation temperature, resulting in less interstitials being able to escape the cascade region before the onset of the thermal spike, could explain the decrease in the overall level of radiation damage with

164

TABLE 8.10

Investigation of the amount of deep radiation damage as a function of increase in implantation temperature

Metal	$I = -\ln \dfrac{(1 - \chi_d)}{(1 + \chi_d)} \times 10$ at various temperatures χ_d = normalized yield at damage knee χ_v = normalized yield at the corresponding channel in the undamaged spectrum				
	77 K	300 K	423 K	523 K	573 K
a–Fe	$5,9 \pm 0,2$	$5,4 \pm 0,5$			
Ni	$5,9 \pm 0,8$	$5,4 \pm 0,7$		$5,4 \pm 0,7$	
Cu	$5,5 \pm 0,3$		$5,5 \pm 0,6$		
Pt	$5,5 \pm 1,6$		$4,9 \pm 1,0$ Anneal 600 K = $3,6 \pm 1,0$		$2,5 \pm 0,9$

increase in implantation temperature. Thermal vacancy emission as well as annealing are two other factors which could contribute to decreased damage levels.

The platinum samples implanted at 423 K and 573 K show a considerably smaller value of I than is exhibited by the other metals implanted at similar temperatures, while the 77 K platinum sample possesses an I value comparable to those of Fe, Ni and Cu. The sharper drop in Pt damage level with temperature from 77 K to 423 K (as opposed to that of the other metals) might be related to the relatively sharp decrease in the number of low index axes along which damage–inducing Ar ions

Figure 8.8   Temperature dependence of damage levels
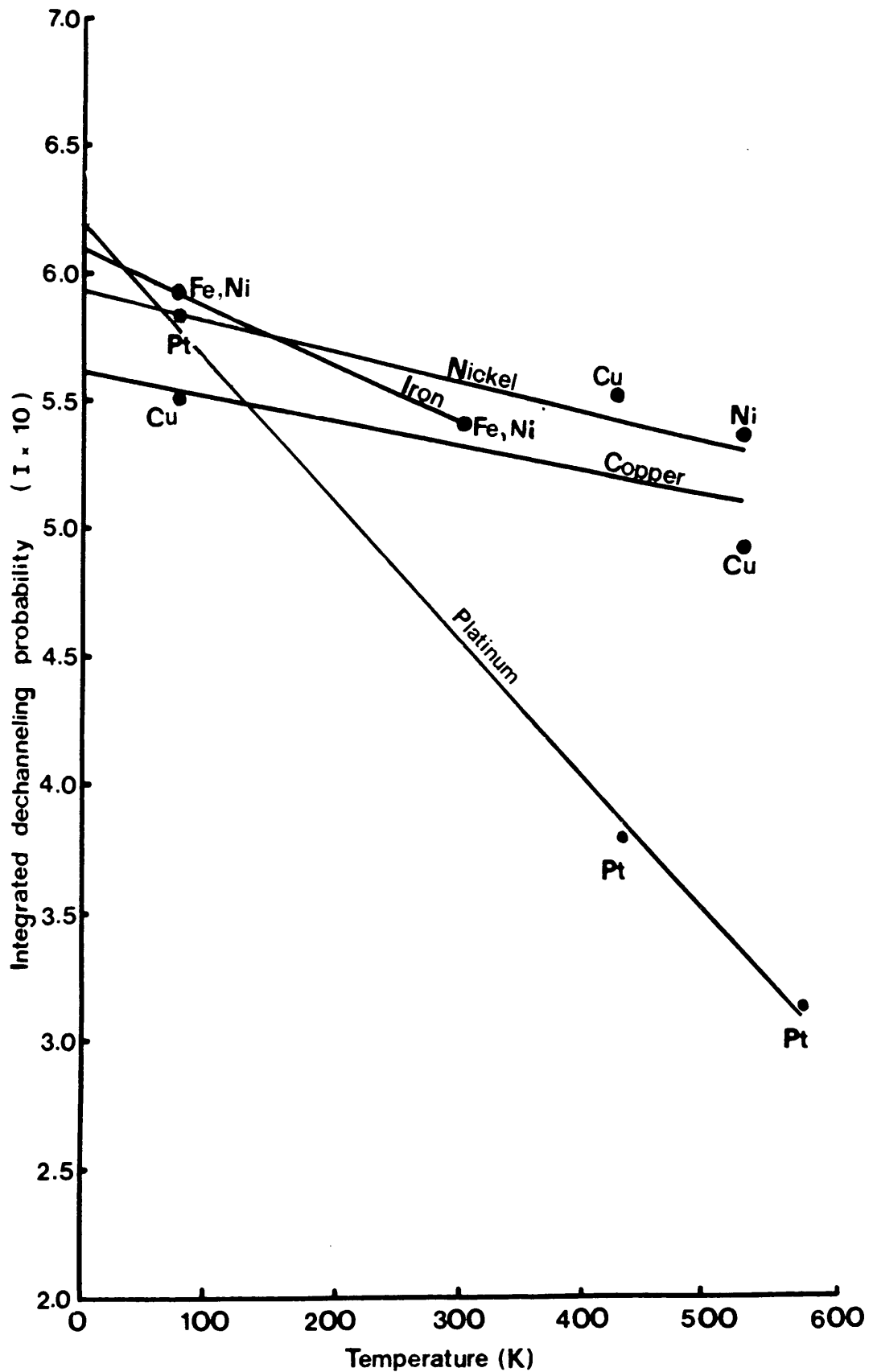
are channeled as the channeling half angles decrease with increasing implantation temperature.

The Pt sample initially implanted at 423 K was annealed at 600 K (under vacuum) and once again investigated: no apparent change in damage level (*or* range) could be discerned (Refer to tables 8.10 and 8.4d.) Annealing, therefore, does not seem to play a role in the difference in damage level between the 423 K and 573 K Pt implantations. This difference may well be attributed either to channeling or to the increase in stress field intensity with increase in implantation temperature.

(**Note**: The damage levels of all the metals were also compared along the various <hkl> directions but no definite trend could be discerned.)

6. THE ALPHA PARTICLE ENERGY DEPENDENCE OF THE DAMAGE LEVELS IN THE PLATINUM SAMPLES

Unluckily, damage level data for nickel, copper and iron could only be obtained from 1,5 MeV alpha particle dechanneling spectra. (Undamaged 1,8 or 1,7 MeV alpha particle dechanneling spectra had generally not been collected and therefore the value of χ_v in equation 5.6 was not available.) For platinum, however, spectra of both energies were available from which a possible energy dependence of the damage level, as listed in Table 8.11, might be discerned:

TABLE 8.11

Implantation Tempe−rature (K)	Integrated dechanneling probability, I (× 10), at various a−particle energies (for platinum)		$\dfrac{I_{1,5}}{I_{1,8}}$
	1,5 MeV	1,8 MeV	
77	5,8 ± 1,9	5,3 ± 1,7	1,1
423	3,8 ± 1,3	3,5 ± 1,6	1,1
573	3,1 ± 0,2	2,6 ± 0,4	1,2

Although the large experimental deviations make accurate interpretation of these results difficult, the I values for all the implantation temperatures listed in this table seem to be slightly lower for damage analysis with the higher energy analyzing beam. For an $E^{-\frac{1}{2}}$ dependence of the dechanneling cross section, one would expect $\dfrac{\sigma(E_{1,5})}{\sigma(E_{1,8})} = \sqrt{\dfrac{1,8}{1,5}} \sim 1,1$. This ratio corresponds quite well to the values of $\dfrac{I_{1,5}}{I_{1,8}}$ listed in Table 8.11. As discussed in Chapter 5, an inverse proportionality of the dechanneling cross section to the square of the alpha particle energy indicates the presence of point defects being the main cause of dechanneling (as opposed to dislocations or stacking faults). This observation must however be viewed with caution due to the small amount of data available and the large fluctuations occuring around the mean I−values.

7. RESULTS OF TRIM CALCULATIONS

The TRIM86 computer programme was used to calculate projected damage ranges in all four metals investigated. In the calculation a fictitious

distribution of collision parameters and pathlengths in an amorphous solid is assumed. For all four metals the following inputs applied:

Ion = Ar

Ion Energy = 150 keV

Displacement Energy = 25 eV

Binding Energy = 2 eV

Surface Energy = 1 eV

All cascades were followed and the calculation was terminated when about 1000 ions had been incorporated.
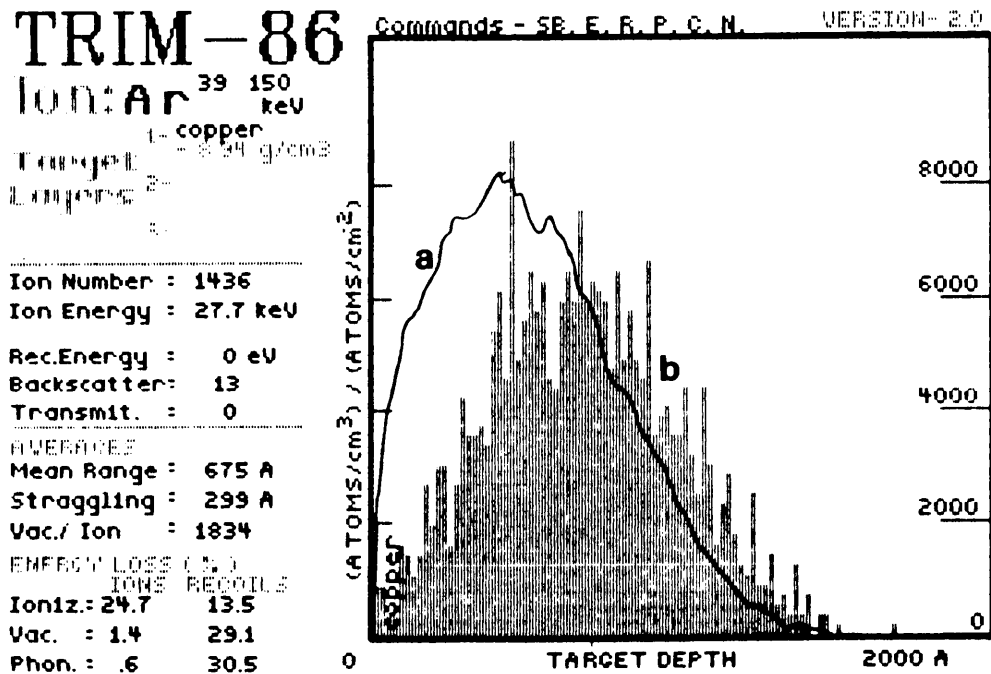
Figure 8.9   TRIM (a) damage range and (b) ion range profiles for 150 keV Ar ions incident on a Cu target.

As illustrated in figure 8.9 for the copper calculation, the mean value of the damage distribution in the *amorphous* material calculated by TRIM, actually lies closer to the surface than that of the ion range profile. This

was found to be the case for all the metals investigated (see Table 8.12) and is a finding in direct contrast with the experimental results obtained in this study of the *crystalline* metals (where damage ranges significantly exceed projected ion ranges, especially in the case of the fcc metals).

The distribution of the incident Ar^+ ion energy into its various energy loss components was also calculated by TRIM for each metal, and is listed in Table 8.13. The percentage of the incident ion energy used in the creation of dislocation–type damage is only that component needed for the production of vacancies and recoils. (Ionization energies are quickly dissipated as heat

TABLE 8.12

Metal	Mean ion range (Å)	Mean damage range (Å)	Straggling (halfwidth) of ion profile (Å)
Fe	673	~ 460	284
Ni	610	~ 400	272
Cu	675	~ 420	299
Pt	487	~ 250	262

and therefore do not play a role in the creation of damage.) The energy involved in damage creation is, for Fe: $\frac{1,4 + 24,8}{100} \cdot 150 \simeq 39$ keV, for Ni: $\frac{1,4 + 21,9}{100} \cdot 150 \simeq 35$ keV, for Cu: $\frac{1,4 + 29,1}{100} \cdot 150 \simeq 46$ keV and for Pt: $\frac{1,5 + 27,2}{100} \cdot 150 \simeq 43$ keV. The phonon energies (due to subthreshold collisions) vary between 21% and 32% of the incident ion energy. In actual crystalline structures the release of this relatively large amount of energy in a very short period of time might be largely responsible for the very high

TABLE   8.13

Metal	Percentage energy loss due to					
	ioniza-tion of inci-dentions	ioniza-tion of recoils	vacancy produc-tion	recoil produc-tion	phonon excita-tion by ions	phonon excita-tion by recoils
Fe	30,3	16,0	1,4	24,8	0,5	26,9
Ni	25,6	18,3	1,4	21,9	0,6	32,0
Cu	24,7	13,5	1,4	29,1	0,6	30,5
Pt	27,9	21,5	1,5	27,2	0,6	21,2

energy densities along the ion track (resulting in the shock–wave which propagates defects deep into the bulk of the crystal, thereby causing deep damage).

TRIM also computes the average number of vacancies formed per incident ion.   As mentioned in Chapter 6, this computation is done by carrying out the modified Kinchin–Pease calculation for each PKA formed. As may be seen from studying Table 8.14, this method of determining the number of Frenkel pairs leads to an answer considerably ($\sim$ 3 times) smaller than the result obtained by a single substitution of the full ion energy into the modified Kinchin–Pease expression.   A smaller number of stable Frenkel pairs is in agreement with both experimental and molecular dynamic simulation results obtained by the various authors[63,65,73,78] mentioned in Chapter 6.

TABLE 8.14

Metal	Number of vacancies per ion predicted by TRIM	Number of stable Frenkel pairs as calculated from the modified Kinchin–Pease equation: $N(E) = 0,8 \dfrac{E}{2E_d}$, $E = 150$ keV $E_d = 25 \times 10^{-3}$ keV
Fe	1584	
Ni	1883	4800
Cu	1834	
Pt	1627	

The method of carrying out the modified Kinchin–Pease calculation for *each* PKA formed, might also explain why the TRIM damage range lies somewhat closer to the surface than the ion range profile: The closer to the surface PKA formation takes place, the higher the average energy E of the PKA and the greater the average number of Frenkel pairs N(E) created by the PKA (refer to equation 6.3).

END

REFERENCES

1. Ashworth V., Grant W.A., Procter R.P.M., Wellington T.C., Corr. Sci., **16** (1976) 393

2. Hermann H., Nucl. Instr. Meth., **182/183** (1981) 887

3. Li H.T., Liu P.S., Chang S.C., Lü H.C., Wang H.H., Tao K., Nucl. Instr. Meth., **182/183** (1981) 915

4. Singer I.C., Carosella C.A., Reed J.R., Nucl. Instr. Meth., **182/183** (1981) 923

5. Dearnaley G., Nucl. Instr. Meth., **182/183** (1981) 899

6. Clayton C.R., Nucl. Instr. Meth., **182/183** (1981) 865

7. Chu W.K., "Backscattering Spectrometry", Academic Press (1978)
    (a) p.350   (b) p.29   (c) p.30   (d) p.50   (e) p.39   (f) p.22
    (g) p. 26   (h) p.60   (i) p.59   (j) p.45   (k) p.59   (l) p.224

8. Bohr N., Phil. Mag. **30** (1915) 581

9. Chu W.K., from "Ion Beam Handbook for Material Analysis", ed. Mayer J.W., Rimini E., Academic Press (1977) 6

10. Chu W.K., Phys. Rev., **A13** (1976) 2057

11. Lindhard J., Scharff M., Mat. Fys. Medd. Dan. Vid. Selsk., **27** no.15 (1953)

12. Friedland E., Lombard J.M., Nucl. Instr. Meth. **168** (1980) 25

13. Bohr A., Kgl. Dan. Vid. Selsk. Mat. Fys. Medd., **24** no.19 (1948)

14. Lindhard J., Scharff M., Schiott H.E., Mat. Fys. Medd. Dan. Vid. Selsk., **33** no.14 (1963)

15. Bethe H.A., Ann. Phys., **5** (1930) 325

16. Bloch F., Ann. Phys., **16** (1933) 285

17. Ziegler J.F., "The Stopping and Ranges of Ions in Matter" Vol.4, (1977), Pergamon Press Inc.

18. Ziegler J.F., "Ion Implantation Science and Technology" (1984), Academic Press Inc., publ. Harcourt, Brace, Jovanovich

     (a) p.75   (b) p.87   (c) p.60

19. Firsov O.B., Zh. Eksp. Teor. Fiz., **32** (1957) 1464

20. Lindhard J., Mat. Fys. Medd. Dan. Vid. Selsk., **28** no.8 (1954)

21. Northcliffe L.C., Phys. Rev., **120** (1960) 1744

22. Robinson M.T., Oen O.S., Phys. Rev., **152** (1963) 2385

23. Barrett J.H., Phys. Rev., **3**, no.5 (1971) 1527

24. Robinson M.T., Torrens I.M., Phys. Rev. B, **9** no.12 (1974)

25. Appleton B.R., Foti G., "Ion Beam Handbook for Material Analysis", ed. Mayer J.W., Rimini E., Academic Press (1977)

26. Schiott H.E., Can J. Phys. **46** (1968) 449

27. Ziegler J.F., "The Stopping and Ranges of Ions in Matter" Vol.1, (1985), Pergamon Press Inc.

28. Whitton J.L., from "Channeling Theory, Observation and Applications", ed. Morgan D.V., publ. John Wiley and Sons, (1973), p.225

29. Bergstrom I., Domeij B., Nucl. Instr. Meth., **43** (1966) 146

30. Lehmann Chr. "Interaction of Radiation with Solids and Elementary Defect Production" (1977) North Holland Publishing Co.

     (a) p.107   (b) p.109 (c) p.157 (d) p.183 (e) p.108 (f) p.171
     (g) p.200

31. Lindhard J., Dan. Vid. Selsk. Mat. Fys. Medd., **34** no.14 (1965)

32. Lehmann C., Leibfried G., J. Appl. Phys., **34** (1963) 2821

33. Morgan D.V., from "Channeling Theory, Observation and Applications", ed. Morgan D.V., publ. John Wiley and Sons, (1973), p.79

34. Bohr N., K. Dan. Vid. Selsk. Mat. Fys. Medd., 18 no.8 (1948)

35.   Gemmell D.S., Rev. Mod. Phys., **46** no.1 (1974)

36.   Firsov O.B., (a) Zh. Eksp. Teor. Fiz. **34** (1958) 447;   (b) JETP., **7** (1958) 308

37.   Van Vliet D., Rad. Effects. **10** (1971) 137

38.   Eriksson L., Phys. Rev., **161** (1967) 235

39.   Davies J.A., Jespersgard P., Can. J. Phys. **44** (1966) 1631

40.   Ecker K.H., Macht M.P., Naundorf V., Nucl. Instr. Meth., **B15** (1986) 66

41.   Whitton J.L., Can. J. Phys., **46** (1968) 581

42.   Davies J.A., Eriksson L., Whitton J.L., Can. J. Phys. **46** (1968) 573

43.   Dearnaley G., "Channeling Theory, Observation and Applications", ed. Morgan D.V. publ. John Wiley and Sons, (1973) p.140

44.   Mory J., Quere Y., Rad. Eff., **13** (1972) 57

45.   English C.A., Eyre B.L., Phil. Mag. **34** no.4 (1976) 603

46.   Kirk M.A., Robertson I.M., Jenkins M.L., English C.A., Black T.J., Vetrano J.S., J. Nucl. Mat. **149** (1987) 21

47.   Jenkins M.L., English C.A., Eyre B.L., Phil. Mag. **A38** no.1 (1978) 97

48.   Haussermann Von F., Phil. Mag. **25** (1972) 537

49.   Vos M., Boerma D.O., Nucl. Instr. Meth. **B15** (1986) 337

50.   Lindgreen R.J. TH., Boerma D.O., de Hosson J. TH. M., Rad. Eff. **71** (1983) 289

51.   Peierls R.E., Proc. Phys. Soc. Lond. **52** (1940) 34

52.   Weertman J., Weertman J.R., "Elementary Dislocation Theory" (1964); publ. Macmillan Company New York, (a) p.149   (b) p.97 (c) p.57   (d) p.148   (e) p.72

53.   Eisen F.H., "Channeling Theory, Observations and Applications", ed. Morgan D.V., publ. John Wiley and Sons (1973), p.417

54. Quéré Y., Ann. Phys. **5** (1970) 105

55. Quéré Y., J. Nucl. Mat. **53** (1974) 262

56. Grobb J.J., Siffert P., Nucl. Instr. Meth., **209/210** (1983), 413

57. Jousset J.C., Mory J., Quillico J.J., J. Phys. Lett. **35** (1974) L229

58. Lindgreen R.J. TH., Dissertation

59. Morita K., Sizmann R., Rad. Eff. **24** (1975) 281

60. Mory J., Ligeon E., J. Mat. Sci. **17** (1982) 925

61. Quéré Y., Phys. Status Solidi **30** (1968) 713

62. Borders J.A., Poate J.M., Phys. Rev. **B13** (1976) 969

63. Sood D.K., Dearnaley G., J. Vac. Sci. Technol. 12 no.1 (1975)

64. Friedland E., Malherbe J.B., Alberts H.W., Vorster R.E., S. Afr. J. Phys. **9** no.4 (1986)

65. Friedland E., Alberts H.W., Nucl. Instr. Meth. **B33** (1988) 710

66. Matthews L.M., Ball C.A.B., J. Appl. Phys. **61** (6) (1987) 2166

67. Friedland E., Alberts H.W., Nucl. Instr. Meth. **B35** (1988) 244

68. Linker G., Gettings M., Meyer O., from "Ion Implantation in Semiconductors and other Metals", ed. Crowder B.L., publ. Plenum New York (1974) p.465

69. Diehl J., Diepers H., Hertel B., Can. J. Phys. **46** (1968) 647

70. Eyre B.L., J. Phys. F: Metal Phys. **3** (1973) 422

71. Gibson J.B., Goland A.N., Milgram M., Vineyard G.H., Phys. Rev. **120** no.4 (1960) 1229

72. Townsend P.D., Kelly J.C., Hartley N.E.W., "Ion Implantation, Sputtering and their Applications", publ. Academic Press (1976) p.69

73. Averback R.S., Benedek R., Merkle K.L., Phys. Rev. **B18** (1978) 4156.

74. Averback R.S., Seidman D.N., Materials Science Forum, Volumes 15–18 (1987) publ. Trans. Tech. Publications Ltd., Switzerland, (a) p.963 (b) p.967

75. Protasov V.I., Chudinov V.G., Rad. Eff. **66** (1982) 1

76. Seitz F., Koehler J.S., Solid State Physics **2** (1956) 351

77. Gratton L.M., Miotello A., Tosello C., Appl. Phys. **A36** (1985) 139

78. Averback R.S., Diaz de la Rubia T., Benedek R., Nucl. Instr. Meth. **B33** (1988) 693

79. Kapinos V.G., Platinov P.A., Rad. Eff. 103 (1987) 45

80. Sigmund P., Rad. Eff. **1** (1969) 15

81. Kinchin G.H., Pease R.S., Repts. Prog. Phys. **18** (1955) 1

82. Kim S.J., Nicolet M.A., Averback R.S., Peak D., Phys. Rev. **B37** (1988) 1

83. Silsbee R.H., J. Appl. Phys. **28** (1957) 1246

84. Kirk, M.A., Blewitt T.H., Metall. Trans. **9A** (1978) 1729

85. Quéré Y., Rad. Eff. 28 (1976) 253

86. Agranovich V.M., Kirsanov V.V., "Physics of Radiation Effects in Crystals", Vol.13 of "Modern Problems in Condensed Matter Sciences", general editors Agranovich V.M., Maradudin A.A., (a) p.119   (b) p.143   (c) p.142

87. Nelson R., Thompson M., Proc. Royal Soc. London, **A259** (1961) 458

88. Black T.J., Jenkins M.L., English C.A., Kirk M.A., Proc Royal Soc. London, **A409** (1987) 177

89. Friedland E., le Roux H., Malherbe J.B., Rad. Eff. Lett. **87** (1986) 281

90. Seitz F., Phys. Rev. **79** (1950) 723

91. Jones D.A., Mitchell J.W., Phil. Mag. **3** (1958) 1

92. Howe L.M., McGurn J.F., Gilbert R.W., Acta Metall. **14** (1966) 801

93. Oen O.S., Robinson M.T., Appl. Phys. Lett. **2**, no.4 (1963) 83

94. Van Tonder B.J.E., Dissertation

95. Van Vliet D., from "Channeling Theory, Observation and Applications", ed. Morgan D.V., publ. John Wiley and Sons, (1973) p.37.

96. Blakemore J.S., "Solid State Physics", publ. W.B. Saunders Company (1974), p.28.

97. Pathak A.P., Bull. Mater. Sci., **10** no. 1 & 2 (1988) 105